UNIVERSITÁ DELLA CALABRIA

DIPARTIMENTI DI CHIMICA E FISICA

B. Telesio-Scuola di Dottorato di Scienza e Tecnica

Dottorato di Ricerca in
"Scienze e Tecnologie delle Mesofasi e dei Materiali Molecolari"
(STM^3) – XXIV Ciclo

Ph. D. Thesis

"Organic semiconductors for molecular electronics: *Columnar mesophases & Organic Photovoltaics with Low Molecular Weight compounds*"

Supervisore

Prof. Attilio Golemme

Coordinatore

Prof. Carlo Versace

Candidato

Upendra Kumar Pandey

Anno accademico 2010-2011

UNIVERSITÁ DELLA CALABRIA

DIPARTIMENTI DI CHIMICA E FISICA

B. Telesio-Scuola di Dottorato di Scienza e Tecnica

Dottorato di Ricerca in
"Scienze e Tecnologie delle Mesofasi e dei Materiali Molecolari"
(STM^3) – XXIV Ciclo

Ph. D. Thesis

"Organic semiconductors for molecular electronics: *Columnar mesophases & Organic Photovoltaics with Low Molecular Weight compounds*"

Settore disciplinare: CHIM02

Supervisore

Prof. Attilio Golemme

Coordinatore

Prof. Carlo Versace

Candidato

Upendra Kumar Pandey

Anno accademico 2010-2011

To my parents

Acknowledgements

It gives me great pleasure to express my deep sense of gratitude to my research supervisor Prof. Attilio Golemme for his guidance, support, encouragement and scientific temperament which furthered my interest in "Molecular Electronics", perticlulary in the field of discotic liquid crystals and organic photovoltaics. I do sincerely acknowledge freedom rendered to me by him for independent thinking, planning and executing the research. He has taught me to be concise, systematic and correct in my approach from the formulation of ideas to the presentation of the results.

My sincere thanks goes to Prof. Roberto Bartilino, Director, B. Telesio School of science and technique of University of Calabria for giving me an opportunitity to pursue my Ph.D. I extend my thanks to Prof. Carlo Versace, co-ordinator of this Ph.D. course, who was always available towards all of us, Ph. D. students, whenever required. I extend my further gratitude to Prof. Mauro Ghedini, Department of chemistry for his support and encouragement during my Ph.D.

I would like to thank my colleagues and friend Dr. Roberto Termine and Dr. Nicolas Godbert from University of Calabria, who helped me many times in the resolution of technical problems and useful discussions.

I would also like to thank all my close friends of India, Italy and of other countries for their cheerful company during my Ph.D. life.

No thanks can be enough to acknowledge the endless encouragement, care and long-distance support, which I had from my parents Shri Ramesh Chand Pandey and Smt. Brijkumari Pandey, brothers Dr. Ravindra Pandey and Dr. Satyendra Pandey and sisters Smt. Kusum Dubey and Smt. Anita Mishra for their love and co-operation. Their constant encouragement helped me in pursuing the Ph. D. and made me achieve the goal.

Help from the physics department is gratefully acknowledged. I sincerely thank Dr. Alfredo Pane, Dr. Maria Penelope De Santo and Dr. Salvatore Abate for their kind co-operation and help during my Ph.D.

Upendra Kumar Pandey

PLEDGE AGAINST PLAGIARISM

I, **Upendra Kumar Pandey**, hereby confirm that the work submitted in this report is my own and that I have not violated the University of Calabria's policy on plagiarism.

Place: Rende, CS, Italy
Date: 30/11/2011

Signature_____

(UPENDRA KUMAR PANDEY)

INDEX OF CONTENTS

Chapter 3

Mobility of columnar mesophases

Section -2

Chapter 4

OPV: Introduction

Chapter 5

OPV: Materials and methods.

Chapter 6

OPV: Results and discussion

INTRODUCTION

"The electronics of the 20th century is based on semiconductor physics. The electronics of the 21st century will be based on molecular chemistry/physics"

--- ***F.L. Carter***

Molecules have not historically played a prominent role in electronic devices. Fifteen years ago, chemical applications were limited to the use of small molecules such as the components of etching processes, resist precursors, packaging materials etc. Engineered inorganic insulators, semiconductors, and metals were the heart of the industry, and the fundamental knowledge that gave birth to the integrated circuit was appropriately credited back to the fundamental solid-state physics that was largely developed in the mid-20th century.

Over the past two decades, the picture has changed. Conducting polymers have emerged as a real technology. In the next 10 – 15 years, molecules will be increasingly viewed not just as the starting points for bulk electronic materials, but as the active device components within electronic circuitry. Although this possibility is hardly a foregone conclusion, a number of fundamental issues favor the development of a true molecular-based electronics.

Although molecular electronics has been the subject of research for more than a decade, over the past few years a number of synthetic and quantum chemists, physicists, engineers, and other researchers have sharply increased the ranks of this field. Several new molecular-electronic systems, analytical tools, and device architectures have been introduced and explored. As a result, the basic science on which a molecular electronics technology would be built is now unfolding, and the science and applications that are emerging are tremendously exciting. But, here, one question comes in mind immediately: why do we need molecular electronics based on the organic semiconductors when we have a well-developed technology based on its inorganic counterpart ?

All electronic processes in nature, from photosynthesis to signal transduction, occur in molecular structures. For electronics applications, molecular structures have four major advantages:

1. **Size.** The size scale of molecules is between 1 and 100 nm, a scale that permits functional nanostructures with accompanying advantages in cost, efficiency, and power dissipation.
2. **Assembly and recognition**. One can exploit specific intermolecular interactions to form structures by nanoscale self-assembly. Molecular recognition can be used to modify electronic behavior, providing both switching and sensing capabilities on the single-molecule scale.
3. **Dynamical stereochemistry**. Many molecules have multiple, distinct, stable geometric structures or isomers. Such geometric isomers can have distinct optical and electronic properties and
4. **Synthetic tailorability.** By choice of composition and geometry, one can extensively vary a molecule's transport, binding, optical, and structural properties. The tools of molecular synthesis are highly developed.

However, molecules have disadvantages, too, such as instability at high temperatures. But overall, the advantages render molecules ideal for electronics applications, such as switches, nonlinear components, **rectifiers**, **transistors**, **photovoltaics**, and memories. In particular, a large amount of efforts is currently dedicated to the industrial commercialization of various rectifiers and transistors, such as OLEDs, OFETs and photovoltaics based on organic semiconducting (OS) materials.

Organic semiconductors are solution-processable and can be incorporated into a variety of electronic devices, unlike inorganic semiconductors, that require the use of expensive and time consuming vacuum processes. OS are then considered among the most useful candidates in the fabrication of electronic devices. However, the performances of devices based on organic conjugated materials still suffer from the very low charge carrier mobilities (typically $< 10^{-2}$ cm^2 V^{-1} s^{-1}) in devices fabricated by using spin coating and ink jet printing[1] that one would like to exploit on the industrial scale. This drawback is inherent to disorder (for example, structural defects or grain boundaries) present in non-crystalline oligomer or polymer materials. In this context, molecules that can form ***"columnar liquid crystalline"*** phases appear attractive as their high degree of ordering from self-assembly can lead to charge mobilities of the same order of magnitude as those in amorphous silicon[2-5]. In addition, these materials are characterized by ease of

processing, capacity of self-healing and possibility of alignment over long distances, making them a promising class of materials for molecular electronics.

In the first section of this dissertation, a new class of columnar liquid crystals formed by mesogens with a triindole core showing very high charge carrier mobility will be described. Also, the optoelectronic properties of a similar discotic liquid crystal formed by a totally different new linearly conjugated core will be discussed.

The second section of the dissertation will focus on the photovoltaics application of organic semiconductors. Nowadays, energy and environment have become two of the most critical subjects of wide concern and these two topics are also related to each other. An estimated more than 80 % of todays world energy supplies are from the burning of fossil fuels such as coal, gas or oil. However, carbon dioxide and toxic gasses released from fossil fuel burning contribute significantly to environmental degradation, such as global warming, acid rains, smog, etc. In addition, fossil fuels deposits on Earth are not unlimited.

Sunlight is instead an unlimited, clean, renewable and easily available source of energy, which can be exploited for our energy needs. Here comes the other important use of organic semiconductors in the field of molecular electronics. In the past decade organic semiconductors were broadly investigated for ***"photovoltaics"*** applications, which basically is the conversion of sun light into electricity.

Organic semiconductors can provide inexpensive sources of solar electricity via low-temperature fabrication on flexible substrates, impossible for inorganic semiconductors (such as silicon) based solar cells[6,7]. Until now, the development of organic solar cells has been essentially based on the use of soluble π-conjugated polymers [8-10] as donor materials. These conjugated polymers were mainly used in conjunction with PCBM acceptors. Efficiencies of more than 7 %[11] are reported in the literature for such devices. However, these conjugated polymers pose several problems related to the control of their structure, molecular weight polydispersity, and purification. In this context, recent years have seen the emergence of an alternative approach based on the replacement of polymers as donor materials by soluble, conjugated single molecules[12], having specific advantages in terms of structural definition, synthesis, and purification.

The second section of this dissertation can be divided in two different research lines. The first one takes origin from the consideration that, in excitonic solar cells, one of

the factors limiting the overall efficiency is the quantum efficiency of the exciton separation into "free" charges. In organic materials, and in the absence of applied fields, this process can only take place with acceptable efficiency at the interface between two different materials, where the difference in chemical (electronic) potential between the two different chemical components plays the role of the driving "field". However, in some materials intrinsic photoconductivity, which includes the photogeneration of free charge carriers without the assistance of an interface, is possible. Such materials were never tried before as components of organic photovoltaic cells. By using a photoconducor [13] as one of the two components of an organic solar cell, we have shown that the use of a material with intrinsic charge photogeneration properties can lead to a significant increase of the exciton dissociation efficiency.

In the second research line, the performance of a new class low molecular weight hydrazonic donors was tested. Such materials exhibit a molecular structure which is similar to the one of compounds that recently[14] showed promising properties in two component organic photovoltaic devices.

Each of the two sections of the dissertation consists of three chapters.

This dissertation is organized as follows:

Section 1

- **Chapter 1** reviews the structure of organic semiconductors, their importance in different applications and their important characteristics, such as charge carrier transport.
- **Chapter 2** reviews the materials used in this section of the dissertation and the experimental techniques used for their characterization, such as those used to measure charge carrier mobility and photoconductivity.
- **Chapter 3** reviews the results of charge carrier mobility and photoconductivity measurements on columnar mesophases formad by novel mesogens.

Section 2

- **Chapter 4** reviews the basic understanding of organic solar cells, the physical processes leading to the final current photogeneration and the factors limiting their efficiency.
- **Chapter 5** reviews the materials used in this section of the dissertation and the experimental techniques to characterize the photovoltaic parameters.
- **Chapter 6** reviews the importance of using a photoconducting donor in bulk heterojunction solar cells. In addition, the photovoltaic results obtained by using two new hydrazonic donors in bulk heterojunction cells are discussed.

References

1. H. Sirringhaus, T. Kawase, R. H. Friend, T. Shimoda, *Science*, 290, 2123-2127, 2000.
2. A. M. Vande Craats, J. M. Warman, A. Fechtenkotter, J. D. Brand, M. A. Harbison, K. Mullen, *Adv. Mater*., 11, 1469, 1999.
3. X. Feng, V. Marcon, W. Pisula, M. R. Hansen, J. Kirkpatrick, F. Grozema, D. Andrienko, K. Kremer, K. Müllen, *Nature Mater.,* 8, 421, 2009.
4. M. Talarico, R. Termine, E. M. Garcia-Frutos, A. Omenat, J.L. Serrano, B. Gomez-Lor, A. Golemme, *Chem. Mater*., 20, 6589, 2008.
5. E. M. Garcia-Frutos, U. K. Pandey, R. Termine, A. Omenat, J. Barbera, J. L. Serrano, A. Golemme, B. Gomez-Lor, *Angew. Chem. Int. Ed*., 50, 7399, 2011.
6. G. Dennler, M. C. Scharber, & C. J. Brabec, *Adv. Mater.,* 21, 1323, 2009.
7. J. Peet, M. L. Senatore, & A. J. Heeger, *Adv. Mater.,* 21, 1521, 2009.
8. S. Gunes, H. Neugebauer and S. Sariciftci, *Chem. Rev.,* 107, 1324, 2007.
9. J. Chen and Y. Cao, *Accounts. Of Chem. Research.,* 42 (11), 1709, 2009.
10. J. Xue, B. P. Rand, S. Uchida and S. R. Forest, *Adv. Mater.,* 17,66, 2005.
11. H. Y. Chen, J. Hou, S. Zhang, Y. Liang, G. Yang, Y. Yang, L.Yu, ,Y. Wu and G. Li, *Nat. Photonics*, 3, 649, 2009.
12. B. Walker, C. Kim, and T. Q. Nguyen,*Chem. Mater*, 23, 470, 2011.
13. M. Ghedini, A. Golemme, I. Aiello, N. Godbert, R. Termine, A. Crispini, M. La Deda, F. Lelj, M. Amati, S. Belviso, *J. Mater. Chem*., 21, 13434, 2011.
14. D. Bagnis, L. Beverina, H. Huang, F. Silvestri, Y.Yao, H. Yan, G. A. Pagani, T. J. Marks, and A. Facchetti*, J. Am. Chem. Soc., 132*, 4074, 2010.

Chapter 1

COLUMNAR MESOPHASE: INTRODUCTION

The objective of this chapter is to review the structure of organic semiconductors, their importance in different applications and their important characteristics, such as charge carrier transport.

1.1Organic semiconductors

Organic semiconductors (OS) are considered among the most useful candidates in the fabrication of electronic devices. Organic semiconductors were first utilized in the industrial fabrication of coatings for xerographic photoreceptors (OPCs)[1]. Currently, organic semiconductors are being used in various electronic devices, such as Organic field effect transistors (OFETs)[2], Bulk heterojunction solar cells (BHJs)[3], Thin film transistors (TFTs) [4,5], and Organic light-emitting diodes (OLEDs)[6]. Unlike inorganic semiconductors, that require the use of expensive and time consuming vacuum processes, most organic semiconductors are solution-processable and can be incorporated into a variety of electronic devices via inexpensive solution process techniques.

The atoms within a molecule or a polymeric chain of an organic semiconductor are held together by σ and π covalent bonds. However, whether polymeric of low molecular weight, the different units (molecules) of organic semiconductors are held together by weak forces. Therefore, such materials are fundamentally different from a conventional inorganic semiconductor, in which the atomic units are connected by covalent bonds. The binding force between two molecules in an organic semiconductor is relatively weak, which makes the resulting electronic bandwidths narrow. The bandwidth for such a case is expected to be about 0.01 to 0.1 eV, which is of the order of thermal energies, phonon energies and polaron binding energies. In inorganic semiconductors, the electronic bandwidths are broad and larger than the other energies mentioned above. The electron-phonon coupling is weak in the inorganic semiconductor, whereas it is strong in the organic semiconductor. The mean free path for the charge carriers in an inorganic

semiconductor may be several times the lattice constant whereas it is of the order of the lattice constant in an organic semiconductor. The charge carrier mobility in the inorganic semiconductor is often higher than the mobility in an organic semiconductor.

Nonetheless, in a single crystal, a close coupling of the π-systems of the molecules can produce remarkable transport properties, including band transport up to room temperature[7]. The charge transport mechanism in polycrystalline and amorphous materials is usually described as a hopping process[8]. Some examples of organic semiconductors are the derivatives of benzene, phenylene, triphenylene, naphthalene and thiophene[9]. These materials show a special potential for the generation and the transport of charge carriers that can be used in molecular electronics.

1.2 Charge carriers photogeneration

The photogeneration process consists in the creation of non-interacting charges of opposite sign, induced by the absorption of light. The first requirement that the material must fulfill is absorption at the working wavelength.

To understand the mechanism leading from an absorbed photon to separated charges, a model involving excitons was proposed[10]. The exciton is an excited state with a distance between charges larger than in the ground state but with the two charges still coulombically interacting. Depending on experimental conditions, the exciton can dissociate completely to give separated charges or, by geminate recombination, can return to the ground state (Fig. 1.1). Since geminate recombination is detrimental for the whole photogeneration process, several studies were conducted in order to understand its physics.

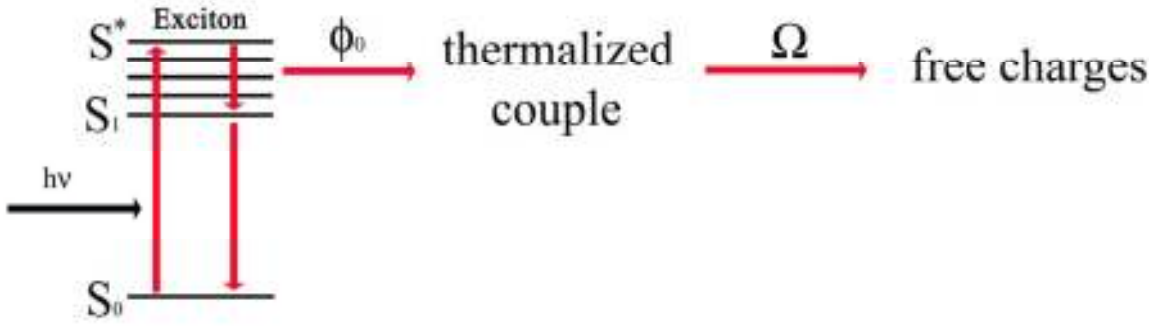

Figure 1.1: Scheme of photogeneration process.

Even if it was studied widely by Poole and Frenkel[11], the description of geminate recombination is usually described by the Osanger's theory of ion-pair dissociation in weak electrolytes[12,13]. This theory, derived by solving the Smoluchowshi equations, describes the photogeneration process as obtained by exciton formation followed by the creation of an intermediate state in which the electron-hole pairs are thermalized (Fig. 1.1) at a typical distance r_0. At this point, if the thermal energy k_BT is comparable to the electrostatic binding energy of the pair, thermal fluctuations can separate the charges. It is possible to define a Coulomb radius r_c as the distance at which thermal and electrostatic energies are equal:

$$r_c = \frac{e^2}{\varepsilon_{DC} k_B T} \tag{1}$$

where CGS units are used. If r_0 is not much shorter than r_c then charge separation can happen, otherwise it is much less probable.

The two parameters describing the separation process are the primary quantum yield ϕ_0 and the escape probability Ω. ϕ_0 represents the probability that an exciton becomes a thermalized couple, while Ω is the probability that an excited charge moves beyond the Coulomb radius and avoids recombination. From Osanger's model it is possible to obtain the analytical expression for Ω[14]:

$$\Omega(r,\theta,E) = e^{-A} e^{-B} \sum_{n=0}^{\infty} \sum_{m=0}^{\infty} \frac{A^m B^{m+n}}{m!(m+n)!} \tag{2}$$

where, in CGS units:

$$A = \frac{e^2}{\varepsilon_{DC} \; k_B T r}$$

$$B = (1+\cos\theta)\frac{eEr}{2k_B T} \tag{3}$$

where E is the applied electric field, e is the elementary charge, ε_{DC} is the static dielectric constant, k_B is the Boltzman constant, T is the temperature and θ is the polar angle between applied field and the direction connecting the two charges[14].

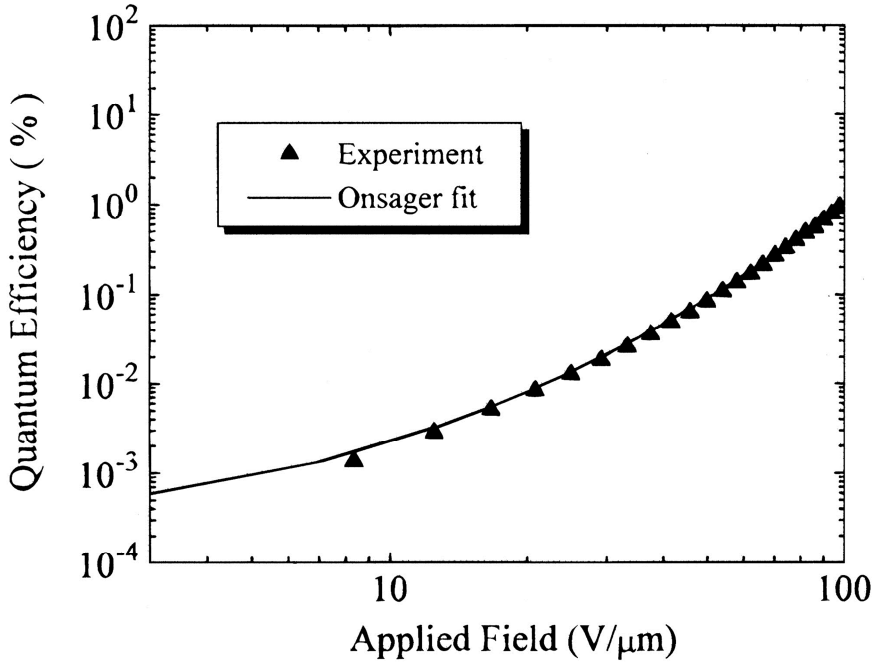

Figure 1.2: Photogeneration efficiency measured as function of the applied field in a film of PVK/DR1/TNF.

Defining the quantum efficiency as $\phi(E,r_0) = \phi_0\,\Omega$, it is interesting to derive the dependence of ϕ on the applied field E. Under the assumption that the distribution of thermalized pairs is isotropic, Mozumder[15,16] integrated the product $\phi_0\Omega$ over space, obtaining an analytic solution for the photogeneration efficiency $\phi(E,r_0)$:

$$\phi(E) = \phi_0\left(1 - \xi^{-1}\sum_0^\infty A_n(\kappa)A_n(\xi)\right) \tag{4}$$

where:

$$A_n(x) = A_{n-1}(x) - \frac{x^n e^{-x}}{n!} \qquad A_0(x) = 1 - e^{-x}$$

$$\kappa = \frac{r_c}{r_0} \qquad \xi = \frac{e r_0 E}{k_B T}$$

Eq. (4) is converging just after several tens of iterations, making it possible to derive the dependence of photogeneration from r_0 and electric field E. For example, if the thermalization radius r_0 is within the 10-30 Å range, typical for organic materials, the photogeneration efficiency ϕ varies strongly with the electric field and it can increases by

several orders of magnitude by increasing the electric field from 10 to 100 V/μm (Fig. 1.2).

1.3 Charge carriers transport

After photogeneration, we consider the transport of carriers over macroscopic distances. Even though in some cases ionic transport can be important, the most common occurrence is electronic mediated transport. Transport mechanisms depend on the nature of the material: in crystals, the ordered structure allows electronic band formation and, consequently, easy movement of the photogenerated electrons (holes) while in organic amorphous materials the localization of electronic levels over each molecule slows down this process. Photogenerated charges must "hop" between localized levels with a transport mechanism that should be considered not as a continuous process but rather as a series of discrete events. Fig. 1.3 is a schematic picture describing the hopping mechanism for the case of hole transport.

In amorphous organics, specific molecular moieties are responsible for charge generation and charge transport. Usually the process can be summarized by considering photon absorption by a sensitizer moiety, which injects a "free" hole in the HOMO levels of the transport moiety. Holes generated in this fashion hop between transport sites until they are trapped or recombine.

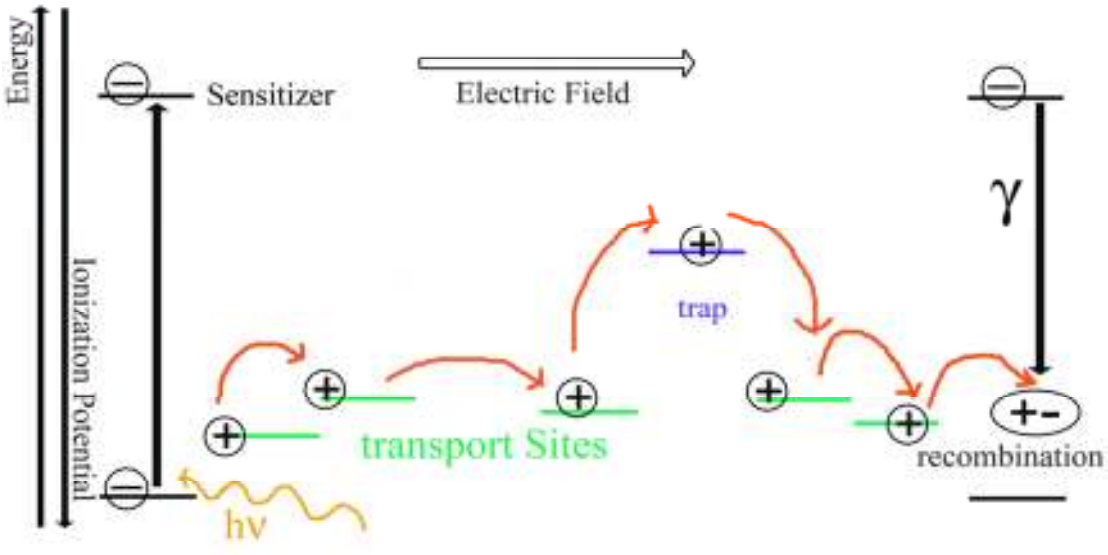

Figure 1.3: Schematic representation of hole transport and trapping mechanism.

The parameter that typically describes the transport process is the drift mobility μ, defining the ratio between the drift velocity $\vec{v}$ of the moving charges and the applied electric field $\vec{E}$:

$$\vec{v} = \mu\vec{E} \tag{5}$$

In organics, due to the nature of the trapping and de-trapping processes, drift mobility can be analyzed in terms of its Poole-Frenkel dependence on electric field[11,16,17]:

$$\mu = \mu_0 \exp(-\frac{F_o - \beta E^{1/2}}{k_B T_{eff}}) \tag{6}$$

where:

$$T_{eff} = \left(\frac{1}{T} - \frac{1}{T_0}\right)^{-1}$$

and β is a constant coefficient depending on the transport system, F_0 the zero-field activation energy, E the applied electric field, μ_0 a parameter depending on the material, T_0 a particular temperature value at which the curves μ vs. T intersect for all applied fields. Despite this empirical relation is one of the most used to fit experimental data[18], it overestimates drift mobility by several orders of magnitude because it considers a trap free transport mechanism[19]. Further enhancements were necessary in order to improve the correlation between theoretical and experimental data.

A fundamental work in the field of intermolecular hopping transport is due to Scher and Montroll[20]. They analyzed the problem by using a random walk model and considering carrier hopping between regularly spaced sites. Even if the model fits experimental data, some discrepancies have been found and new models were elaborated[21]. Among the most recent ones, the so called disorder formalism is already widely used. It considers a Gaussian distribution of the positions[22] and of the energies[23,24] (Fig. 1. 4) of the hopping sites and in addition that:

- electrons and phonons do not interact;
- no correlation exists between successive hops;
- the hopping rates ν_{AB} between states A and B with energies ε_A,ε_B and position R_A e R_B can be expressed in the Miller-Abrahamas form:

$$\nu_{AB} = \nu_0 \exp(-2\gamma|R_A - R_B|) \cdot \Theta \tag{7}$$

where:

$$\Theta = \exp(-\frac{\varepsilon_A - \varepsilon_B}{k_B T}) \quad \text{if} \quad \varepsilon_A > \varepsilon_B$$

or

$$\Theta = 1 \quad \text{if} \quad \varepsilon_A < \varepsilon_B$$

In Eq. (7) ν_0 is a frequency pre factor and γ is an inverse wave function decay length[22].

It is possible to observe that the probabilities of hopping to higher and lower energy sites are different. According to the disorder formalism model, if σ and Σ are the standard deviations of the Gaussian distributions for energy and position, respectively, the drift mobility μ is given by:

$$\mu = \mu_0 \exp\left[-\left(\frac{2}{3}\frac{\sigma}{k_B T}\right)^2\right] \exp\left[C\sqrt{E}\left(\frac{\sigma^2}{k_B^2 T^2} - \Sigma^2\right)\right] \tag{8}$$

where *C* is an empirical constant.

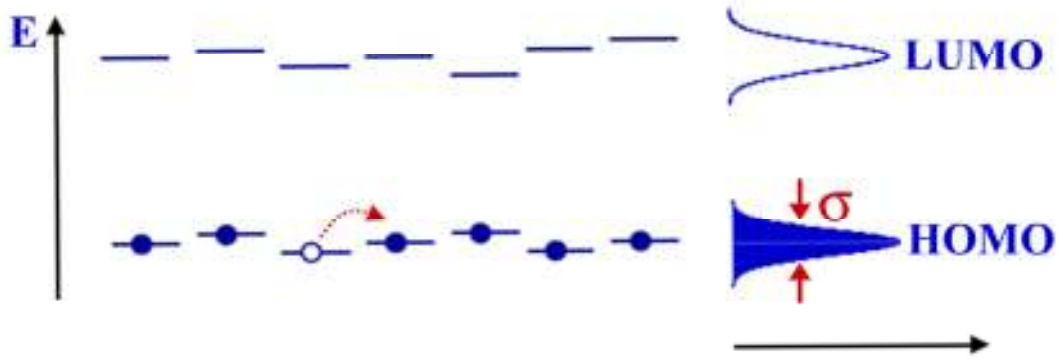

Figure 1.4. Energetic disorder in transporting levels.

1.4 From single crystal to liquid crystal as organic semiconductors

Single crystals of organic semiconductors may possess high mobilities. However, there are practical limitations in using them, due to the difficulty in the growth and the processing of defect free bulk single crystals and in their incorporation into device structures. In an actual crystal, different types of defects are always present, e.g., intrinsic point defects (vacancies, interstitials), extended defects (dislocations, stacking faults,

lattice distortions, grain boundaries) and chemical impurities (substitutional atoms or interstitial atoms or molecules). For device applications, such as photoreceptors for xerographic copiers and organic electroluminescent devices, organic semiconductors are required to have large area uniformity for the charge carrier transport. It is very difficult to achieve such uniformity in the single crystals. This type of uniformity can be achieved only by films of polycrystalline, amorphous, or liquid crystalline semiconductors.

The transport of charge carriers in both organic and inorganic materials decreases considerably upon decreasing the order, from single crystal to amorphous solid. In the case of silicon, its charge carrier mobility decreases from > 1000 cm^2 / V s in the crystal to ~ 1 cm^2 / V s in its amorphous form. An example of an organic material is pentacene. According to Akinori Saeki et al.[25], the photoinduced charge carrier mobility of pentacene thin films prepared by thermal vapor deposition is around 0.7 cm^2 / V s whereas its charge carrier mobility in a highly purified single crystal form is 35 cm^2 / V s. This is a huge deterioration in the charge carrier mobility in pentacene when its form is changed from the single crystal to the deposited amorphous material. This is a common problem encountered when using amorphous or non-crystalline organic semiconductors. To overcome this problem, liquid crystal materials were developed as an alternative to inorganic semiconductors, as they show both a liquid-like structural flexibility and a crystal-like molecular arrangement that favors large area uniformity. Moreover, it is widely recognized that the self-organization of liquid crystalline phases is a key strategy to control the order and packing of organic semiconductors and to suppress defect formation. In addition, the possibility of self-healing of defects is an added advantage of mesophases when considering their use in molecular electronics.

1.5 Liquid crystals

An intermediate state of aggregation of a substance between the crystalline solid and the amorphous liquid[26] is known as a liquid crystalline phase. A substance in this state exhibits strongly anisotropic properties as well as a certain degree of fluidity, which, in some cases, may be comparable to that of an ordinary liquid. The very first observations of liquid crystalline or mesomorphic behaviour were observed back in the 19^{th} century by Reinitzer[27] and Lehmann[28]. Many thousands of organic compounds are currently known to form liquid crystals. Depending on the molecular structure, a solid

may pass through one or more mesophases before it is transformed into an isotropic liquid. Transitions to these intermediate states may be induced by purely thermal processes (thermotropic mesomorphism) or also by the influence of solvents (lyotropic mesomorphism). Lyotropic liquid crystals were not studied in this dissertation.

Liquid crystals can be also divided into two types on the basis of the mesogen's structure. Liquid crystal formed by rod-like mesogens are called calamitic liquid crystals while those formed by disk-like mesogens are called discotic LC.

1.5.1 Thermotropic liquid crystals.

Calamitic liquid crystals The majority of compounds showing thermotropic mesophases are formed by rod-like shaped mesogens. The term calamitic has been used to describe such liquid crystals, in order to distinguish them from Discotic liquid crystals (DLCs) formed by disk-like molecules.

A typical structure of a calamitic LCs is schematically shown in Fig. 1.5 a. Where x and x' are side groups, A and B are aromatic rings and, L is a linking group. The length and flexibility of the side group affects the type of LC phases and the phase transitions. Some common side groups are alkyl groups (C_nH_{2n+1}) and alkoxy groups ($C_nH_{2n+1}O$). Most LC mesogens contain two or more aromatic rings. Those aromatic rings can be benzene, phenyl, pyridine, thiophene, etc. or combinations of these. The linking group makes an important contribution to the phase transition and physical properties, such as birefringence. In Fig. 1.5 b, a typical example of the calamitic LC is shown.

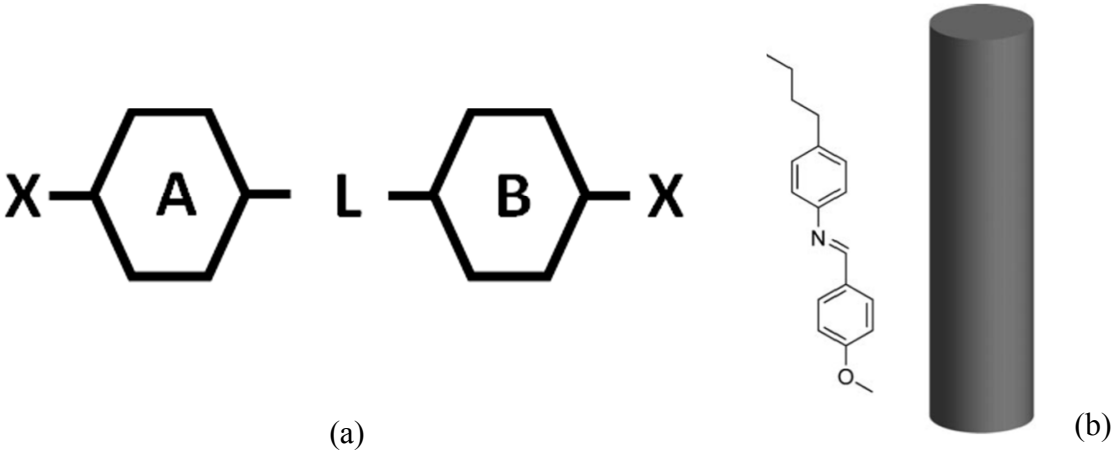

(a) (b)

Figure 1.5: (a) The basic structure of calamitic liquid crystals, (b) a typical example of calamitic liquid crystal .

These are further classified into three types, namely nematic, smectic and cholesteric depending on the nomenclature proposed originally by Friedel[29].

The nematic liquid crystals mesophase is characterized by molecules which tend to orient along a particular direction with certain degree of long range orientational order but without any particular positional order. The preferred direction is characterized by an average direction of all molecules, which is called the director (n), Fig. 1.6. Nematic phase differs from an isotropic liquid in that molecules are spontaneously oriented with their long axes approximately parallel to each other. The preferred direction usually varies from point to point in the medium, but a uniformly aligned sample is optically uniaxial and highly birefringent. The mesophase owes its fluidity to the ease by which molecules slide past one another while still retaining their parallelism.

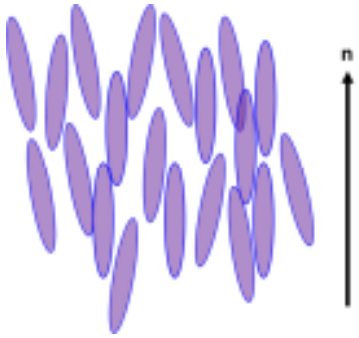

Figure 1.6: Schematic representation of the molecular arrangement in a nematic phase.

Smectic liquid crystals (Sm) have layered structures and a variety of molecular arrangements are possible within each layer. The smectic liquid crystal mesophases can be subdivided into a number of different types[30,31]. Some of them are SmA, SmB (hexatic), SmB (crystal), SmC, SmE, SmF, SmG, SmH, SmI, SmJ, SmK, etc.

In SmA, the molecules are located within the liquid-like layers with the director perpendicular on average to the plane of the layer. Therefore, the layer thickness d is roughly the same as the molecular length l (Fig. 1.7). Even if it is more viscous than the nematic, this mesophase exhibits still a certain degree of fluidity.

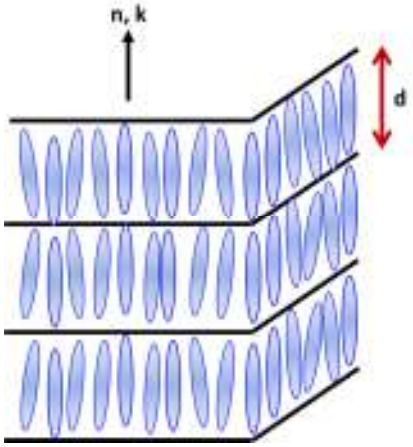

Figur 1.7: Model structure of the SmA phase. The director **n**, which is the average local direction of the long molecular axis, is oriented parallel to the smectic layer normal **k**, while within a smectic layer the centers of mass of the molecules are isotropically distributed.

In SmC, the molecules in the layers are parallel and tilted in arrangement with respect to the normal of the layers by a tilt angle θ (Fig. 1.8). Hence the layer thickness of SmC is d = l cosθ. In both smectic phases, the molecules have no particular positional order within the layer. There is a liquid-like motion of the rods in each layer and no correlation of the molecular positions from one layer to the next. In both cases the interlayer attractions are weak compared with the lateral forces between molecules, hence the layers can easily slide.

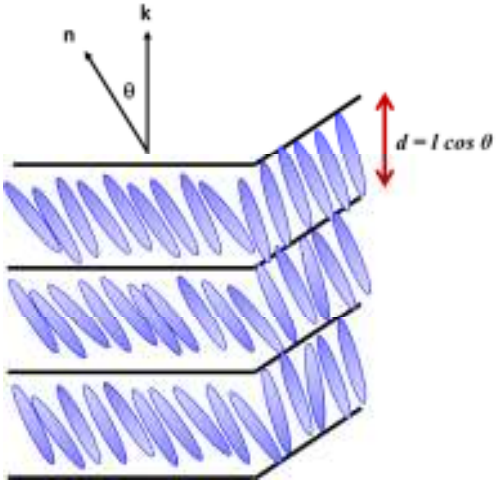

Figure 1.8: Model structure of the SmC phase. The director **n** is tilted with respect to the smectic layer normal **k** at an angle θ, the director tilt angle. The centres of mass of the molecules are isotropically distributed within the layer.

Some smectic phases (e.g. Sm_B, Sm_E, Sm_G, Sm_H, Sm_J, and Sm_K) have three-dimensional long-range positional order as in crystals, however with weak interlayer forces. Other phases, referred to as hexatic phases, have three-dimensional long-range "bond-orientational" order but without any long-range positional order[32,33]. There are also chiral versions of all the tilted smectic phases where the director rotates about the perpendicular to the planes in going from one layer to the next (Fig. 1.9).

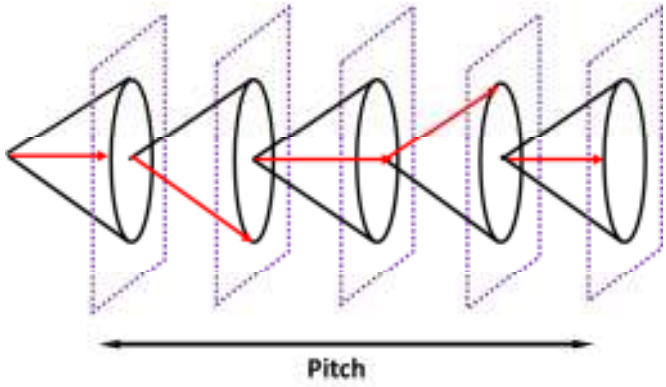

Figure 1.9: Structure of the SmC* phase. The planes represent the smectic layers and the arrows denote the directors.

A cholesteric (N*) liquid crystal mesophase is chiral, sometime also referred as twisted nematic: the molecules have left or right handedness. As a consequence, when molecules align in layers, this causes the director orientation to rotate slightly between the layers, eventually bringing the molecules back into the original orientation. The distance required to achieve this is known as the *pitch* of the twisted nematic, as seen in Fig. 1.10. Racemic mixtures result in a helix of infinite pitch which corresponds to the true nematic. The twist energy represents only a small part of the total energy associated with the parallel alignment of the molecules, so that when a small quantity of an optically active substance is added to a nematic, the mixture adopts a helical configuration.

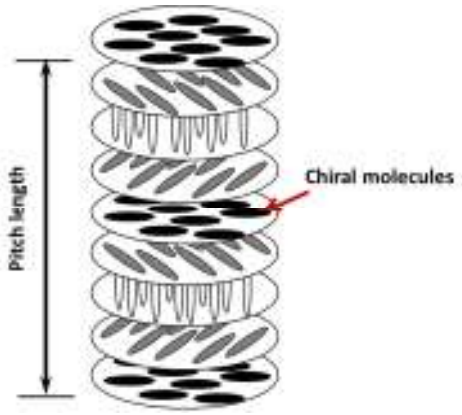

Figure 1.10: A cholesteric liquid crystal: schematic representation of the helical structure.

1.5.2 Discotic liquid crystals (DLCs).

The first liquid crystals of disc-shaped molecules, broadly known as discotic liquid crystals (DLCs), were prepared and identified in 1977 by S. Chandrasekhar[34]. In general, DLC mesogens consist of flat and rigid aromatic cores surrounded by flexible chains. Flexible chains are connected to the core by different linkages such as ether, ester, benzonate, alkyne etc. Fig. 11 shows a general molecular architecture for discotic mesogens.

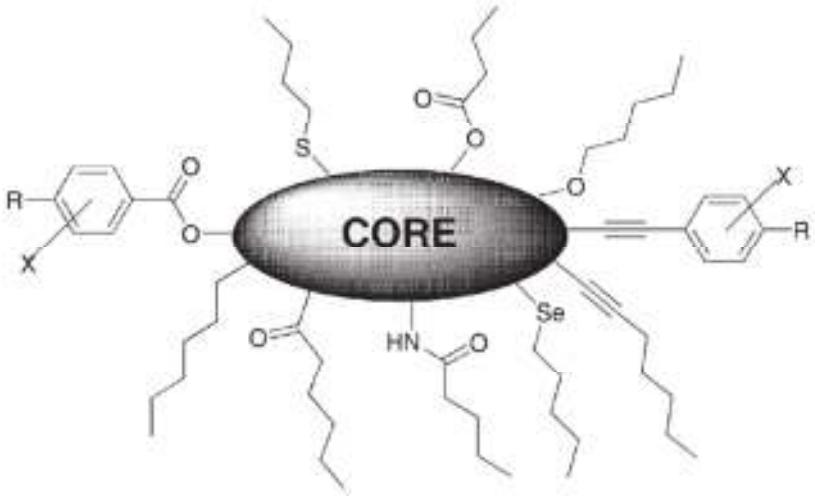

Figure 1.11: A general molecular structure of discotic mesogens.

Mesophases formed by disc shaped molecules are primarily of three types: (1) nematic, (2) columnar and (3) lamellar.

The nematic phases of disc-shaped molecules can be subdivided into three types: (a) nematic discotic (b) chiral nematic and (c) nematic columnar. In the nematic discotic

phase, the molecules stay more or less parallel, having orientational order but no long-range positional order (Fig. 1.12 a).

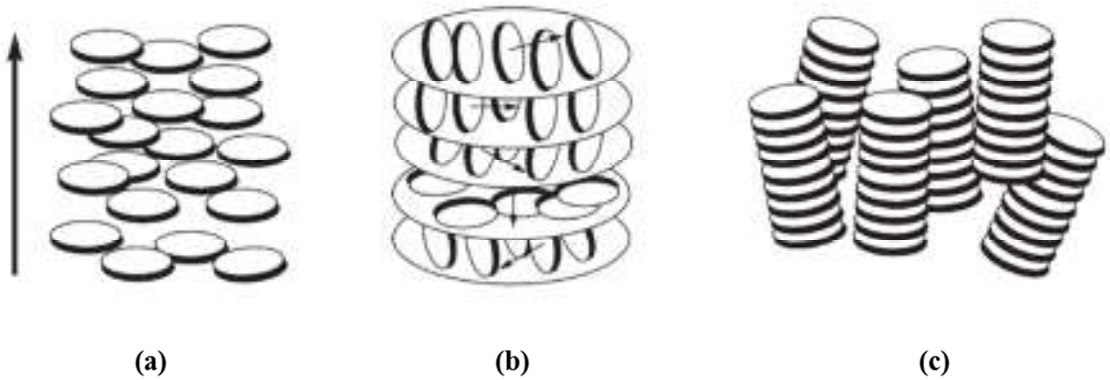

Figure 1.12. : Schematic representation of (a) discotic nematic (b) helical structure of chiral nematic phase and (c) nematic columnar phase.

The nematic phase of disc-shaped molecules is usually not miscible with the nematic phase of rod-shaped molecules, though they exhibit similar fluid Schlieren textures[35]. However, unlike the usual calamitic nematic, the discotic nematic phase is optically negative, the director being the preferred axis of orientation of the disc-normals (or the short molecular axes). The symbol ''N_D'' is used to denote discotic nematic mesophase.

Like the chiral rod-shaped nematic or cholesteric phase, the chiral discotic nematic mesophase N_D* also exists. The mesophase occurs in mixtures of discotic nematic and mesomorphic or non-mesomorphic chiral dopants, as well as in pure chiral discotic molecules[36,37]. The helical structure of the chiral discotic nematic phase is schematically shown in Fig. 1.12 b.

The nematic columnar N_{Col}, phase is characterized by a columnar stacking of the molecules. However, these columns do not form two-dimensional lattice structures. They display a short-range positional order and an long-range orientational order, see Fig. 1.12 c.

In columnar mesophases, molecular assemble themselves one on top of the other in columns which are packed parallel to each other in a two-dimensional lattice. The molecules within a column may be arranged in a regularly ordered manner or disordered. Depending on the order in the molecular stacking in the columns and on the two-

dimensional lattice symmetry of the column packing, columnar mesophases may be classified in five classes: (a) columnar hexagonal phase, (b) columnar rectangular, (c) columnar oblique phase, (d) columnar plastic phase, and (e) columnar helical phase.

The columnar hexagonal phase is characterized by an hexagonal packing of the columns. Hexagonal mesophases are often denoted as Col_{ho} or Col_{hd}, where h stands for hexagonal and o or d for ordered or disordered stacking of the molecules. In both the cases fluidity exists; only the positional correlation length within the columns are different and, therefore, it is recommended to discontinue o and d subscripts. The recommended abbreviation for columnar hexagonal phase is ‘‘Col_h’’. Fig. 1.13a illustrates the molecular packing in a Col_h mesophase.

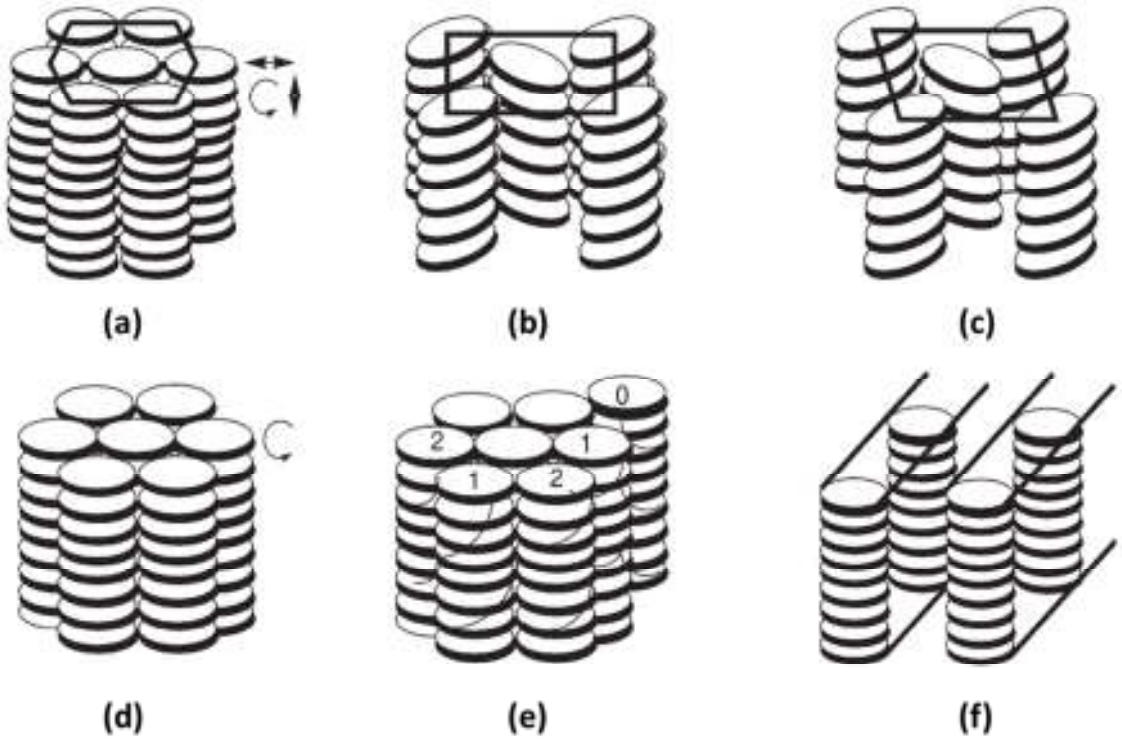

Figure 1.13:. Schematic representation of (a) hexagonal columnar phase (b) rectangular columnar phase (c) columnar oblique phase (d) columnar plastic phase (e) helical phase and (f) columnar lamellar phase.

The columnar rectangular mesophase consists of the stacking of the aromatic cores of the molecules in columns surrounded by the disordered aliphatic chains and packed in a rectangular fashion (Fig. 1.13b). The columnar rectangular phase is denoted

by Col_r. In the columnar oblique mesophase, the columns are arranged with an oblique unit cell (Fig. 1.13c).

The columnar plastic phase, denoted as Col_p, has been identified recently[38]. The phase is characterized by three-dimensional crystal-like order in an hexagonal lattice, while the discs within the columns are able to rotate about the column axis (Fig. 1.13d). In the Col_h phase instead, structural disorders such as non-parallel arrangement of the discs, longitudinal and lateral displacements and rotation around the columnar axis occur, while such motional freedom of discs in the Col_p phase is restricted.

An exceptional mesophase structure with helical order (Fig. a) has been demonstrated for a triphenylene derivative, namely hexahexylthiotriphenylene (HHTT)[39].In this so-called H phase, helical columns develop which interdigitate in groups of three columnar stacks. The H phase found in HHTT is illustrated in Fig. 1.13e.

A layered structure is known to exist for mesophases of certain discotic compounds, e.g. bis (p-n-decylbenzoyl)methanato copper(II), some perylene derivatives, etc.[40] Such a columnar lamellar mesophase, which is denoted by the symbol Col_L, is shown in Fig. 1.13f. Another columnar mesophase with two-dimensional square lattice has recently been described in some metallomesogens[41].

1.6 Discotic mesophases as organic semiconductors for molecular electronics

In columnar mesophases, transport of the charge carriers in directions perpendicular to the columns is more hindered than transport parallel to the columns, because electrons have to cross “insulating” hydrocarbon regions, with a width in the 15-20 Å range. N Boden et al [42] estimated that the charge mobility along the direction parallel to the columns is approximately two orders of magnitude higher than that in the perpendicular direction. Therefore, charge transport is highly anisotropic.

This transport behavior, and the previously mentioned advantages of liquid crystals, make the discotic mesophases useful materials for several technological applications, such as photocopying, electrophotography, nonlinear optics, molecular electronics, photoconducting systems, light emitting diodes, photovoltaic solar cells, optical data storage devices, hybrid computer chips for molecular electronics, etc.

The charge transport mechanism in discotic mesophase seems to be an incoherent hopping process, as shown by experiments on the frequency dependence of the conductivity parallel to the columnar stacks[43, 44]. The disc-like molecules self-assemble into columns, with a significant intermolecular overlap of delocalized π-electrons, thereby providing quasi-one-dimensional channels for facile charge transport. In the past decade, charge transport in various columnar discotic mesophases has been investigated by using several experimental techniques, such as time-of-flight (TOF)[45], space charge limited current (SCLC)[46], pulse radiolysis time-resolved microwave conductivity technique (PR-TRMC)[47] and the field-effect transistor geometry (FET)[48, 49].

Moreover, we know that the inherent fluidity of liquid crystals induces advantageous properties, such as the ability to self-heal structural defects and easier alignment and processing from the isotropic phase. However, fluidity is also associated with intra stack dynamism of the functional units, that reduces carrier mobility in the bulk. Therefore, the preferred strategy for improving mobility in discotic mesophases has been the enhancement of the intermolecular order within the stacks. To achieve this goal, different approaches have been explored, such as:

1. Linking the cores to peripheral alkylic chains through bulky moieties[50,51,52]
2. Introducing functional groups providing directional interactions[53,54,55] (e.g. hydrogen bonds) or even
3. Inducing helical columnar arrangements that provide a higher degree of order.[50,56]

However, charge carrier mobility does not depend just on the degree of order, but also on the stacking distance between molecules within the columnar organization, which usually decreases with increasing order. Therefore, the research on columnar discotic mesophases has attempted to introduce chemical modifications designed to increase the ordering along the column [57, 58, 59]. In other words, the stacking distance within the columnar organization can also be altered by chemical modifications, as columnar ordering and stacking distance are correlated.

In rescent years, charge carrier mobility measurements in many discotic liquid crystalline mesophases have been reported. The mesogens used displayed several different types of discotic cores, including benzene,[60-64] pyridine,[65] triazine,[62,64,66] triphenylene,2,12 diazatriphenylene,[67] hexaazatriphenylene,[68] pyrene,[69] dibenzo[g,p]chrysene,[70,71] dibenzonapthacene,[72] tristriazolotriazine,[73] rufigallol,[74-76]

truxene,[77] Triazatruxene/Triindole core[78,79] tricycloquinazoline,[80,81] hexaazatrinaphthylene (HATNA),[82,83] perylene,[84] coronene diimide,[85] phthalocyanine (Pc),[86-90] porphyrin,[91,92] quin-oxalinophenanthrophenazine (TQPP),[93,94] pyrazinopyrazinoquinoxalinophenanthrophenazine (TPPQPP),[94] dodecaazatrianthracene (DATAN),[94] and hexa-perihexabenzocoronene (HBC),[95]. The highest charge carrier mobilities are in the 0.2 - 0.5 $cm^2\ V^{-1}\ s^{-1}$ range.

The objective of this section of the dissertation is to study the charge carrier transport properties in columnar discotic liquid crystals formed by the megogens of triindole core. The meshophases exhibit a considerably smaller core than in the usual discotics as described above.

The structure of the triindole core is shown in Fig. 1.14, It is basically a disk-like molecule[97] with C3-symmetry, that can be considered as an extended π-system in which three carbazole units share an aromatic ring. The chemical structure resemblance with the well-known hole transporter carbazole. Carbazole-based compounds have been extensively studied due to their ability to transport holes[98-101]. Having a π-extended structure, renders triindoles attractive candidates in the search of new systems for organic electronics, as charge transport active layers.

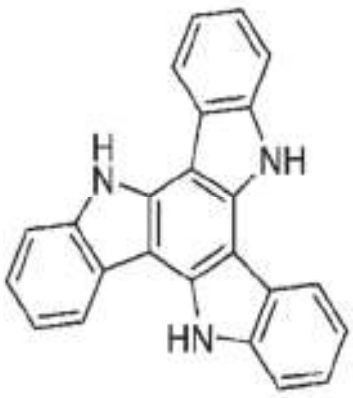

Figure 1.14: Structure of 10,15-dihydro-5H-diindolo[3,2-a:3′,2′-c]carbazole (triindole)

A generalised schematic of a triindole columnar mesogen is shown in Fig. 1.15 where R indicates a peripheral chain, including the linker, and R' is a nitrogen substituent.

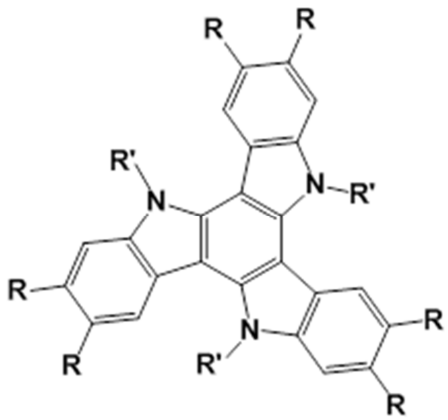

Figure 1.15: Schematic of the discotic mesogens formed by triindole core

The results of charge transport properties of columnar mesophases formed by this new triindole mesogens will be discussed in the results and discussion section foucusing :

1. The effect of different linkers on the charge mobility.
2. Effect of the different nitrogen substituents on the charge mobility.

BIBLIOGRAPHY

1. P.M. Borsenberger, D. S. Weiss, Organic Photoreceptors for Xerography, Marcel Dekker Inc., New York, 1998.
2. C.J. Brabec, N.S. Sariciftci, J.C. Hummelen, *Adv. Funct. Mater.*, 11, 15, 2001.
3. C.D. Dimitrakopoulos, P.R.L. Malenfant, *Adv. Mater.*, 14, 99, 2002.
4. M. Kitamura, Y. Arakawa, *J. Phys.: Condens. Matter*, 20, 184011, 2008.
5. S. Allard, M. Forster, B. Souharce, H. Thiem, U. Scherf, *Angew. Chem., Int. Ed.*, 47, 4070, 2008.
6. O.D. Jurchescu, J. Baas, T.T.M. Palstra, *Appl. Phys. Lett.*, 84, 16, 2004.
7. M. Funahashi, J.-I. Hanna, *Adv. Mater.*, 17, 594, 2005.
8. D. Adam, F. Closs, T. Frey, D. Funhoff, D. Haarer, H. Ringsdorf, P. Shcuhmacher, K. Siemensmeyer, *Phys. Rev. Lett.*, 70, 457, 1993.
9. F. Gamier, A. Yassar, R. Hajlaoui, G. Horowitz, F. Deloffre, B. Serve, S. Ries, P. Alnott, *J. Am. Chem. Soc.*, 115, 8716, 1993.
10. S. Chandrasekhar, B. K. Sadashiva, K. A. Suresh, *Pramana*, 9, 471, 1977.
11. C. Mauguin, *C. R. Acad. Sci.*, 156, 1246, 1911.
12. H. Zocher, K. Coper, *Z. Phys. Chem.*, 132, 295, 1928.
13. P. Chatelain, *Bull. Soc. Fr. Min.*, 60, 300, 1937.
14. Y.B. Kim, H.S. Kim, J.S. Choi, M. Matuszcyk, H. Olin, M. Buivydas, P. Rudquist, *Mol. Cryst. Liq. Cryst.*, 262, 89, 1995.
15. J. L. Janning, *Appl. Phys. Lett.,* 21, 173, 1972.
16. X. Quintana, J.M. Oton, M. Brunet, R. Lotoux, *Ferroelectrics,* 244, 275, 2000.
17. K. Skarp, G. Andersson, *Ferroelectric Lett.,* 6, 67, 1986.
18. C.W. Oseen, *Trans. Faraday Soc.*, 29, 883, 1933.
19. H. Zocker, *Trans. Faraday Soc.,* 29, 945, 1993.
20. F.C. Frank, *Discuss. Faraday Soc.*, 25, 19, 1958.
21. S.T. Lagerwall, Ferroelectric and Antiferroelectric Liquid Crystals, Wiley-VCH, Weinheim, 1999.
22. A. Saupe, *Mol. Cryst. Liq. Cryst.*, 7, 59, 1969.
23. Orsay Group on Liquid crystals, *Solid State Commun.*, 9, 653, 1971.
24. S.T. Lagerwall, I. Dahl, *Mol. Cryst. Liq. Cryst.*, 114, 151, 1984.
25. A. Saeki, S. Seki, S. Tagawa, J. *Appl. Phys.*, 100, 023703, 2006.
26. S. Chandrasekhar, Liquid Crystals, Cambridge University Press, Cambridge, 1992.
27. F. Reinitzer, *Liq. Cryst.*, 5, 7, 1889.
28. O. Lehmann, *Z Physikal. Chem.*, 4, 462, 1889.
29. G. Friedel, *Ann. Physique*, 18, 273, 1922.
30. J. Leadbetter, "Thermotropic Liquid Crystals, Wiley, Chichester, 1987.
31. P.S. Pershan, Structure of Liquid Crystal Phases, World Scientific, Singapore, 1988.
32. R.J. Birgeneau, J.D. Litster, *J. de Physique Lettres*, 39, 399, 1978.
33. R. Pindak, D.E. Moncton, S.C. Davey, J.W. Goodby, *Phys. Rev. Lett.*, 46, 1135, 1981.
34. S. Chandrasekhar, B.K. Sadashiva, K.A. Suresh, *Pramana*, 9, 471, 1977.
35. M. Baron, *Pure Appl. Chem.*, 73, 845, 2001.

36. C.V. Yelamaggad, V. Prasad, M. Manickam, S. Kumar, *Mol. Cryst. Liq. Cryst*., 325, 33, 2001.
37. G. Heppke, D. Kruerke, C. Lohning, D. Lotzsch, D. Moro, M. Muller, H. Sawade, *J. Mater. Chem.*, 10, 2657, 2000.
38. B. Glusen, W. Heitz, A. Kettner, J.H. Wendorff, *Liq. Cryst.*, 20, 627, 1996.
39. E. Fontes, P.A. Heiney, W.H. De Jeu, *Phys. Rev. Lett.*, 61, 1202, 1988.
40. M. Giroud-Godquin, J. Billard, *Mol. Cryst. Liq. Cryst*., 66, 147, 1981.
41. K. Hatsusaka, K. Ohta, I. Yamamoto, H. Shirai, *J. Mater. Chem.*, 11, 423, 2001.
42. N. Boden, R.J. Bushby, J. Clements, *J. Chem. Phys*., 98, 7, 1993.
43. I. Bleyl , C. Erdelen , H.-W. Schmidt, D. Haarer, *Phil. Mag. B*, 79, 463, 1999.
44. N. Boden, R.J. Bushby, J. Clements, B. Movaghar, *Phys. Rev. B*, 52, 18, 1995.
45. T. Mori, E. Sugimura, T. Mizutani, *J. Phys. D: Appl. Phys*., 26, 452, 1993.
46. P.W.M. Blom, M.J.M. de Jong, M.G. van Munster, *Phys. Rev., B55, R656*, 1997.
47. A.M. Van de Craats, J.M. Warman, *Adv. Mater*., 13, 130, 2001.
48. D. Poplavskyy, J. Nelson, *J. Appl. Phys*., 93, 341, 2003.
49. V. Duzhko, A. Semyonov, R.J. Twieg, K.D. Singer, *Phys. Rev. B*, 73, 2006.
50. I. Fischbach, T. Pakula, P. Minkin, A. Fechtenkötter, K. Müllen, H.W. Spiess, K. Saalwachter, *J. Phys. Chem. B,* 106*,* 6408, 2002.
51. J.S. Wu, M.D. Watson, L. Zhang, Z.H. Wang, K. Müllen *J. Am. Chem. Soc.*, 126, 177, 2004.
52. M. van de Craats, J.M. Warman, *Synth. Metals.,* 121, 1287, 2001.
53. R.I. Gearba, M. Lehmann, J. Levin, D.A. Ivanov, M.H.J. Koch, J. Barberá, M.G. Debije, J. Piris, Y.H. Geerts, *Adv. Mater.* 15, 1614, 2003.
54. C. Lavigueur, E.J. Foster, V.E. William, *J. Am. Chem. Soc.*, 130, 11791, 2008.
55. M.L. Bushey, T.-Q. Nguyen, W. Zhang, D. Horoszewski, C. Nuckolls, *Angew. Chem. Int. Ed.*, 43, 5446, 2004.
56. D. Adam, P. Schuhmacher, J. Simmerer, L. Häussling, K Siemensmeyer, K.H. Etzbach, H. Ringsdorf, D. Haarer, *Nature*, 371, 141, 1994.
57. M.T. Allen, S. Diele, K.D.M. Harris, T. Hegmann, B.M. Kariuki, D. Lose, J.A. Preece, C. Tschierskec, *J. Matt.. Chem*., 11, 302, 2001.
58. N. Boden, R.J. Bushby, A.N. Cammidget, G. Headdock, *J. Mater. Chem*., 5, 2275, 1995.
59. M. Funahashi, J.-I. Hanna, *Appl. Phys. Lett*., 76, 2574, 2000.
60. G. Hennrich, E. Cavero, J. Barbera, B. Gomez-Lor, R.E. Hanes, M. Talarico, A. Golemme, J.L. Serrano, *Chem. Mater*., 19, 6068, 2007.
61. M.J. Jeong, J.H. Park, C. Lee, J.Y. Chang, *Org. Lett*., 8, 2221, 2006.
62. Y.-D. Zhang, K.G. Jespersen, M. Kempe, J.A. Kornfield, S. Barlow, B. Kippelen, S.R. Marder, *Langmuir*, 19, 6534, 2003.
63. A. Grafe, D. Janietz, T. Frese, J.H. Wendorff, *Chem. Mater*., 17, 4979, 2005.
64. H. Meier, M. Lehmann, H.C. Holst, D. Schwoppe, *Tetrahedron,* 60, 6881, 2004.
65. A.-J. Attias, C. Cavalli, B. Donnio, D. Guillon, P. Hapiot, J. Malthete, *Mol. Cryst. Liq. Cryst*., 415, 169, 2004.
66. K. Pieterse, A. Lauritsen, A.P.H.J. Schenning, J.A.J.M. Vekemans, E.W. Meijer, *Chem. Eur. J*., 9, 5597, 2003.
67. M. Ichihara, H. Suzuki, B. Mohr, K. Ohta, *Liq. Cryst*., 34, 401, 2007.
68. O. Roussel, G. Kestemont, J. Tant, V. de Halleux, R.G. Aspe, J. Levin, A. Remacle, I.R. Gearba, D. Ivanov, M. Lehmann, Y. Geerts, *Mol. Cryst. Liq. Cryst*., 396, 35, 2003.

69. A. Hayer, V. de Halleux, A. Koehler, A. El-Garoughy, E.W. Meijer, J. Barbera, J. Tant, J. Levin, M. Lehmann, J. Gierschner, J. Cornil, Y.H. Geerts, *J. Phys. Chem. B*, 110, 7653, 2006.
70. R. Chaudhuri, M.-Y. Hsu, C.-W. Li, C.-I. Wang, C.-J. Chen, C.K. Lai, L.-Y. Chen, S.-H. Liu, C.-C. Wu, R.-S. Liu, *Org. Lett*., 10, 3053, 2008.
71. S. Kumar, S.K. Varshney, *Mol. Cryst. Liq. Cryst*., 378, 59, 2002.
72. S. Kumar, J.J Naidu, D.S.S. Rao, *J. Mater. Chem*., 12, 1335, 2002.
73. R. Cristiano, H. Gallardo, A.J. Bortoluzzi, I.H. Bechtold, C.E.M. Campos, R.L. Longo, *Chem. Commun*., 5134, 2008.
74. R. Dhar, S. Kumar, M. Gupta, V.K. Agrawal, *J. Mol. Liq*., 141, 19, 2008.
75. H.K. Bisoyi, S. Kumar, *New J. Chem*., 32, 1974, 2008.
76. A.E. Murschell, T.C. Sutherland, *Langmuir*, 26, 12859, 2010.
77. K. Negita, C. Kawano, K. Moriya, *Phys. Rev. E: Stat., Nonlinear, Soft Matter Phys*., 70, 021702, 2004.
78. J. Luo, B. Zhao, J. Shao, K.A. Lim, H.S.O. Chan, C. Chi, *J. Mater. Chem*., 19, 8327, 2009.
79. M. Talarico, R. Termine, E.M. Garcia-Frutos, A. Omenat, J.L. Serrano, B. Gomez-Lor, A. Golemme, *Chem. Mater*., 20, 6589, 2008.
80. J. Kadam, C.F.J. Faul, U. Scherf, *Chem. Mater*., 16, 3867, 2004.
81. N. Boden, R.J. Bushby, K. Donovan, Q. Liu, Z. Lu, T. Kreouzis, A. Wood, *Liq. Cryst*., 28, 1739, 2001.
82. C.W. Ong, S.-C. Liao, T.H. Chang, H.-F. Hsu, *Tetrahedron Lett*., 44, 1477, 2003.
83. M. Lehmann, G. Kestemont, R.G Aspe, C. Buess-Herman, M.H.J. Koch, M.G. Debije, J. Piris, M.P. de Haas, J.M. Warman, M.D. Watson, V. Lemaur, J. Cornil, Y.H. Geerts, R. Gearba, D.A. Ivanov, *Chem. Eur. J*., 11, 3349, 2005.
84. Z. An, J. Yu, S.C. Jones, S. Barlow, S. Yoo, B. Domercq, P. Prins, L.D.A. Siebbeles, B. Kippelen, S.R. Marder, *Adv. Mater*., 17, 2580, 2005.
85. Z. An, J. Yu, B. Domercq, S.C. Jones, S. Barlow, B. Kippelen, S.R. Marder, *J. Mater. Chem*., 19, 6688, 2009.
86. C. Deibel, D. Janssen, P. Heremans, V. De Cupere, Y. Geerts, M.L. Benkhedir, G. Adriaenssens, *J. Org. Electron*., 7, 495, 2006.
87. S. Sergeyev, O. Debever, E. Pouzet, Y.H. Geerts, *J. Mater. Chem*., 17, 3002, 2007.
88. M. Kimura, H. Narikawa, K. Ohta, K. Hanabusa, H. Shirai, N. Kobayashi, *Chem. Mater*., 14, 2711, 2002.
89. C.A. Donders, S.-X. Liu, C. Loosli, L. Sanguinet, A. Neels, S. Decurtins, *Tetrahedron*, 62, 3543, 2006.
90. J. Miao, L. Zhu, *Soft Matter*, 6, 2072, 2010.
91. J.E. Kroeze, R.B.M. Koehorst, T. Savenije, *J. Adv. Funct. Mater*., 14, 992, 2004.
92. M.-H. Qi, G.-F. Liu, *J. Mater. Chem*., 13, 2479, 2003.
93. J. Hu, D. Zhang, S. Jin, S.Z.D. Cheng, F.W. Harris, *Chem. Mater*., 16, 4912, 2004.
94. S. Leng, L.H. Chan, J. Jing, J. Hu, R.M. Moustafa, R.M. Van Horn, M.J. Graham, B. Sun, M. Zhu, K.-U. Jeong, B.R. Kaafarani, W. Zhang, F.W. Harris, S.Z.D. Cheng, *Soft Matter*, 6, 100, 2010.
95. J. Wu, M.D. Watson, L. Zhang, Z. Wang, K. Mullen, *J. Am. Chem. Soc*., 126, 177, 2004.

96. E. M. García-Frutos, E. Gutierrez-Puebla, M. A. Monge, R. Ramírez, P. de Andres, A. de Andres, R. Ramírez, B. Gómez-Lor, O*rganic electronics.*,10, 643, 2009.
97. N. Blouin, M. Leclerc, *Acc. Chem. Res.,* 41,1110, 2008.
98. Y.Song, Ch.Di, Z.Wei, T.Zhao, W.Xu, Y.Liu, D.Zhang, D.Zhu, *Chem. Eur. J.,* 14, 4731, 2008.
99. N.Drolet, J.F.Morin, N.Leclerc, S.Wakim, Y.Tao, M.Leclerc, *Adv. Funct. Mater.,* 15 1671, 2005.
100. J.V.Grazulevivius, P.Strohriegl, J.Pielichowski, K.Pielichowski, *Prog. Polym. Sci.*, 28, 1997
101. Y. Wu, Y. Li, S. Gardner, B.S. Ong, *J. Am. Chem. Soc.,* 127, 614–618, 2005.

Chapter 2

MATERIALS AND METHODS

This chapter will review the materials used in this section of the dissertation and the experimental techniques used for their characterization, such as charge carrier mobility and photoconductivity.

2.1 Materials for investigating effect of different linkers

To explore the effect of the different linkers on the charge carrier mobility three compounds namely **1**, **2** and **3** were synthesized at the Instituto de Ciencia de Materiales de Madrid, Spain. The structures of the three compounds are shown in Fig. 2.1

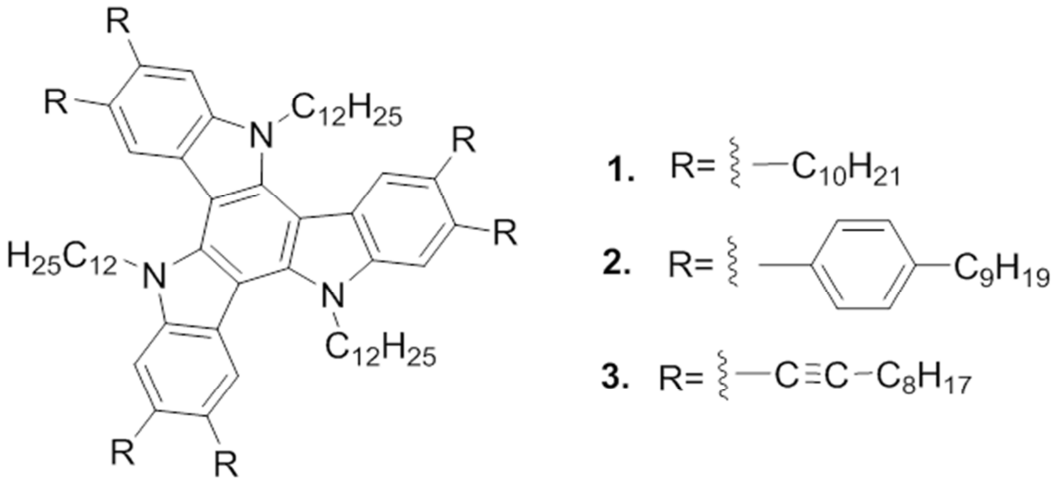

Figure 2.1: Chemical structure of compounds **1**, **2** and **3**.

In compound **1**, six decyl chains are present, whereas in compounds **2** and **3**, a sterically demanding phenyl group or a rigid alkyne group were introduce as spacers between the peripheral alkyl chains and the central triindole core. All three of the compounds exhibit a columnar hexagonal mesophase.

2.2 Materials for investigating effect of different nitrogen substituent

In order to completely understand the role of the stacking distance on the charge carrier mobility, we further decided to change the nitrogen substituent, choosing one of the linkers, that was not changed. This strategy was chosen because one might also increase the columnar ordering, simultaneously reducing the stack distance, by changing the nitrogen substituent in a discotic mesophase formed by triindole molecules. For such purpose, two new compounds, namely **4** and **5**, were synthesized and characterized at the Instituto de Ciencia de Materiales de Madrid, Spain. The structures of these compounds are shown in Fig. 2.2. In both compounds the linker and the peripheral chains are the same as in **2**, but the nitrogen substituents are -H and -CH_3 instead of -$C_{12}H_{25}$.

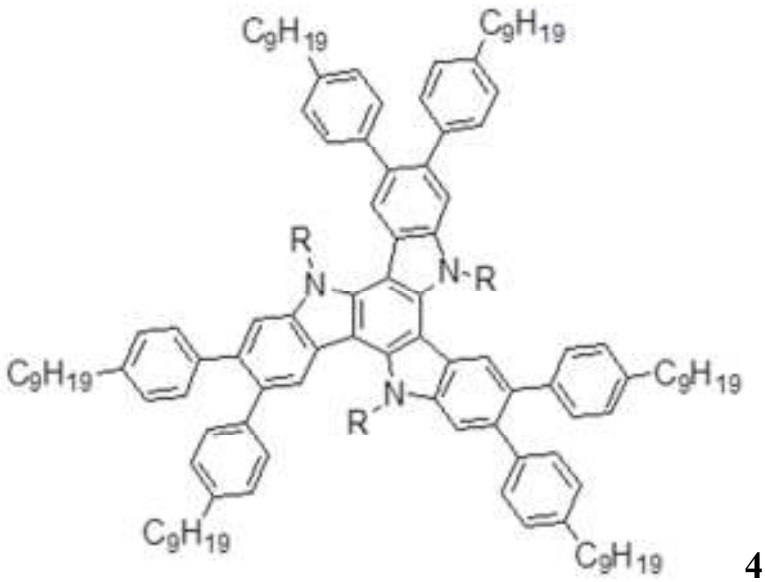

4 R = H
5 R = CH_3

Figure 2.2: Chemical structure of the compounds **4** and **5**.

Attempts to measure the charge carrier mobility of compound **6**, were also carried out. The chemical structure of the compound is shown in Fig. 2.3.

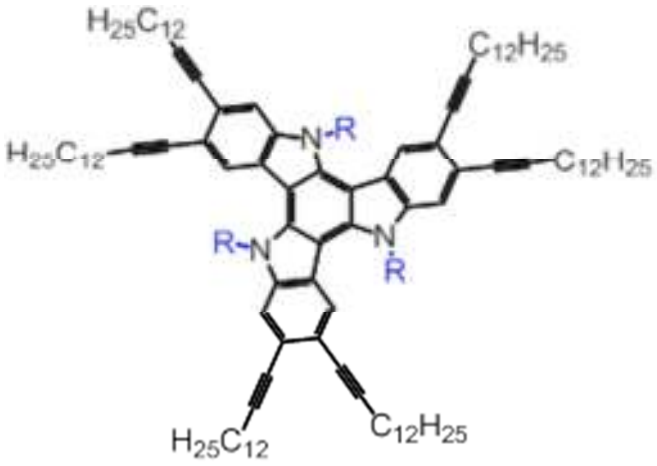

R - C_8H_{17}

Figure 2.3: Structure of compound **6**

2.3 A new columnar liquid crystal

Besides working on the charge carrier mobility of the columnar mesophases formed by the triindole cores, I also worked on a totally different kind of linear conjugated core. In the last part of the results and discussion section I will briefly explain the different optoelectronic properties of columnar liquid crystal formed by this new linearly conjugated core. These materials was synthesized at Instituto de Nanociencia de Aragón, Universidad de Zaragoza, Spain. The chemical structure of such new molecules with a linearly conjugated core is shown in Fig. 2.4. In results and discussion section I will refer **C_3B6 and C_3B9** for compound **7** and **8.**

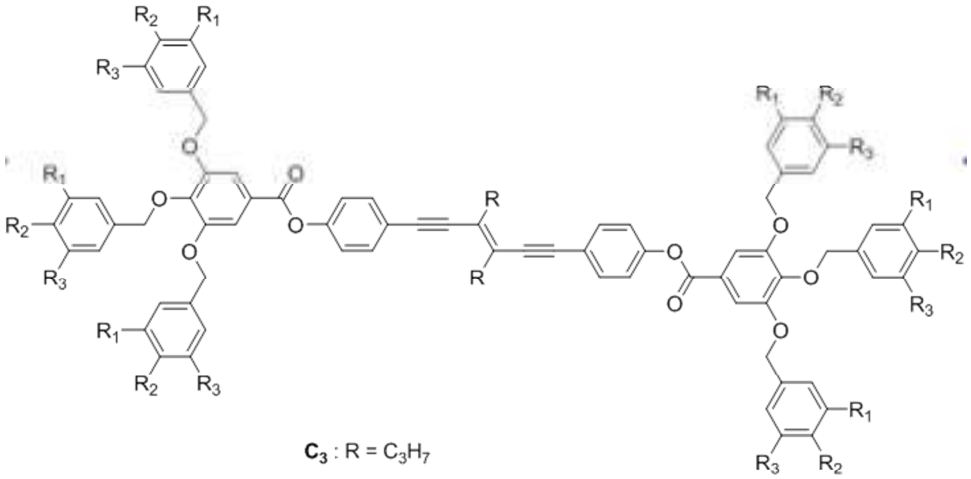

Figure 2.4: Structure of compounds **7 (C_3B6)** and **8 (C_3B9)**.

2.4 Mobility Measurements of Discotic liquid Crystals

The mobility of charge carriers in organic semiconducting materials actually determines their suitability for use in electronic and opto-electronic devices. Mobility ultimately controls the switching speed of field-effect transistors, the intensity of the light emitting diode, and the separation of charges in photovoltaic cells[1]. The mobility is strongly influenced by the properties of the solid state. In comparison to amorphous materials, highly ordered single crystalline materials[2] show higher mobility due to their well-organized structure. While staggeringly high mobilities have been reported for single crystal-devices, the major drawbacks in this approach are both the cost and the time-effort associated with the growth of single crystals.

Different techniques and device geometries have been used to measure the mobility of charge-carriers in Discotic Lliquid Crystals (DLCs) materials. These include the pulse radiolysis time-resolved microwave conductivity technique (PR-TRMC)[3-9], time-of-flight (TOF)[10-13], steady-state space charge-limited current (SCLC) [14-17], and measurements of field-effect transistor characteristics[18-20]. The limitations and advantages of the SCLC and TOF techniques, which were used for this work, will be discussed in the following.

2.4.1 Steady-state space charge-limited current (SCLC)

In steady-state SCLC experiments, charge mobility is derived from the current-voltage characteristics of thin organic films between injecting electrodes. In this method, the current-voltage characteristic is comprised of a linear region at low voltage and a nearly quadratic nonlinear region at high voltage that is referred to as the SCLC regime as shown in Fig. 2.5. While the current in linear region depends simultaneously on two unknown parameters - the volume density of free charges and the charge mobility - the current in the SCLC region depends only on the charge mobility and the dielectric properties and geometry of the sample. Hence, the measurement of the current values in this regime allows for the determination of the mobility.

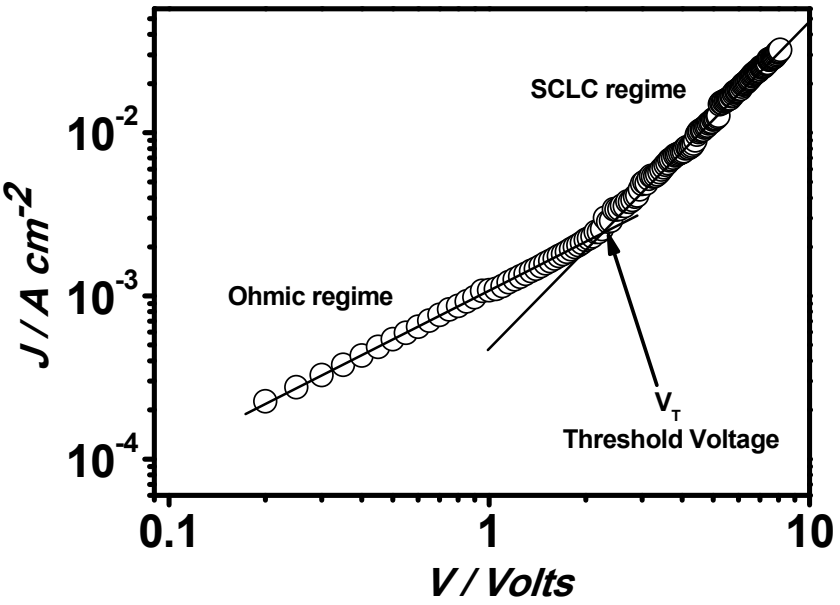

Figure 2.5: Typical current-voltage curve obtained during SCLC measurements at room temperature. The two straight lines, with slope of 1 and 2, represents ideal ohmic and SCLC behavior, respectively.

At low applied voltages, the current is a linear function of voltage and the resistive behaviour is ohmic:

$$\boldsymbol{J = n(x)e\mu E(x)} \tag{1}$$

where *J* is the current density, *n(x)* is the charge carrier density at a certain distance x, *e* is the elementary charge, μ is the charge carrier drift mobility, *E(x)* is the applied electric field. At higher voltages, the mobility calculated using SCLS is not only depends on the field due to total number of charges injected but also on the applied external field. In such cases the expression for the charge density ρ of the material is given Poisson's Eq.

$$\boldsymbol{\varepsilon \frac{\partial E}{\partial x} = \rho = n(x)e} \tag{2}$$

where ε is the dielectric constant of the material. From Eqns. (1) and (2) one can easily calculate the value of electric field at a distance x in the material which is given by:

$$\boldsymbol{E(x) = \sqrt{\frac{2Jx}{\varepsilon\mu}}} \tag{3}$$

If we want to obtain the voltage across a sample of thickness d, we integrate obtaining:

$$V = -\int_0^d E(x).dx = -\sqrt{\frac{2J}{\varepsilon\mu}}\int_0^d \sqrt{x}.dx \quad (4)$$

Performing the integral, we get:

$$V^2 = \frac{2J}{\varepsilon\mu}\left(\frac{2d^{3/2}}{3}\right)^2 = \frac{8Jd^3}{9\varepsilon\mu} \quad (5)$$

$$J = \frac{9}{8}\varepsilon\mu\frac{V^2}{d^3} \quad (6)$$

After rearranging the above Eq. (6) we will finally get the expression of current density in terms of the voltage given by the Eq. (7).

$$J = \frac{9}{8}\varepsilon_r\varepsilon_0\mu\frac{V^2}{d^3} \quad (7)$$

The above equation is broadly known as the Mott-Gurney equation. That's why, in the SCLC regime, at higher voltage the current can be approximated by the above Eq. (7). In the above Eq. (7), ε_0 is the free space permittivity and ε_r is the relative dielectric constant of the material.

According to Eqn. (1) and (7), the voltage V_T at which the slope of the I – V curves changes from linear to quadratic can be given by.

$$V_T = \frac{8}{9}en\frac{d^2}{\varepsilon_r\varepsilon_0} \quad (8)$$

The measured value of the mobility can be used in Eq. (1) to obtain n which, in turn, can be used in Eq. (8) to obtain V_T. A reliability check of the mobility measured by SCLC technique can be carried out by comparing the theoretically calculated and experimentally measured V_T values: a good match indicates a reliable measurement.

From Eq. (7), it is evident that in order to calculate the mobility, one has to know the value of the relative dielectric constant ε_r of the material. We used LCR meter (Instrument name & type) to measure the capacitance of each sample. The capacitance is given by Eq. (9).

$$C = \varepsilon_r\varepsilon_0\frac{S}{d} \quad (9)$$

In the Eq. (9) $\varepsilon_0 = 8.854 \times 10^{-12}$ F/m is the vacuum permittivity, S is the area of the sample and d is the thickness of the sample. From the above Eq. (9) one can easily calculate the value of ε_r.

An important condition in the analysis of this method is that the contact from where the charges are to be injected must be ohmic. One limitation of the SCLC technique is that both holes and electrons can be injected from the appropriate electrodes and contribute to the SCLC current. For a nearly perfect ohmic contact the difference in the energy of the contact and the material should be ≤ 0.3eV.

The relative contribution of hole and electron conductivities can be controlled by a careful choice of metal electrode work functions. For hole mobility measurements, metals should be selected such that their work function matches the energy of the highest occupied molecular orbital (HOMO) of the organic semiconductor, whereas for determining electron mobilities the lowest unoccupied molecular orbital (LUMO) energy should be matched. The SCLC measurements were finally performed on these samples using a either Keithley 6517A or Keithley 2400 source meter to obtain current-voltage characteristics.

2.4.2 Time-of-flight (TOF)

The time-of-flight technique relies on charge photogeneration. Charges are generated by light irradiation of films in a typical sandwich-cell configuration, as shown in Fig. 2.6. A light pulse with a defined wavelength, depending upon the peak absorption of the material under test, and with a short duration (typically of the order of μs or less) is delivered to the sample, so that the absorption and the following charge generation occurs in a very thin layer of material close to the first interface. An electric field is applied to induce a drift of the charges. Depending on the polarity of the applied field, holes or electrons will move across the sample, thus inducing a transient current, which is recorded in an external circuit with the help of an oscilloscope, allowing the determination of the type of charge carriers involved. It is important to note that the value of the resistance in series with the sample must be much lower than the internal resistance of the sample itself.

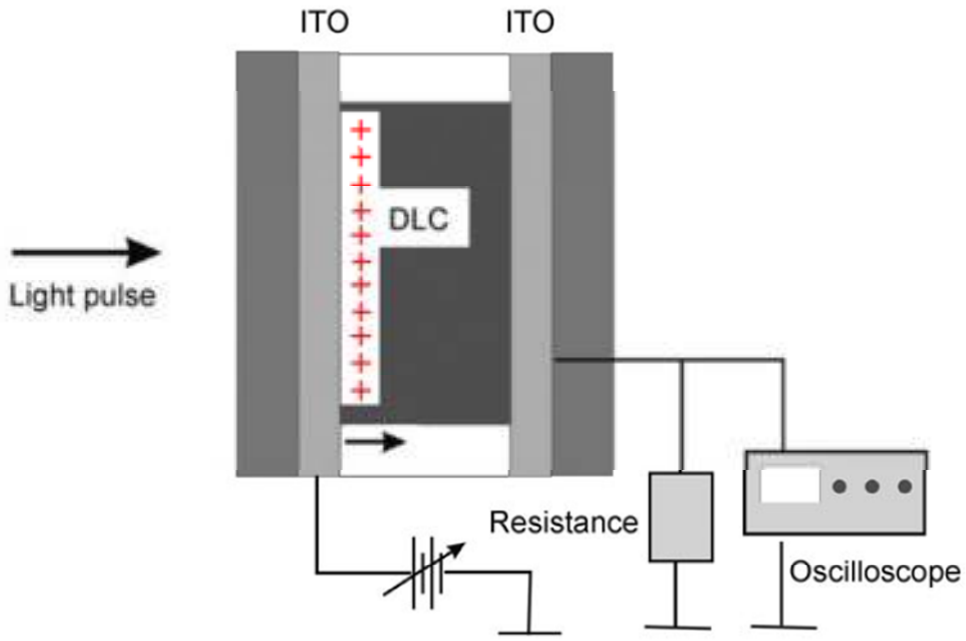

Figure 2.6. Schematic of the setup of the TOF experiment.

The time that charges take to travel between the electrodes allows the mobility μ to be estimated. In fact, μ depends on the applied voltage V and transit time t_t according to Eq. (10), where v is the drift velocity, d is the film thickness, and E is the applied electric field.

$$\boldsymbol{\mu = \frac{v}{E} = \frac{d^2}{Vt_t}} \tag{10}$$

If the photogeneration process is not efficient enough, a thin layer of a photosensitizer can be deposited between the conducting material and the electrode. In this case charges photogenerated in the photosensitive layer are injected into the material. In Fig. 2.7a typical transient current development is shown: when a sheet of charges is first photogenerated/injected in the sample, a sharp increase in the transient current is observed. Then the transient current is constant (Fig. 2.7b) until the injected charges reache the opposite electrode and at $t = t_t$, before the current decays (Fig. 2.7c).

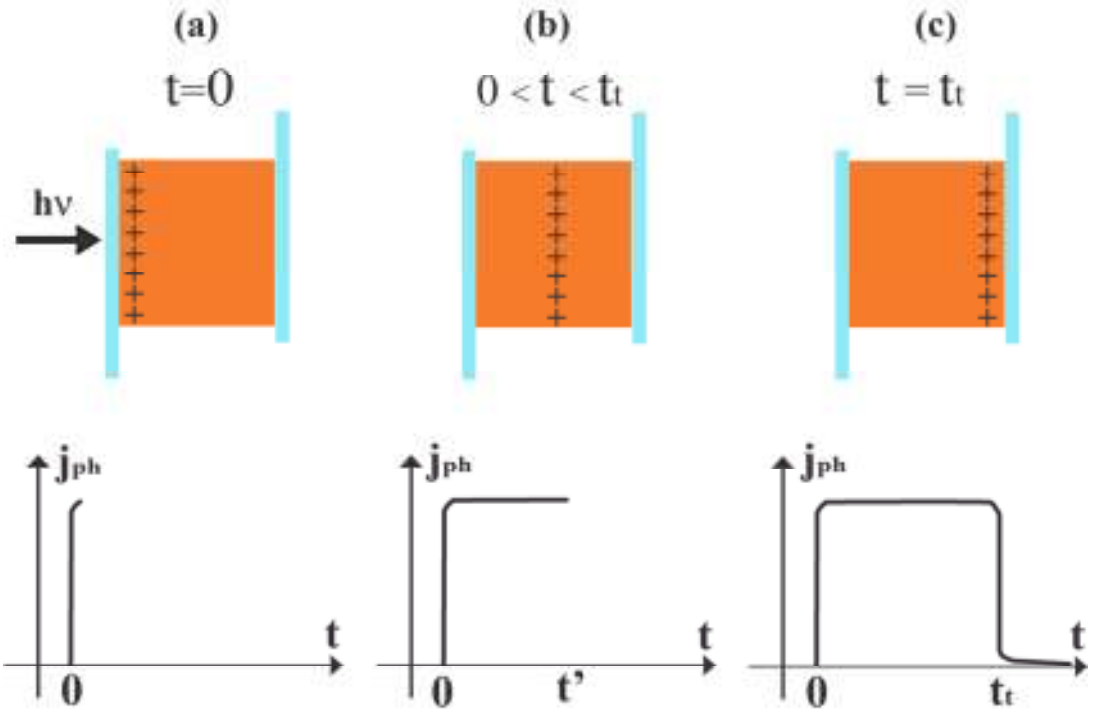

Figure 2.7. Transient current during a TOF experiment

The behaviour shown in Fig. 2.7 is typical for an ideal material. However, not many materials show this ideal case of a transient photocurrent and the behaviour shown in Fig. 2.8 is often observed.

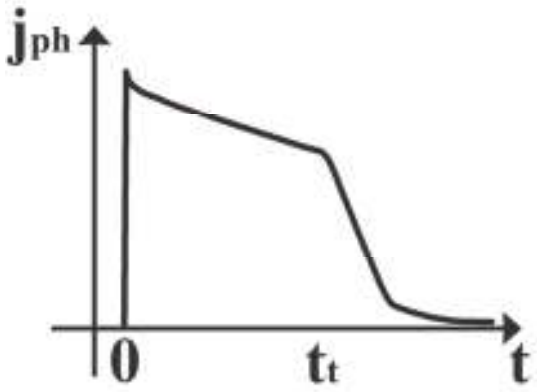

Figure 2.8. Typical current transient shape during a TOF experiment on a non-ideal material.

This behaviour can have many causes. Some of them are connected with: (a) the RC response time of the circuit, (b) the loss of carriers due to deep trapping, (c) the variation in drift mobility of the sheet of charge carrier as a function of its position due to sample inhomogeneity, (d) the local electric-field variation due to trapped space charge

and (e) the spreading of the sheet of charge carriers on a distance comparable to the thickness of the sample.

The reason (a) is usually responsible for a practical limitation of the transient experiment, as given by the condition $RC << \tau << \tau_d$, where τ_d is a deep trapping lifetime, R is the resistance and C is the capacitance of the sample. A current induced across R due to the drifting carriers across the sample in the presence of the applied potential will fall rapidly as the carriers arrive at the counter electrode at the transit time (τ). So the response time RC of the circuit must be always less than τ.

Sometimes, if the trace is too dispersive, it is very difficult to locate the transit time. In such traces, logarithmic scales are used in both axes to find the transit time. The transient time is then determined by the intersection of the two lines with different slopes in the transient photocurrent, as shown in Fig. 2.9.

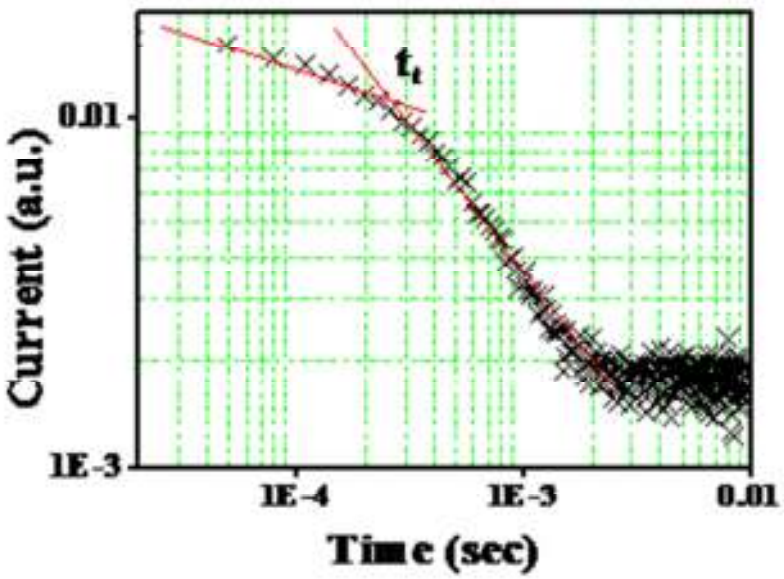

Figure 2.9. Log-log plot in a dispersive transient current obtained in a typical TOF experiment.

There are some limitations in this technique. The dielectric breakdown at high field limits the application of high voltage. The disturbance due to noise limits the experiment at a low field, when little charge is generated. The internal field may also be disturbed by the injected charge. A contact between the sample and the electrode may cause electrochemical reactions resulting in contamination and reduction of the quality of

the sample. It is also difficult to change the alignment of molecules in-situ because the sample is sandwiched between two electrodes. It is not possible to degas in-situ, i.e., the gas trapped between electrodes at the time of filling the cell cannot be removed. When the first electrode is negative, a rapidly decaying current is often observed, due to the electrons being absorbed by residual oxygen trapped within the electrodes[21], making it difficult to measure electron mobility.

2.5 Photoconductivity Measurements

Photoconductivity (σ_{photo}) measurements can be performed by measuring the difference between the electric conductivity under illumination and the electric conductivity in the dark. In organic materials, the measurement is conducted by applying an electric field and then measuring the electrical conductivity increase resulting from sample illumination. The schematic of the set-up for the photoconductivity measurement is shown in Fig. 2.10.

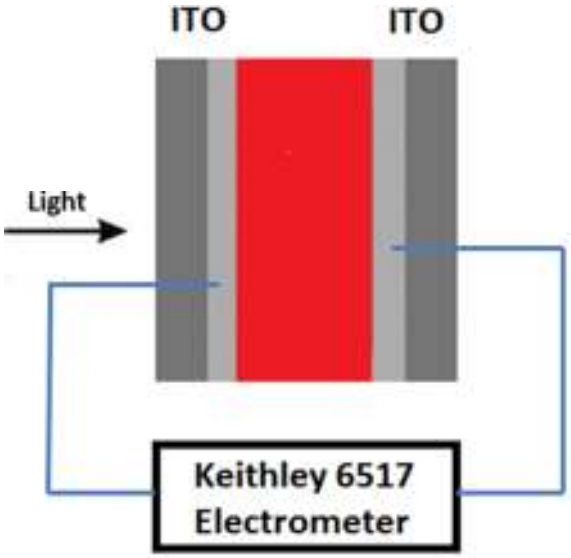

Figure 2.10. Schematic of Photoconductivity measurement set-up.

In our photoconductivity experiments, a certain electric field is applied across the sample using a Keithley 6517 electrometer (can measure currents up to pico-ampere with great precision) depending upon the sample thickness and material properties. The corresponding currents were measured under dark and illumination. During the experiment, it is necessary to first let the dark current stabilize at a certain applied field. If the material is photoconducting, upon illumination photogenerated charges are created

and they move to the other electrode under the influence of the applied electric field, resulting in a current. A typical current during the photoconductivity measurement is shown in Fig. 2.11.

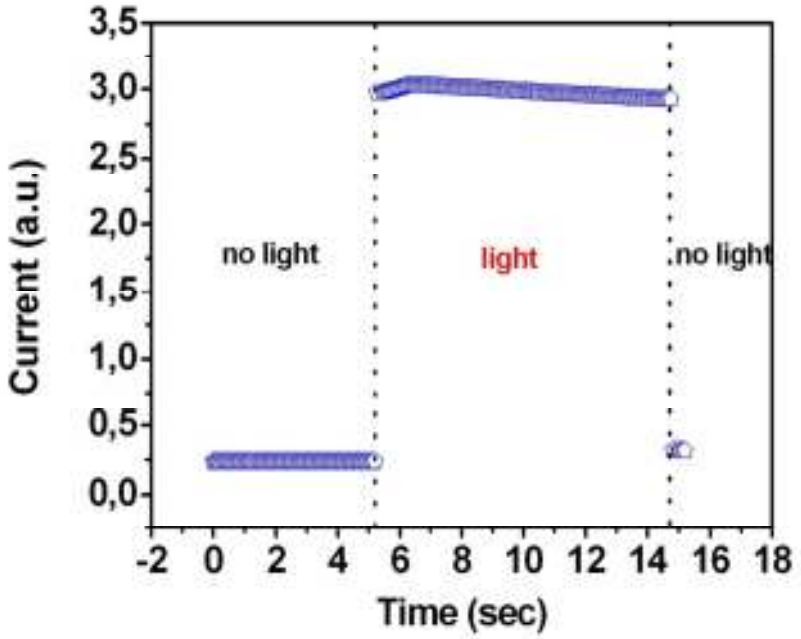

Figure 2.11. Typical current of a photoconducting material under dark and illumination during the measurement.

The photoconductivity can be calculated by using Eq. (11).

$$\boldsymbol{\sigma_{photo}} = \frac{\boldsymbol{I_{light}.d}}{\boldsymbol{V.S}} \tag{11}$$

Where, I_{light} is the current difference between with and without illumination, V is the applied voltage across the sample, d is the thickness of the sample and S is the area of the sample under illumination. Since photogeneration efficiency depends on the intensity of light (I), results are often expressed in terms of σ_{photo}/I . A typical σ_{photo}/I versus applied electric field curve is shown in Fig. 2.12.

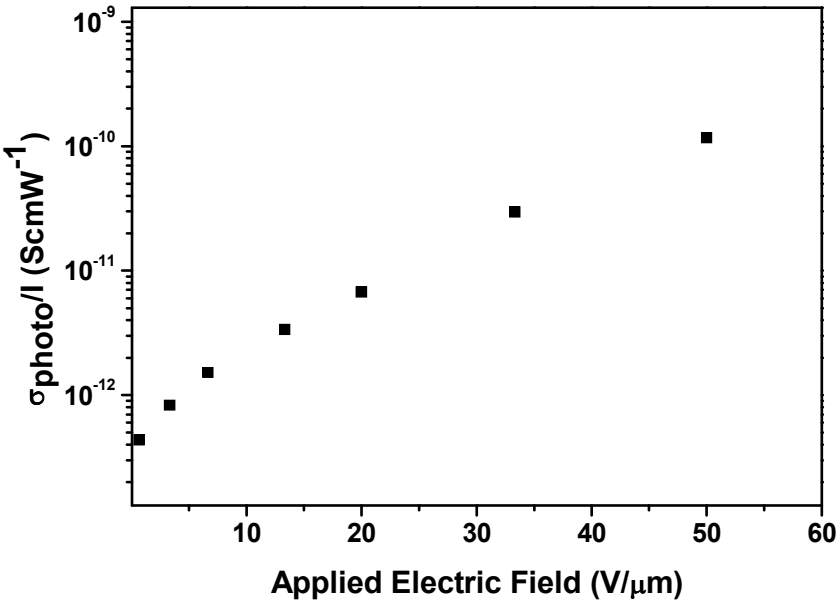

Figure 2.12. Typical σ_{photo}/I Vs applied electric field curve of photoconducting material.

The applied electric field and light wavelength are important factors determining the continuous wave (C) photoconductivity of the material. In general, if the illuminated light wavelength is the same where the material shows maximum absorption, the resulting photogenerated current will be higher due to higher number of photogenerated charges. The electric field dependence of the C photoconductivity (I_c) can be characterize by a power law function, $I^c \propto (E)^{\alpha_c}$, with α_c ranges between 1.8 – 3.2 for organic films[22, 23].

2.6 Measurement of the thickness of the samples.

The thickness of the empty cell can be measured by using a UV-Vis spectrophotometer. Light passes through the inner walls of the sample placed perpendicular to incident beam of the spectrophotometer, see Fig. 2.13a. As a result of interference, one typically obtains an interference pattern consisting of maxima and minima, as shown in Fig. 2.13b. Note that if the inner walls of the cell are not nearly parallel, one will not get very clear interference patterns. From this graph, we can easily calculate the thickness of the cell using Eq. (11).

$$\boldsymbol{d = \frac{x\lambda_1\lambda_2}{2n(\lambda_1-\lambda_2)}} \qquad (11)$$

Where d is the thickness of the cell, n is the refractive index of air (n ~ 1), x is the total number of oscillation maxima between the wavelength maxima λ_1 and λ_2 as shown in Fig . 2.13b.

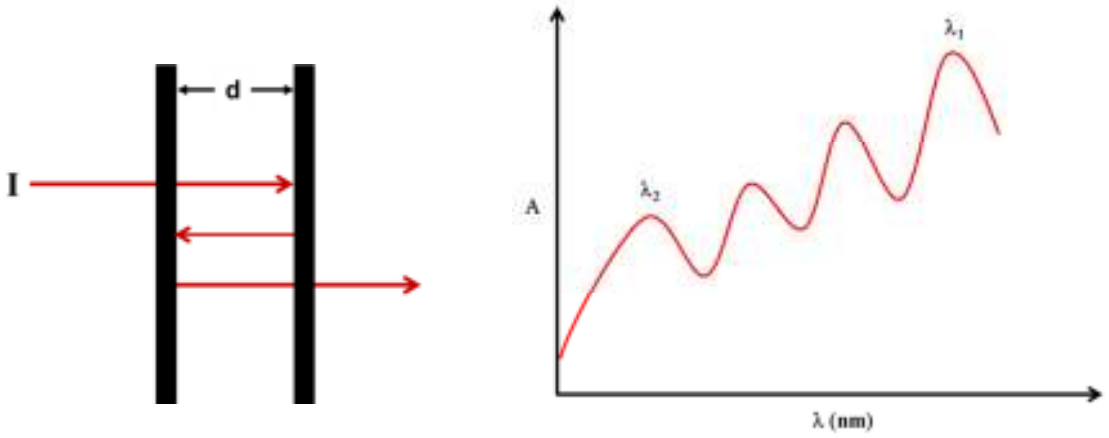

(a) **(b)**

Figure 2.13. (a) Internal reflection in a cell of thickness d and (b) related interference pattern obtained from spectrophotometer.

To obtain the interference pattern for the thickness calculation of the cells the wavelength of the spectrophotometer was varied from 900 nm to 1500 nm.

2.7 Sample preparation

Cells for SCLC measurements were usually prepared by using two glass slides with two different conducting surfaces. One type of electrode was obtained by etching, by photolithography, indium tin oxide (ITO) coated glass (UNAXIS, 110 nm ITO thickness) in order to obtain 1 mm wide strips. The other type of electrode was of gold stripes prepared by thermal evaporation in high vacuum (10^{-7} mbar) .

Before preparing the devices, ITO electrodes were cleaned in a ultrasonic bath via successive treatments with detergent, distilled water, acetone and isopropanol and then dried overnight at 80°C in a vacuum oven. The shape of the ITO stripes and gold stripes are shown in Fig. 2.14.

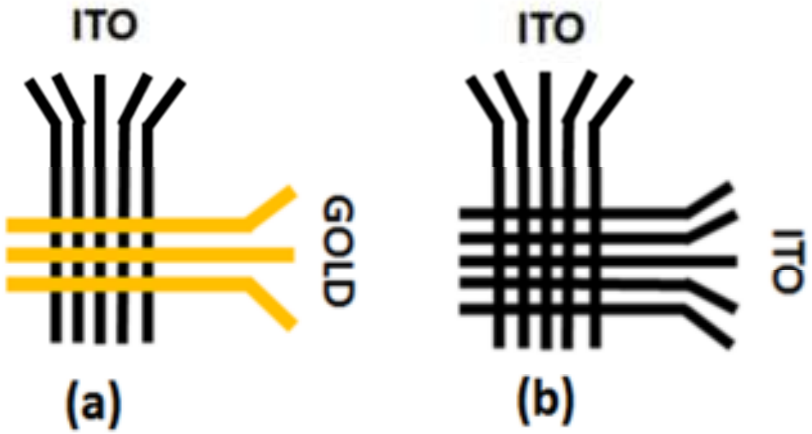

Figure 2.14. Schematic of the samples prepared for drift mobility measurements.

The two substrates were glued together, using spacers of different thicknesses, ranging from 1.7 μm to 5 μm, to control the thickness of the sample, which was subsequently measured by interferometry. Cells were then filled by capillarity, by melting the material on a hot plate, often inside a glove box (H_2O < 0.1 PPM, O_2 < 0.1 PPM) under nitrogen or argon atmosphere. Samples were then allowed to cool down to room temperature by simply turning off the hot plate.

When the material decomposes before melting, we cannot use capillarity to fill preformed cells. In such cases, we usually heated the material on one of the two electrodes at 15 °C or more below the decomposition point and then we squeezed the

other electrode on top of it. In this method the thickness was measured after sample preparation. However, we could not use Au electrodes because gold does not stick well on glass and the Au electrode would be damaged during the squeezing. We instead prepared samples by using two ITO electrodes. In this case, for the proper matching of the work functions between sample and electrode, in order to insure efficient injection of the charge carriers, air plasma treatment was performed on one of the ITO electrodes. Plasma treatment is widely used to tune the work function of ITO. The resulting devices were sealed by using an epoxy glue prior to be transferred outside the glove box for further measurements.

BIBLIOGRAPHY

1. J.M. Warman, M.P. de Haas, M.P. Dicker, G. Grozema, F.C. Piris, M.G. Debije, *Chem. Mater.,* 16, 4600, 2004.
2. V.C. Sundar, V. Zaumseil, V. Podzorov, E. Menard, R.L. Willet, T. Someya, E. Gershenson, J.A. Rogers, *Science.*, 303, 1644, 2004.
3. Y. Wu, Y. Li, S. Gardner, B.S. Ong, *J. Am. Chem. Soc.,* 127, 614, 2005.
4. G. Dicker, M.P. de Haas, L.D.A. Siebbeles, J.M. Warman, *Phys. Rev. B: Condens. Matter Mater. Phys.,* 70, 045203/1, 2004.
5. F.C. Grozema, T.J. Savenije, M.J.W. Vermeulen, L.D.A. Siebbeles, J.M. Warman, A. Meisel, D. Neher, H.G. Nothofer, U. Scherf, *Adv. Mater.,* 13, 1627, 2001.
6. J.M. Warman, A.M. van de Craats, *Mol. Cryst. Liq. Cryst.,* 396, 41, 2003.
7. A.M. van de Craats, J.M. Warman, *Adv. Mater.,* 13, 130, 2001.
8. K. Ban, K. Nishizawa, K. Ohta, A. M.van de Craats, J.M. Warman, I. Yamamoto, H. Shirai, *J. Mater. Chem.,* 11, 321, 2001.
9. M.G. Debije, J. Piris, M.P. De Haas, J.M. Warman, Z. Tomovic, C.D. Simpson, M.D. Watson, K. Müllen, *J. Am. Chem. Soc.,* 126, 4641, 2004.
10. J.M. Warman, J. Piris, W. Pisula, M. Kastler, D. Wasserfallen, K. Mullen, *J. Am. Chem. Soc.,* 127, 14257, 2005.
11. D. Adam, P. Schuhmacher, J. Simmerer, L. Haeussling, K. Siemensmeyer, K.H. Etzbach, H. Ringsdorf, D. Haarer, *Nature,* 371, 141, 1994.
12. P.M. Borsenberger, E.H. Magin, M. van der Auweraer, F.C. de Schryver, *Phys. Status Solidi A,* 140, 9, 1993.
13. D. Poplavskyy, J. Nelson, *J. Appl. Phys.,* 93, 341, 2003.
14. A. Rybak, J. Pfleger, J. Jung, M. Pavlik, I. Glowacki, J. Ulanski, Z. Tomovic, K. Mullen, Y. Geerts, *Synth. Met.,* 156, 302, 2006.
15. P.W.M. Blom, M.J.M. de Jong, M.G. van Munster, *Phys. Rev. B: Condens. Matter.,* 55, R656, 1997.
16. L. Bozano, S.A. Carter, J.C. Scott, G.G. Malliaras, P. Brock, *J. Appl. Phys. Lett.*, 74, 1132, 1999.
17. Y. Shen, M.W. Klein, D.B. Jacobs, J. Campbell Scott, G.G.Malliaras, *Phys. Rev. Lett.*, 86, 3867, 2001.
18. V.D. Mihailetchi, J.K.J. van Duren, P.W.M. Blom, J.C. Hummelen, R.A.J. Janssen, J.M. Kroon, M.T. Rispens, W.J.H. Verhees, M.M. Wienk, *Adv. Funct. Mater.*, 13, 43, 2003.
19. A. Babel, S.A. Jenekhe, *J. Am. Chem. Soc.,* 125, 13656, 2003.
20. V. Podzorov, S.E. Sysoev, E. Loginova, V.M. Pudalov, M.E. Gershenson, *Appl. Phys. Lett.,* 83, 3504, 2003.
21. K. Oikawa, H. Monobe, J. Takahashi, K. Tsuchiya, B. Heinrich, D. Guillonc, Y. Shimizu, *Chem. Commun.,* 5337, 2005.
22. B.R. Kaafarani, L.A. Lucas, B. Wex, G.E. Jabbour, *Tetrahedron Lett.*, 48, 5995, 2007.
23. J. Day, S. Subramanian, J.E. Anthony, Z. Lu, R.J. Twieg, O. Ostroverkhova, *J. Appl., Phys.,* 103, 123715, 2008.

Chapter 3

MOBILITY IN COLUMNAR MESOPHASES

In this chapter the structural and thermal properties and the results of charge carrier mobility measurements of **1 - 6** will be discussed. The steady state space charge limited current (SCLC) method was used to obtain charge mobility values. Both the effect of different linkers between core and peripheral chains and the effect of the nitrogen substituent on mobility will be discussed. Also, the optoelectronic properties of a similar discotic liquid crystal formed by a totally different new linearly conjugated core will be discussed.

3.1 Effect of linkers on the charge carrier mobility

Charge carrier mobility measurements were carried out on compounds **1 - 3**. The structures of the compounds are shown in Fig. 3.1

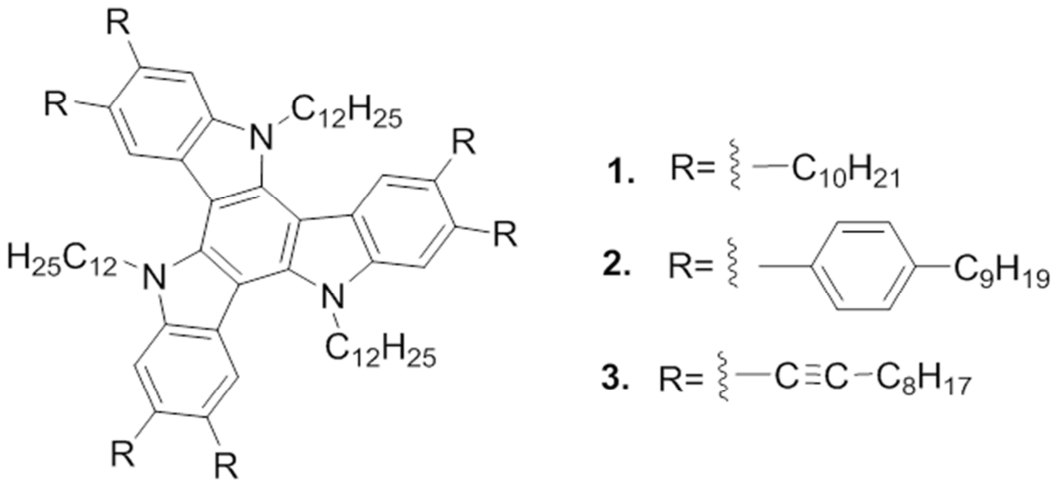

Figure 3.1: Chemical structure of the compounds **1**, **2** and **3**.

3.1.1 Structural Characterization

Compounds **1 - 3** were synthesized at the Instituto de Ciencia de Materiales de Madrid, Spain. The structural and thermal characterizations were also performed at the same place and I will summaraize here the main results. The X-ray diffraction data of the

mesophases of **1** – **3**, along with the Differential Scanning Calorimetric (DSC) results and the HOMO level, obtained from cyclic voltammetry, are summarized in table 3.1

Compound	Thermal properties[a]	Stacking distance (Å)	HOMO (eV)
1	C 38.9 (51.2) Col_h 67.3 (0.5) I	-	4.94
2	C 39.3 (39.7) Col_{ho} 153-160 I	4.4	4.98
3	C 43.5 (51.2) Col_{ho} 150-165 I	3.9	5.05

[a] Corresponding to the first heating scan (DSC), C: crystal, Col_h: hexagonal columnar mesophase, Col_{ho}: ordered hexagonal columnar mesophase.

Table 3.1: Phase transition temperatures (^{0}C) and corresponding enthalpy values (in brackets, KJ/mol), of **1** - **3**, intracolumnar distance of the hexagonal columnar mesophase determined by XRD.

Among the compounds listed in table 3.1, **2** and **3** were obtained as crystalline solids. On heating, they show mesomorphic behavior between *ca* room temperature and *ca* 150 ºC, a significant broader range when compared with compound **1** (Table 1). In particular, distancing the disordered alkylic chains from the central core with phenyl (compound **2**) or alkyne linkers (compound **3**), does not significantly influence the melting points but drastically increases the clearing point of these materials. Both **2** and **3** exhibit a hysteresis phenomenon in the crystallization process upon cooling, showing a glassy state that maintains the structural features of the mesophases. This behavior favors the structural characterization of the compounds at room temperature. Only partial crystallization is observed after several days.

The mesophases of **2** and **3** were identified as ordered hexagonal columnar (Col_{ho}), on the basis of the typical pseudoconical textures observed by POM as shown in Fig. 3.2 which was in accordance with their X-ray diffractograms (Table 3.1).

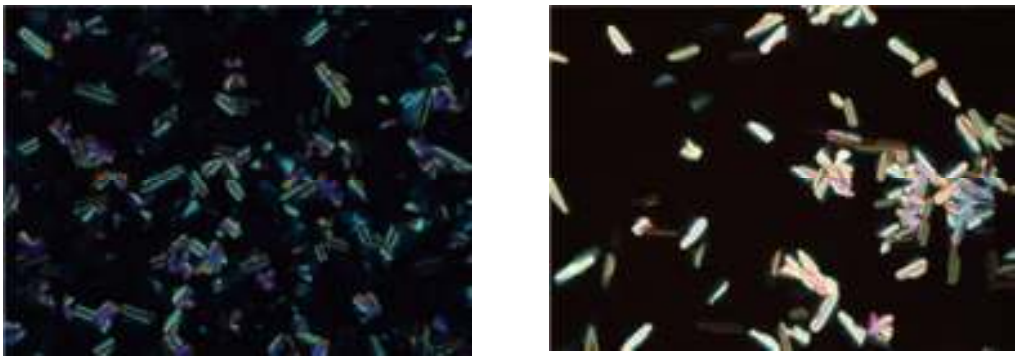

Figure 3.2: Polarizing optical photomicrographs of **2** (left) and **3** (right) obtained at 105 ºC and 117 ºC, respectively, on cooling from the isotropic liquid.

The X-ray diffraction patterns obtained for these compounds show a diffuse halo at 4.5 Å, typical of the liquid-like order of the aliphatic chains. The diffraction patterns of **2** and **3**, in contrast to what observed for compound **1**, present an additional diffuse maximum with intensity reinforcement in the meridian region. This maximum corresponds to the periodic stacking of the cores, evidencing the higher order achieved by distancing the disordered alkylic chains from the central core.

Bulky phenyl linkers have been previously shown to efficiently interlock molecules within the columns.[1] However, in the case of **2**, the high steric demand of these connecting groups induces large stacking periodicities (c = 4.4 Å). The alternative strategy of distancing the alkylic chains from the central core by rigid ethynyl groups results instead in closer adjacent disks (c = 3.9 Å) for **3** (Table 1). It should be noted that while phenyl[1] or phenylethynyl moieties[2,3] have often been used as linkers between the flexible chains and the aromatic core, the direct attachment of the pendant side chains through an alkyne spacer has been rarely described.[4,5]

3.1.2 Charge carrier mobility measurements

In order to measure the charge carrier mobility of compounds **1** - **3**, SCLC measurements were performed. Cells of various thicknesses, ranging between 4 and 10 μm, were prepared, using gold and ITO as electrodes. The gold electrode was chosen in order to obtain ohmic contact for the SCLC measurements. The measured values of mobility were highly dependent on the alignment of each particular sample, and even on the alignment of different areas within the same sample. The values of charge carrier

mobility measured for compounds **1** - **3** along with the intracolumnar stacking distance are summarized in table 3.2

Typical SCLC characteristic curves for compound **2** are shown Fig.3.3. The mobility of compound 2 was measured on the as prepared sample as well as the aligned samples. We were able to align properly this sample by using controlled thermal treatment. For the compound 2 the mobility reported in the table 3.2 is of that on the aligned sample. Alignment is very important, as in this case mobility values decreased even by more than one order of magnitude when the alignment was particularly poor.

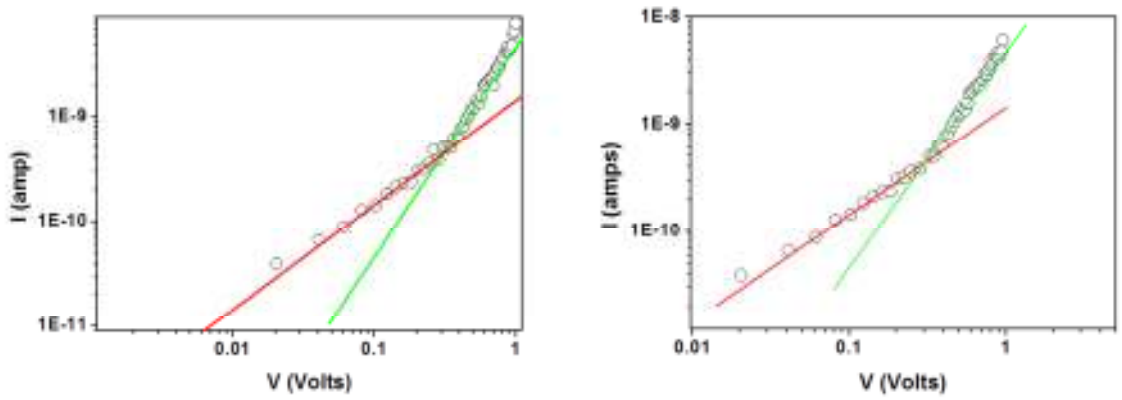

(a) (b)

Figure 3.3: Typical SCLC curves obtain during mobility measurement of compound **2**.

SCLC measurements of compound **3**, were performed on as prepared and partially aligned samples. For this compound the alignment we could obtain after controlled thermal treatment was not particularly as good as compared to compound **2**, but still we were able to get good SCLC curves and values. The typical SCLC curves obtained during the measurement of compound **3** is shown in Fig. 3.4 In both the compounds **2** and **3**, SCLC measurement by changing the polarity of the applied electric field , the current obtained was more than half a magnitude less and there was not any quadratic behaviour found. As I discussed earlier that, mobility measurement using SCLC technique is highly dependent on the alignment of the sample. For example for this compound we prepared two samples of thicknesses 6 and 5.2 µm respectively, for SCLC measurements. In both the cases alignment was tried to obtain the best results for the mobility values. In the case of first sample we obtain the average mobility value of 0.14

$cm^2V^{-1}s^{-1}$ where as for the second one the average mobility value was observed 1.4 $cm^2V^{-1}s^{-1}$.

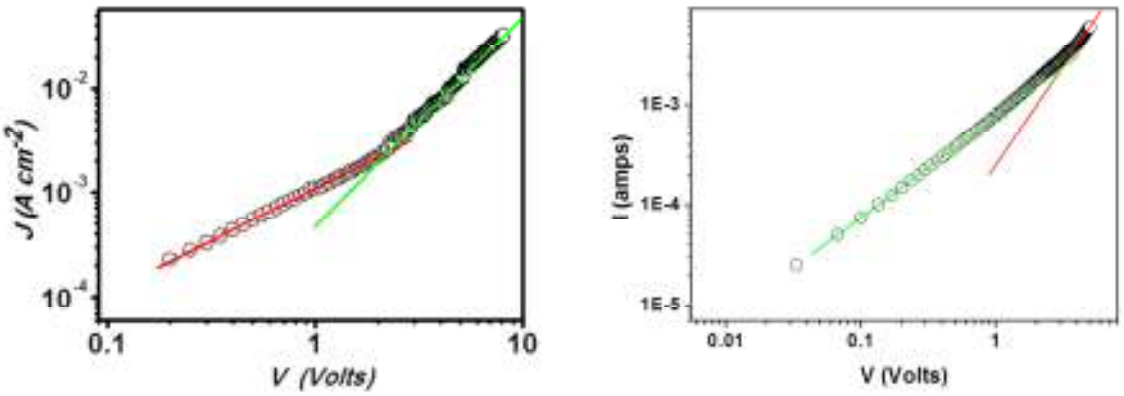

(a) **(b)**

Figure 3.4: Typical SCLC curves obtain during mobility measurement of compound 3.

The different values of mobility obtained between different samples, can be attributed to the fact that the material present different morphologies in the two sample. In particular the second sample observed under the microscope showed a better alignment. The microscopic images of the sample after alignment in both cases are shown in Fig. 3.5.

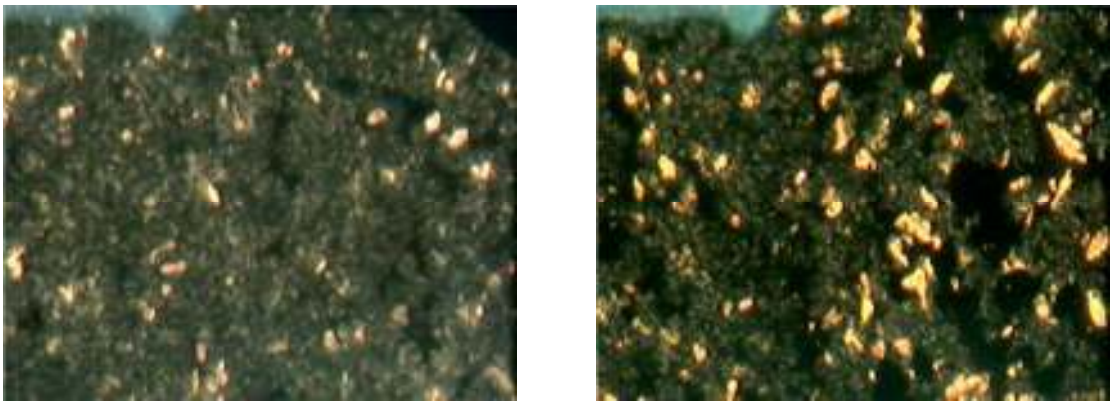

Sample 2 **Sample 3**

Figure 3.5: Comparison of microscopic images of compound 3 for two different samples at 10X magnification.

In Table 3.2, we summarize the mobility values measured in the samples with the best alignment which, as mentioned above, was good for **1** and **2**, but only partial for **3**.

Compound	Stacking distance (Å)	Mobility (μ) ($cm^2 V^{-1}s^{-1}$)
1	-	0.02 ± 0.005
2	4.4	$6x10^{-4}$ ± 0.0004
3	3.9	1.4 ± 0.3

Table 3.2 Stacking distance (in Å) in of the hexagonal columnar mesophase compounds **1**, **2** and **3**, determined by XRD and charge carrier mobility (μ) determined from SCLC measurements.

As the SCLC technique is sensitive not only to orientational order defects but also to the charge injection effectiveness at the electrodes, this should be considered as a lower limit for the hole mobility. To our knowledge, the hole mobility of **3** is the highest ever reported for discotic phases.[6] This results is particularly relevant since the columnar phases with the highest hole mobility generally exhibit shorter stacking distances (around 3.4 Å) and considerably more extended π-systems. In addition, from what is known on similar model compounds,[7] the core of **1-3** is expected to be to some extent non-planar, a condition that is known to hinder orbital overlap and then mobility. However, examples of columnar phases with high mobility obtained from mesogens with non-planar cores are known[8].

Compound **3** simultaneously shows a more regular stacking order (compared to **1**) and a shorter stacking distance (compared to **2,** as evident from the XRD data shown in table 3.1). The comparison between the charge carrier mobility of **1** and **3** shows that the value found for **1** (a liquid crystalline material with no constant stacking distance) is two orders of magnitude lower than the mobility of **3**, probably due to this lack of intracolumnar order. On the other hand, compound **2**, with a high degree of

intermolecular order but with a larger intermolecular regular distance, shows the lowest charge mobility, underlining the importance of the stacking distance.

The role of ethynyl linkers is then twofold: increasing the order within the column and at the same time reducing the stacking distances. However, the possible contributions to the charge transport of a larger π-orbital overlap and/or of a variation of the relative orientation of adjacent molecules induced by the alkyne spacers, could also be important.

In conclusion, the strategy of introducing alkyne spacers has proved to efficiently increase the supramolecular order in the discotic mesophases, simultaneously reducing the distance between molecules in the stack, resulting in the discotic liquid crystalline material with the highest hole mobility reported to date. This concept is illustrated graphically in Fig 3.6. The stacking order and distance in columnar phases of triindole-based liquid crystals is controlled by the linker (orange in the figure) between the central triindole core (green) and the peripheral flexible chains of a discotic mesogen.

Figure 3.6: Schematic representation of the effect of the linkers on the stacking distance and on the charge carrier mobility in the columnar mesophases formed by mesogens with a triindole core.

3.2 Effect of different nitrogen substituents

Charge carrier mobility measurements were also carried out on compounds **4** and **5.** The structure of the compounds **4** and **5** are shown in Fig. 3.7.

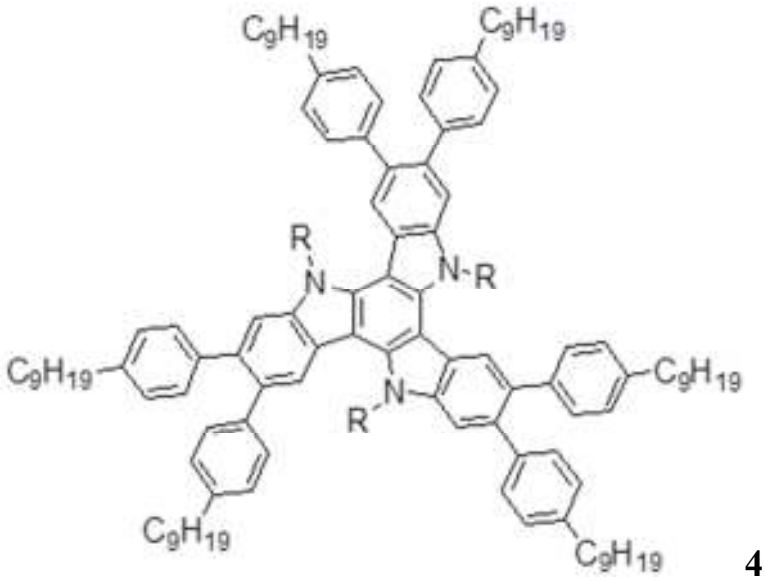

4 R = H
5 R = CH_3
2 R = $C_{12}H_{25}$

Figure 3.7: Chemical structure of the compounds **2**, **4** and **5**.

3.2.1 Structural Characterization

Phase Transition Temperatures (ºC), with the corresponding Enthalpy Values (in brackets, KJ/mol)**,** lattice constant (in Å) in of the hexagonal columnar mesophase determined by XRD and HOMO values obtained from CV for compounds **4** and **5** are summarised in Table 3.3.

Both compounds were obtained as waxy solids and they show mesomorphism when heated over a wide range of temperatures. By polarized optical microscopy (POM) typical textures were not observed for these mesophases, neither was the transition to isotropic liquid. Upon cooling, fluidity gradually decreases but neither POM nor DSC gave any evidence of crystallization or glass transition.

Compound	Thermal properties[a]	Stacking distamnce (Å)	HOMO (eV)
2	C 39.3 (39.7) Col_{ho} 153-160 I	4.4	4.98
4	Col_{ho} 140 Desc.	3.3	4.98
5	C(Col_h) 90.1 (1.8) Col_{ho} 175 Desc	3.5	5.05

[a] Corresponding to the first heating scan (DSC), C: crystal, Col_h: hexagonal columnar mesophase, Col_{ho}: ordered hexagonal columnar mesophase.

Table 3.3: X-ray diffraction data for the mesophases of **4** and **5**, along with the Differential Scanning Calorimetric (DSC) and the CV results .

The X-ray diffraction patterns of **4** and **5** show a set of maxima at low angles, that unequivocally assign the mesophases as hexagonal columnar. A maximum at high angles corresponding to the periodic staking of the cores was also observed. These maxima are relatively sharp and this gives evidence of a long range correlation order within the columns. The structural details of the compound **2** is described in the previous section. The presence of a small N-substituent allows a more efficient π-π stacking comparing distances with derivatives incorporating N-octyl and N-dodecyl alkylic chains.

For compound **5**, the XRD patterns show an additional diffuse maximum at middle angles corresponding to twice the stacking distance (3.5Åx2), and this is consistent to a certain local order within the column. Taking into account the single crystal XRD data of an analogue methyl-substituted triindole, it is possible to propose a model in which one molecule is rotated 60º with respect to the next molecular unit. The C3 symmetry of the triindole causes an interaction between the aromatic rings of one molecule and its nearest neighbor which are located on top of each other. This periodicity is not observed in **4** and this can be explained by the absence of the methyl groups that obligate molecules to rotate to better accommodate them.

3.2.2 Charge carrier mobility measurements

Charge carrier (hole) mobility of **4** and **5** was measured by steady-state space charge limited current (SCLC) technique. As these substance decompose before melting, for this set of experiments cells of various thicknesses ranging from 9 to12 μm were prepared using ITO for both electrodes. A plasma treatment was performed on one of the ITO electrodes to tune the work function of the ITO, in order to achieve a good ohmic contact (details can be found in the materials and methods section).

As it was the case with the measurements described above, mobility depends highly on the alignment of the sample. While a good alignment was obtained for **2**, with **4** and **5** **a**ttempts to align the director by thermal treatment (holding the sample on a controlled hot plate 15 °C below the decomposition temperature for 15 min, followed by a slow cooling at 0.3 ^{0}C/min) were not helpful and the values of mobility before and after the treatment were the same, within experimental error. The lack of a good alignment was also evident from the microscopic images, before and after the thermal treatment. Examples of microscopic images of **4** and **5** after thermal treatment at different resolutions are shown in Fig. 3.8.

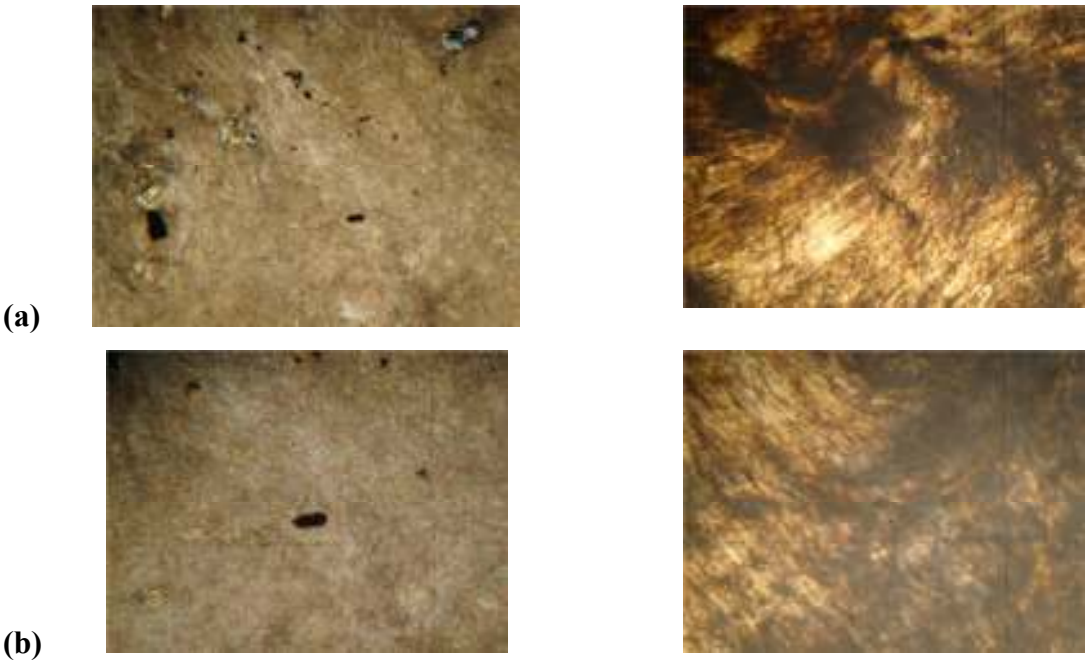

(c)

(4) **(5)**

Figure 3.8: Microscopic images of **4** and **5** at (a) 5X (b) 10X and (c) 50X magnification.

Examples of typical SCLC behaviour of **4** and **5** are shown in Fig. 3.9 All experiments were carried out with the plasma treated ITO as the positive electrode. By changing the polarity of the applied electric field, the measured currents decreased by more than half a magnitude order and no quadratic regime was obtained. The theoretical and experimental threshold voltage values for the onset of the SCLC regime closely matched, with a maximum mismatch of 3%. This is a good evidence that the measured mobility values are reliable. As the SCLC technique is sensitive not only to orientational order defects but also to the charge injection effectiveness at the electrodes, this should be considered as a lower limit for the hole mobility of **4** and **5**.

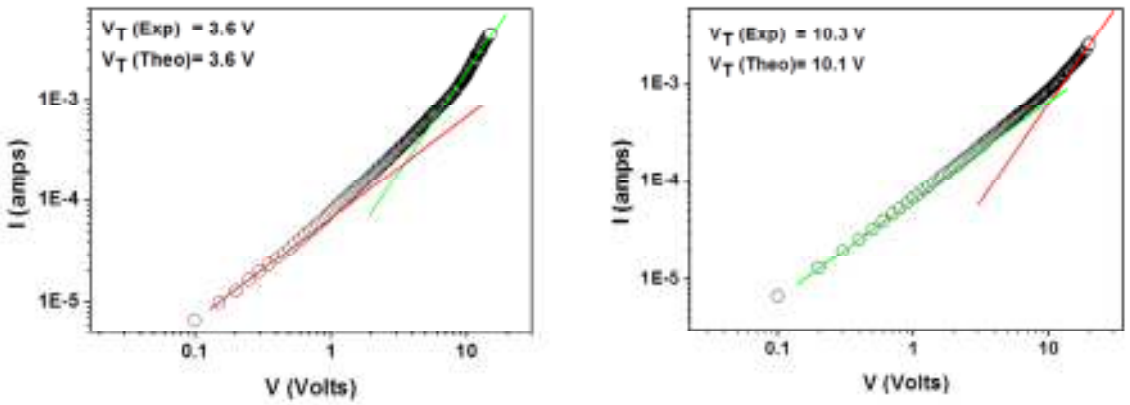

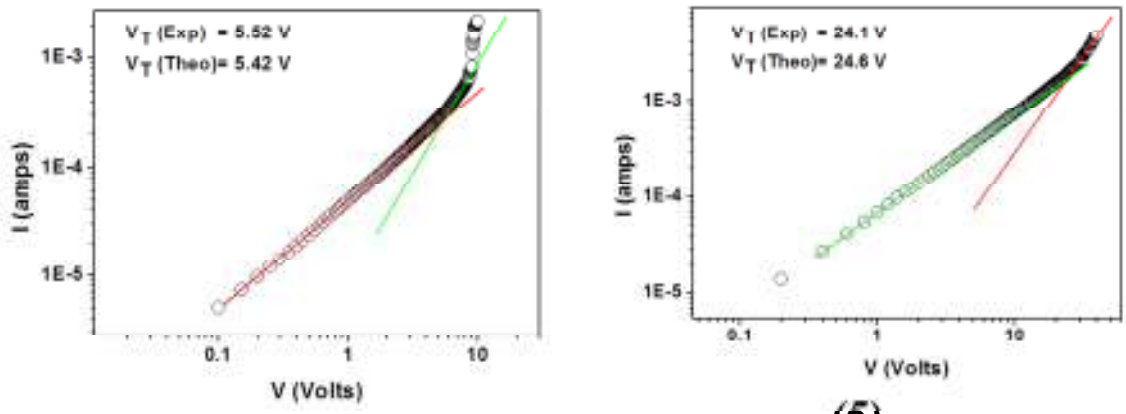

Figure 3.9: Typical characteristic curves for **4** and **5**.

Results of the charge carrier mobility values of **2**, **4** and **5** along, obtained from the above I/V characteristivs of SCLC with the stacking distance in the column are summarized in Table 3.4. All measurements were performed at room temperature.

Compound	Stacking distance (Å)	Mobility (μ) ($cm^2 V^{-1}s^{-1}$)
2	4.4	$6x10^{-4} \pm 0.0004$
4	3.3	2.4 ± 1.3
5	3.5	2.8 ± 1.6

Table 3.4: Mobility values of compound **4** and **5** along with the stacking distance.

It is important to underline that the waxy nature of **4** and **5** is at the same time positive and negative. Its negative nature is connected to the fact that the director is not easily orientable, as explained above. The positive side is that the materials can be easily processable from solution, forming films with homogeneous thickness and without pinholes. Mobility measurements on the thin films of these compounds are in progress.

Considering all the results in compounds **1**-**5** we can conclude that the obtained values of hole mobility are the highest ever measured in columnar mesophases. This result is particularly relevant, given the fact that the extent of π-conjugation is low, and often also the stacking distance is far from ideal, highlighting the importance of triindole as a core for high mobility columnar phases. We have also shown that even though higher order has been often claimed as a fundamental factor for improving mobility in discotic liquid crystals, at least in this particular case the stacking distance between molecules seems to be even more important. These results can be of general relevance for many columnar phases, as they point out the specific role of chain-linkers and nitrogen substituents[9] in determining stacking distances. The recognition of such an important structure-function relationship can certainly guide future work aimed at obtaining columnar phases with high charge mobility.

Compound **6**, with the same alkynyl linker as in **3**, was also tested. The only difference in their structure is in the nitrogen substituents: – C_8H_{17} for **6** and – $C_{12}H_{25}$ for **3**. The structure of **6** is shown in Fig. 3.10

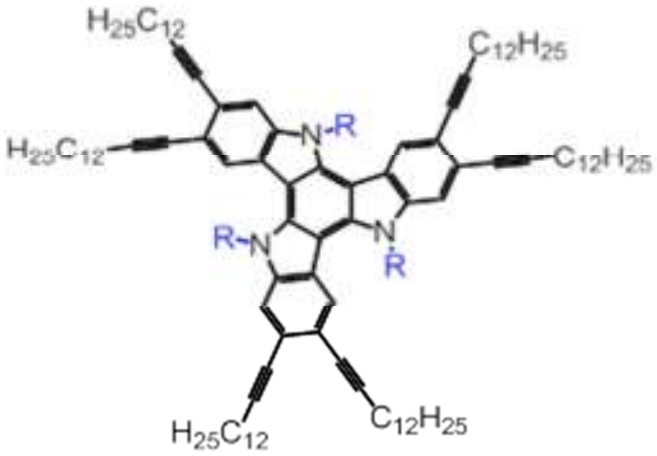

R - C_8H_{17}

Figure 3.10.: Structure of compound 6

X-ray diffraction (XRD) studies were performed to identify the mesophases and the results are summarized in Table 3.5.

Compound	Thermal properties[a]	Stacking distance (Å)	HOMO (eV)
6	Col_{ho} 143^{0}C I	3.9	4.90

[a] Corresponding to the first heating scan (DSC), Col_{ho}: ordered hexagonal columnar mesophase.

Table 3.5: X-ray diffraction data in the mesophase of **6**, along with the Differential Scanning Calorimetric (DSC) and CV results.

The mesophases compound **6** was identified as ordered hexagonal columnar (Col-$_{ho}$), on the basis of X-ray results and of the typical pseudoconical textures observed by POM, as shown in Fig. 3.11. This compound is columnar at room temperature and it was easy to align.

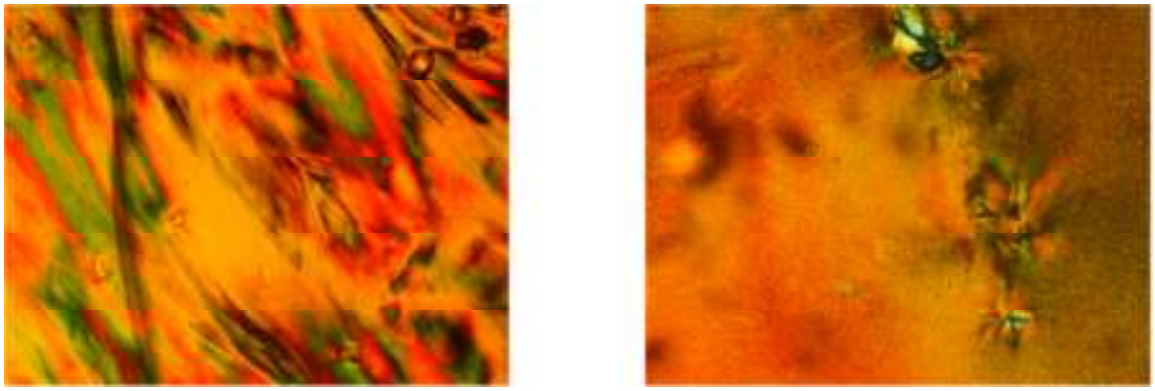

(a) (b)

Figure 3.11. POM images of compound **6**. (a) Heating at 65 ^{0}C, (b) cooling after flattening at 72 ^{0}C

Repetitive attempts to measure the charge carrier mobility of **6** by using the SCLC technique were not successful. The J-V characteristic were always linear, never reaching a quadratic regime. This could be possible due to two reasons, (a) the samples prepared for SCLC measuerments were shorted or not evenly (air bubble) filled, leading to the linear behavior of the measurements and (b) a very high charge mobility of compound 6 could also lead to the linear behaviour during SCLC measurements. This happens when the mobility of the charges generated are too high and due to this they are collected at the

counter electrode before showing any quadratic behaviour. This reason can not be ruled out as the similar coupound 3 shows a very high charge carrier mobility.

3.3 A Linear Conjugated Core for Multifunctional Columnar Liquid Crystals

The design of multifunctional materials is one of the most interesting targets in materials chemistry. The combination of different physical properties in the same material may simplify the processing required to construct the corresponding devices and this aspect is of great importance in fields such as organic optoelectronics[10-14]. In an effort to achieve optoelectronic materials, a great deal of research effort has been focused on the supramolecular organization of the molecules[15-17]. The appropriate organization of the different functional building blocks in such a way that one or several properties are magnified, or the appearance of cooperative effects in the material due to the influence of the neighboring molecules, are ideal situations that must be considered for the development of high-performance functional materials.

In this respect, the combination of liquid crystalline order with other physical properties is particularly interesting to obtain multifunctional materials in which the control of the macroscopic molecular arrangement is essential for a certain property to manifest itself or to be enhanced, especially those properties that are direction-dependent[18-21]. Liquid crystals allow us to control order at the microscopic level and this can be extended into the macroscopic regime through appropriate processing and bulk alignment. Thus, for example, the effects of π-conjugation and organization on emission and conductive properties have led to an increasing interest for columnar liquid crystals as an approach to luminescent and semiconductor materials for optoelectronic applications[22-24]. Indeed, columnar phases of tailor-made mesogenic cores have been synthesized and investigated with regard to their application as semiconductors with high charge-carrier mobility values and intense fluorescence[25-32].

The molecular design of columnar liquid crystals not only relies on disk-like structures. Phasmidic or polycatenar liquid crystals are a family of thermotropic mesogens that are generally composed of a rod-like core and two half-disk-shaped units (aromatic end groups containing several flexible tails) [33]. These mesogenic structures combine the structural and mesogenic properties of conventional calamitic and discotic

liquid crystals. As a result, polycatenar liquid crystals not only display conventional nematic and smectic mesophases, but they also commonly display columnar mesomorphism in which the composition of the stacking units is strongly dependent on the particular structure of the molecule. Furthermore, this approach allows tailoring of the mesogen design toward the achievement of functional liquid crystals with luminescent and photoconducting properties suitable for optoelectronic purposes[34-36].

In this section I will show the results of emission, X-ray characteristics briefly which was done at Instituto de Nanociencia de Aragón, Universidad de Zaragoza, Spain and finally the photoconductivity of the two compounds named C_3B6 and C_3B9.

C_3B9 is a new polycatenar mesogen derived from a new core, 1,6-diphenyl-3,4-dipropyl-3-hexen-1,5-diyne (**C_3**), basically a π-conjugated core reported by our collaborators[37]. This core has a rod-like shape, high electronic conjugation and fluorescence properties in solution, which make it interesting to implement functionality into liquid crystalline materials. This C3 core has been modified in the two terminal positions with aromatic acid bearing long aliphatic chains and acids **B**, derived from 3,4,5-tribenzyloxybenzoic acid. These carboxylate moieties contribute to the design of molecules with structurally differentiated parts, which promote liquid crystalline order through nanosegregation. Moreover, the properties encoded in the molecule, i.e. chirality or electronic and luminescent features, are transferred to the resulting mesomorphic organization and hence manifested by the final material.

The structure of the compound is shown in Fig. 3.12

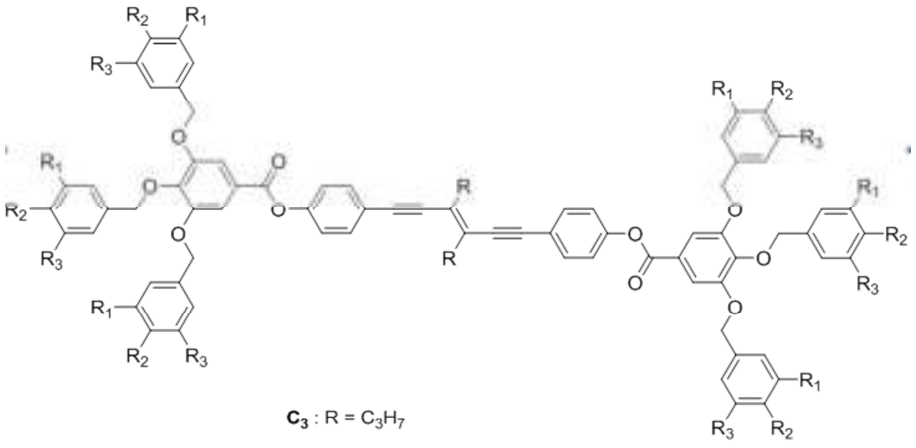

Figure 3.12: Chemical structure of compounds C_3B6 and C_3B9.

3.3.1 Thermal properties

The thermal behavior of the **C_3B6** and **C_3B9** mesogens was characterized by polarizing optical microscopy (POM) and differential scanning calorimetry (DSC). Phase transition temperatures and associated enthalpy values of both compound are summarized in Table 3.6.

Compound	Transition[a] temperatures, ºC and [enthalpies, kJ mol^{-1}][b]								
C_3B6	M	8.1[c] [30.6]					Col_h	107.0 [29.7]	I
C_3B9			Col_h	40.3 [–84.2]	Cr	84.6 [149.8]	{Col_h	59.6}[e] [13.6]	I

(a) Cr: crystalline phase, M: unidentified mesophase, Col_h: hexagonal columnar mesophase, I: isotropic liquid. (b) Reported are the onset values of transitions observed in the second heating-cooling cycle at 10 ºCmin^{-1}, except for (c), for which the maximum of the peak is given. (. (e) Monotropic transition.

Table 3.6: Phase transition temperatures and associated enthalpy values for **C_3B6** and **C_3B9** .

From data summarized in Table 3.6, it can be deduced that an optimum size-ratio between the bis-dendronized rigid π-conjugated core and the aliphatic regions (π-stacking and flexibility, respectively) exists, and this ensures stable mesomorphic properties through nanosegregation. This is the case for compounds **C_3B6**. Compounds derived from acid **B6** show Col_h behavior at room temperature. In addition, at temperatures below 8 ºC, **C_3B6** show a mesophase that could not be identified.

Compound bearing the acid **B9**, **C_3B9** show monotropic mesomorphic behavior. The Col_h mesophase of **C_3B9** was previously characterized[37], although its data are herein included for the better comparison with **C_3B6**.

3.3.2 Structural characterization of the mesophases

X-ray diffraction was performed on **C_3B6** and **C_3B9** with the aim of elucidating the type of mesophase and determining the lattice parameters. Most of the experiments were performed at room temperature; however, in some cases high-temperature experiments

were also carried out. The proposed indexing, lattice constants, and the observed and calculated maximum diffraction distances of the columnar mesophases are summarized in Table 3.7

.compound	T(ºC)	phase	lattice constant (Å)
C_3B6	RT	Col_h	a = 54.1
	79	Col_h	a = 52.9
C_3B9	RT	Col_h	a = 33.9

Table 3.7: X-ray diffraction data for the columnar mesophases of compounds **C_3B6** and **C_3B9**

From X-ray pattern, together with POM observations, it was concluded that there are two molecules per unit cell for C3B6 in one coloumn. A hexagonal lattice of C3B6 consists one column per unit cell and this was interpreted as two molecules forming each slice of the column. However, for C3B9 there was half a molecule per unit cell which corresponds to half a molecule per columnar stratum was observed. The lattice parameter is much smaller than the parameters of the Col_h mesophase found for compounds derived from acid **B6,** and this finding supports both models, this proposed for **C_3B6** , with Z=2 and the one proposed for **C_3B9** with Z=0.5 (Figure 3.13a,b).

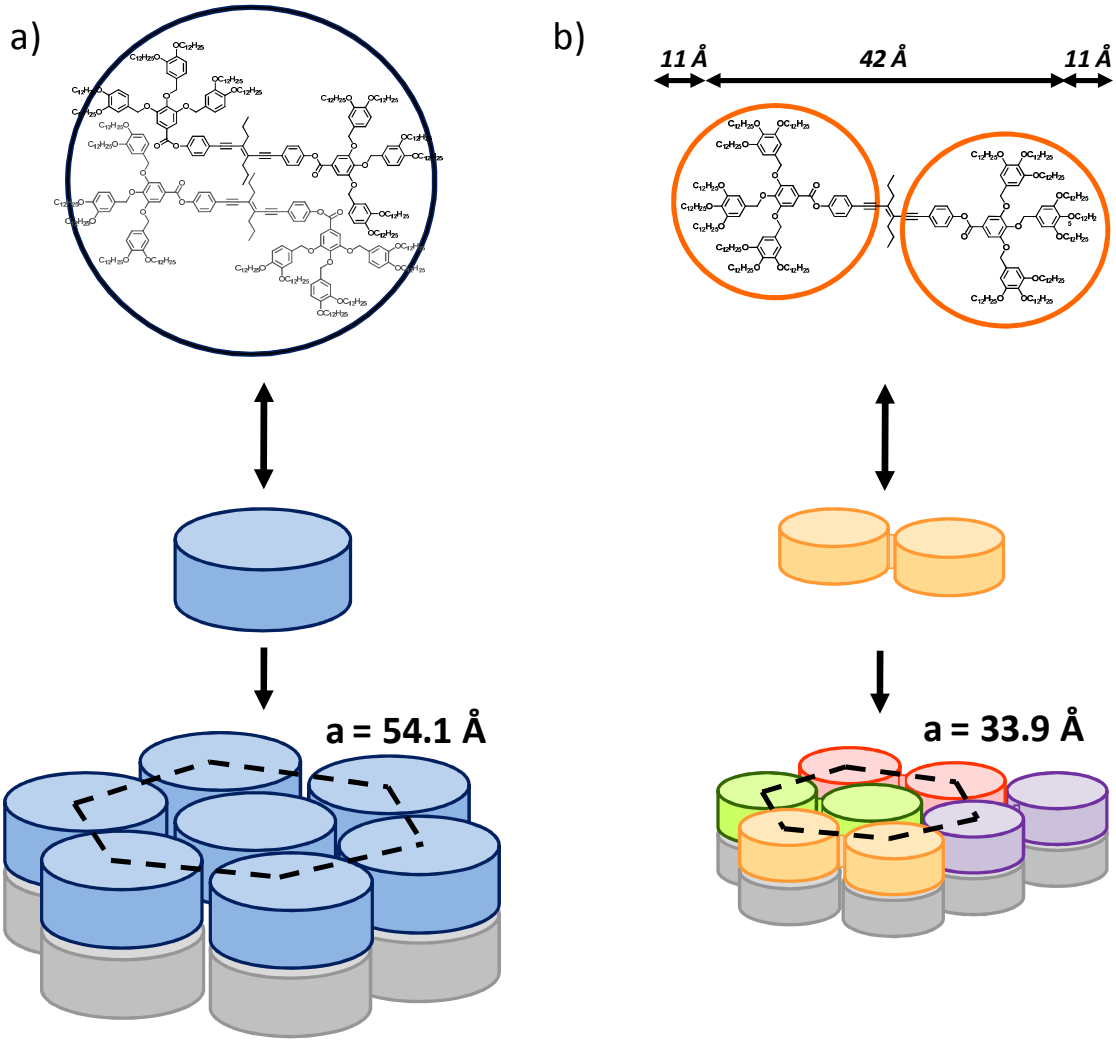

Figure 3.13: Proposed models for the disposition of a) two molecules per slice of the column in the columnar mesomorphic arrangement of compound **C_3B6**, and b) half a molecule per slice of the column in the columnar mesomorphic arrangement of compound **C_3B9**. The size measured by stereomodels for the molecule is represented in b). The length of the aliphatic part has been estimated considering an all-trans conformation for the chains (11Å).

3.3.3 Luminescent properties

The luminescent properties of both compounds (C3B6 and C3B9) were investigated by absorption and emission spectroscopy in solution and, where applicable, in the mesophase. Both C3B6 and C3B9 show the same absorption and emission profiles,

3.3.4 Electroactive Properties

In view of the potential applications in optoelectronics of molecules C_3B6 and C_3B9, it is important to consider the relative facility to inject holes and electrons, respectively, in the material. This can be approximated from the molecular electrochemical properties, first oxidation and first reduction potentials, measured in solution and associated with the highest occupied and the lowest unoccupied molecular orbitals (HOMO and LUMO energy levels, respectively). The electrochemical behavior of **C_3B6** and **C_3B9** was investigated by cyclic voltammetry (CV), in oxygen-free THF solutions. The corresponding HOMO and LUMO energy levels are summarized in Table 3.8.

Compound	HOMO (eV)[c]	LUMO (eV)[d]
C_3B6	-5.7	-2.4
C_3B9	-5.8	-2.5

Table 3.8: HOMO and LUMO levels of **C_3B6** and **C_3B9** in THF solutions.

The charge carrier mobility of **C_3B6** and **C_3B9** were very difficult to measure, as their HOMO level is too low to ensure a good ohmic contact with any electrode, which is a requirement for SCLC measurements. For this reason it was decided to measure room temperature photoconductivity. Such measurements were performed as a function of wavelength and electric field, on samples that were aligned as homeotropic monodomains or, at least, partially aligned. Photoconductivity shows the usual electric field dependence (as shown in Figure 3.14) As expected, the photoconductivity of both **C_3B6** and **C_3B9** increases with increasing absorption but even at λ = 532 nm, where absorption is quite small, a photoconduction signal can be measured. The values of photoconductivity are similar to the ones measured in amorphous materials, i.e. in this case the columnar organization does not seem to improve mobility.

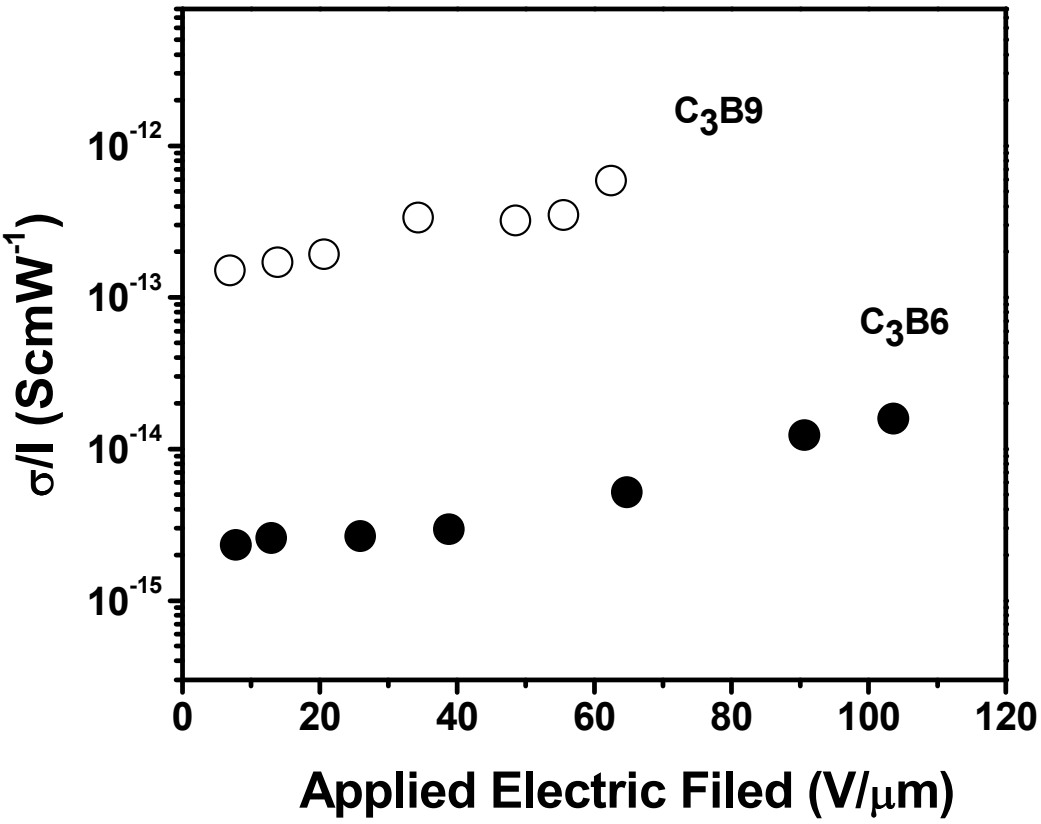

Figure 3.14: Photoconductivity of **C_3B6** (homeotropically aligned, 4.0 μm thick sample; α = 80 cm^{-1}) and **C_3B9** (partially aligned, 7.5 μm thick sample; α = 75 cm^{-1}) as a function of the applied electric field, at λ = 532 nm.

In conclusion of this section, the self-organization characteristics of rod-like fluorophore **C_3** can be controlled by conjugation to different types of benzoic acid derivatives. This strategy allows multifunctional materials to be obtained that combine mesomorphic architectures with luminescence and photoconducting properties.

Depending on the type of acid, the nature of the materials ranges from nematic liquid crystals, for compounds derived from 4-dodecyloxybenzoic acid, to columnar liquid crystals, for compounds that incorporate six or nine terminal tails, through crystalline solids, for compounds with either four or six terminal tails. Indeed, the size ratio between the rigid core and the acid groups, which vary in bulk, is crucial to address

self-organization, thus indicating the delicate balance of forces involved in liquid crystalline behavior. Also, the structure of the Col_h mesophase shown by compound **C_3B9** with half a molecule as the circular cross section of column is corroborated, versus the structure of the column in **C_3B6** in which two columns form the stacking unit.

As multifunctional materials, C3B6 and C3B9 compounds show luminescence in the mesophase and this indicates that the supramolecular architecture prevents quenching – in contrast to the situation in the crystal structure of the chromophores. These columnar materials behave as photoconductors. Our materials show a photoconductivity which is of the same order of magnitude as the photoconductivity of the amorphous polymers[38] often used as photoconductors, but much lower than in crystalline composite organic solids[39].

.

BIBLIOGRAPHY

1. I. Fischbach, T. Pakula, P. Minkin, A. Fechtenkötter, K. Müllen, H. W. Spiess, K. J. Saalwachter, *Phys. Chem. B,* 6408, 2002.
2. S. Diring, F. Camerel, B. Donnio, T. Dintzer, S. Toffanin, R. Capelli, M. Muccini, R. Ziessel, *J. Am. Chem. Soc.*, 131, 18177, 2009.
3. G. Hennrich, E. Cavero, J. Barberá, B. Gómez-Lor, R.E. Hanes, M. Talarico, A. Golemme, J. L. Serrano, *Chem. Mater.,* 19, 6068, 2007.
4. B. Kohne, K. Praefcke, *Chimia*, 41, 196, 1987.
5. K. Praefcke, B. Kohne, *Angew. Chem. Int. Ed. Engl,* 29, 177, 1990.
6. M. van de Craats, J. M. Warman, A. Fechtenkötter, J. D. Brand, M. A. Harbison, K. Müllen, *Adv. Mater.,* 11, 1469, 1999.
7. E. M. García-Frutos, E. Gutierrez-Puebla, M. A. Monge, R. Ramírez, P. de Andrés, A. de Andrés, R. Ramírez, B. Gómez-Lor, *Org. Electr.,* 10, 643, 2009.
8. S. Xiao, M. Myers, Q. Miao, S. Sanaur, K. Pang, M. L. Steigerwald, C. Nuckolls, *Angew. Chem. Int. Ed.,* 44, 7390, 2005.
9. X. Feng, V. Marcon, W. Pisula, M. R. Hansen, J. Kirkpatrick, F. Grozema, D. Adrianenko, K. Kremer, K. Müllen, *Nat. Mater.,* 8, 421, 2009.
10. C. Li, M. Liu, N.G. Pschirer, M. Baumgarten, K. Müllen, *Chem. Rev.,* 110, 6817, 2010.
11. H. Sasabe, J. Kido, *Chem. Mater.,* 23, 621, 2010.
12. A.C. Grimsdale, K. Leok Chan, R.E. Martin, P.G. Jokisz, A.B. Holmes, *Chem. Rev.***,** 109, 897, 2009.
13. A. Pron, P. Gawrys, M. Zagorska, D. Djurado, R. Demadrille, *Chem. Soc. Rev.,* 39, 2577, 2010.
14. H. Dong, C. Wang, W. Hu, *Chem. Commun.,* 46, 5211, 2010.
15. J.A.A.W. Elemans, R. van Hameren, R.J.M. Nolte, A.E. Rowan, *Adv. Mater.,* 18, 1251, 2006.
16. J.W. Steed, J.L. Atwood, Supramolecular Chemistry. Second ed., Wiley, 2009.
17. M.R. Wasielewski, *Acc. Chem. Res.***,** 42, 1910, 2009.
18. T. Kato, N. Mizoshita, K. Kishimoto, *Angew. Chem. Int. Ed.,* 45, 38, 2006.
19. T. Kato, T. Yasuda, Y. Kamikawa, M. Yoshio, M., *Chem. Commun.,*729, 2009.
20. M. Lehmann, *Chem.-Eur. J.***,** 15, 3638, 2009.
21. S. Sergeyev, W. Pisula, Y.H. Geerts, *Chem. Soc. Rev.***,** 36, 1902, 2007.
22. B.R. Kaafarani, *Chem. Mater.,* 23, 378, 2011.
23. S. Laschat, A. Baro, N. Steinke, F. Giesselmann, C. Hägele, G. Scalia, R. Judele, E. Kapatsina, S. Sauer, A. Schreivogel, M. Tosoni, *Angew. Chem. Int. Ed.,* 46, 4832, 2007.
24. R.J. Bushby, O.R. Lozman, *Curr. Opin. Solid State Mat. Sci.,* 6, 569, 2002.
25. W. Pisula, X. Feng, K. Müllen, *Adv. Mater.,* 22, 3634, 2010.
26. K. Isoda, T. Yasuda, T. Kato, *Chem.-Asian J.,* 4, 1619, 2009.

27. M. Talarico, R. Termine, E.M. García-Frutos, A. Omenat, J.L. Serrano, B. Gómez-Lor, A. Golemme, *Chem. Mater.,* 20, 6589, 2008.
28. Z. Chen, V. Stepanenko, V. Dehm, P. Prins, P. Siebbeles, D.A. Laurens, J. Seibt, P. Marquetand, V. Engel, F. Würthner, *Chem.-Eur. J.,* 13, 436, 2007.
29. A. Hayer, V. de Halleux, A. Köhler, A. El-Garoughy, E.W. Meijer, J. Barberá, J. Tant, J. Levin, M. Lehmann, J. Gierschner, J. Cornil, Y.H. Geerts, *J. Phys. Chem. B,* 110, 7653, 2006.
30. M. Lehmann, G. Kestemont, R.G. Aspe, C. Buess-Herman, M.H.J. Koch, M. Debije, J. Piris, M.P. de Haas, J.M. Warman, M.D. Watson, V. Lemaur, J. Cornil, Y.H. Geerts, R. Gearba, D.A. Ivanov, *Chem.-Eur. J.,* 11, 3349, 2005.
31. V. de Halleux, J.P. Calbert, P. Brocorens, J. Cornil, J.P. Declercq, J.L. Bredas, Y. Geerts, *Adv. Funct. Mater.,* 14, 649, 2004.
32. L. Schmidt-Mende, A. Fechtenkotter, K. Mullen, E. Moons, R.H. Friend, J.D. MacKenzie, *Science,* 293, 1119, 2001.
33. M. Gharbia, A. Gharbi, H.T. Nguyen, J. Malthête, *Curr. Opin. Colloid Interface Sci.,* 7, 312, 2002.
34. B.P. Hoag, D.L. Gin, *Adv. Mater.,* 10, 1546, 1998.
35. T. Yasuda, K. Kishimoto, T. Kato, *Chem. Commun.,* 32, 3399, 2006.
36. T. Yasuda, H. Ooi, J. Morita, Y. Akama, K. Minoura, M. Funahashi, T. Shimomura, T. Kato, *Adv. Funct. Mater.,* 19, 411, 2009.
37. A. Pérez, J.L. Serrano, T. Sierra, A. Ballesteros, D. de Saá, J. Barluenga, *J. Am. Chem. Soc.,*133, 8110, **2011.**
38. E. Hendrickx, Y. Zhang, K. B. Ferrio, J. A. Herlocker, J. Anderson, N. R. Armstrong, E. A. Mash, A. P. Persoons, N. Peyghambarian, B. Kippelen, *J. Mater. Chem.*, 9, 2251, 1999.
39. G. Hernandez-Sosa, N.E. Coates, S. Valouch, D. Moses, *Adv. Funct. Mater.,* 21, 927, 2011.

Chapter 4

OPV: INTRODUCTION

The objective of this chapter is to review the basic understanding of organic solar cells. The physical processes leading to the final current generation and the limiting factors of these cells will be discussed.

4.1 Solar energy

What can be a more attractive way of producing energy than harvesting it directly from sunlight? The amount of energy that the Earth receives from the Sun is enormous: 1.75×10^{17} W. Earth receives enough energy to fulfill the yearly world demand of energy in less than an hour. Not all of that energy reaches the Earth's surface due to absorption and scattering. The photovoltaic conversion of solar energy remains an important challenge State-of-the-art inorganic solar cells have a record power conversion efficiency of close to 39 %,[1] while commercially available solar panels, have a significant lower efficiency of around 15–20%.

Practically all conventional inorganic solar cells incorporate a semiconductor which is doped to form a p-n junction across which the photo voltage is generated. The p side contains an excess of positive charges (holes), and the n side contains an excess of negative charges (electrons). In the region near the junction an electric field is formed and the electrons and holes, which are generated through light absorption in the bulk of Si, diffuse to this junction, where they are directed by the electric field towards the proper electrode. Over the years, solar cells have been made from many semiconductor materials with various device configurations such as single-crystal, polycrystalline, and amorphous thin-film structures. At present, crystalline Si solar cells are dominant and account for more than 85% of the market. A comprehensive review on Si and other types of solar cells can be found in literature[2].

Although in the last 10 years the production of PV modules is increased steadily by an annual average of 40 %, the semiconductor PV still accounts for less that 0.1 % of the total world energy production. One of the major obstacles for the market implementation of PV cells is the large production costs for Si based technology.

However, despite much effort of further reducing the price, large scale production of Si-based solar cells will be limited by the availability of raw materials, such as solar-grade Si. Therefore, to ensure a sustainable technology path for PVs, the development of new materials and device structures are required.

4.2 Development of Photovoltaics

The photovoltaic effect was discovered in 1839 by Becquerel[3] . However, it was not until 1883 that Charles Fritts developed the first solar cell, based on selenium[4]. In 1954 Chaplin et al. from Bell Laboratories found that silicon doped with certain impurities was very sensitive to light[5]. This led to the first practical solar cells, with power conversion efficiency of around 6% at an estimated production cost of US$ 200 per Watt[6]. Spacecraft provided the main application during the next 20 years, where the necessities of low weight and reliability, made the cost of the cells unimportant. In the 1970s oil embargoes led to a sudden interest in alternative sources of energy, and the first modern solar modules for terrestrial use were fabricated in 1976[7]. The development of solar cells can be divided in three generations, as described below.

First Generation Devices were based on silicon wafers (such as those developed by Bell Laboratories) are termed the "first generation" of photovoltaic cells. Development of this technology continues up to the present, with economies of scale and increases in efficiency driving reductions in cost. The current cost of these photovoltaics is ~ US$ 4/Wp (watt-peak: a unit of power output giving the maximum power in watts of a 1 m^2 panel at 25 $^{\circ}$C), which is still too high to have a significant impact on the energy production market.

The second generation of photovoltaic materials were based on thin film technologies not requiring the use of silicon wafers. This enables them to be produced at a significantly lower cost. Materials and technologies under investigation or in production include amorphous silicon, cadmium telluride and copper indium gallium selenide (CIGS)[8].

For solar cells to achieve truly competitive cost to efficiency ratios, significant breakthroughs in technology are likely to be required. Such technologies are known as **"third generation"** photovoltaics. These are broadly defined as semiconductor devices which do not rely on traditional p-n junctions to separate photogenerated charges. "Third

generation" technologies can be divided into IIIa and IIIb. The solar cells in IIIa aim for very high efficiencies, thus the allowed cost of the cell can be quite high. Possible technologies include hot carriers, multiple electron-hole pair creation, and thermo-photonics. The goal of IIIb devices is to achieve moderate efficiency with very low cost. It is in this area that organic based photovoltaic devices are likely to have a significant short/mid term impact. Cost efficiency analyses for each of the generations are shown in Fig. 4.1[8]

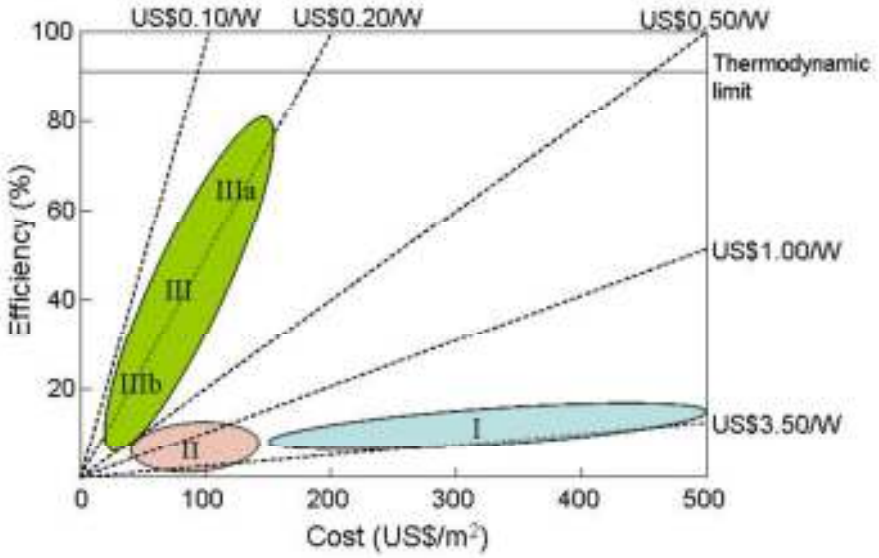

Figure 4.1. Cost efficiency analysis of first, second, and third (IIIa and IIIb) generation photovoltaic devices. [from ref.8]

The improvements in the efficiency of solar cells in different generations over the years is summarized in the Fig. 4.2. This graph was published by the NERL, USA[9]. Some of the advantages of organic materials, such as small organic molecules and polymers, are inherently inexpensive to implement. For example, as materials can have high absorption coefficients[10], films with thickness of the order of 100 nm can be used, reducing costs. Devices can be fabricated using high throughput, low temperature processes such as printing[11], spray coating, spin coating etc, and since these processes require less energy than that required for the manufacture of silicon based devices, the production costs are lower. There is also the possibility of using flexible plastic substrates for organic photovoltaic devices[12- 13]. This will allow them to be integrated into building structures in ways impossible for conventional solar cells. In addition to the advantages in fabrication, there are significant advantages resulting from the flexibility in the synthesis

of the molecules, which allows parameters such as the molecular weight, energy levels, band-gap, and solubility to be altered. Combined with the physical fabrication advantages, these chemical properties make the organic solar cell an incredibly versatile design.

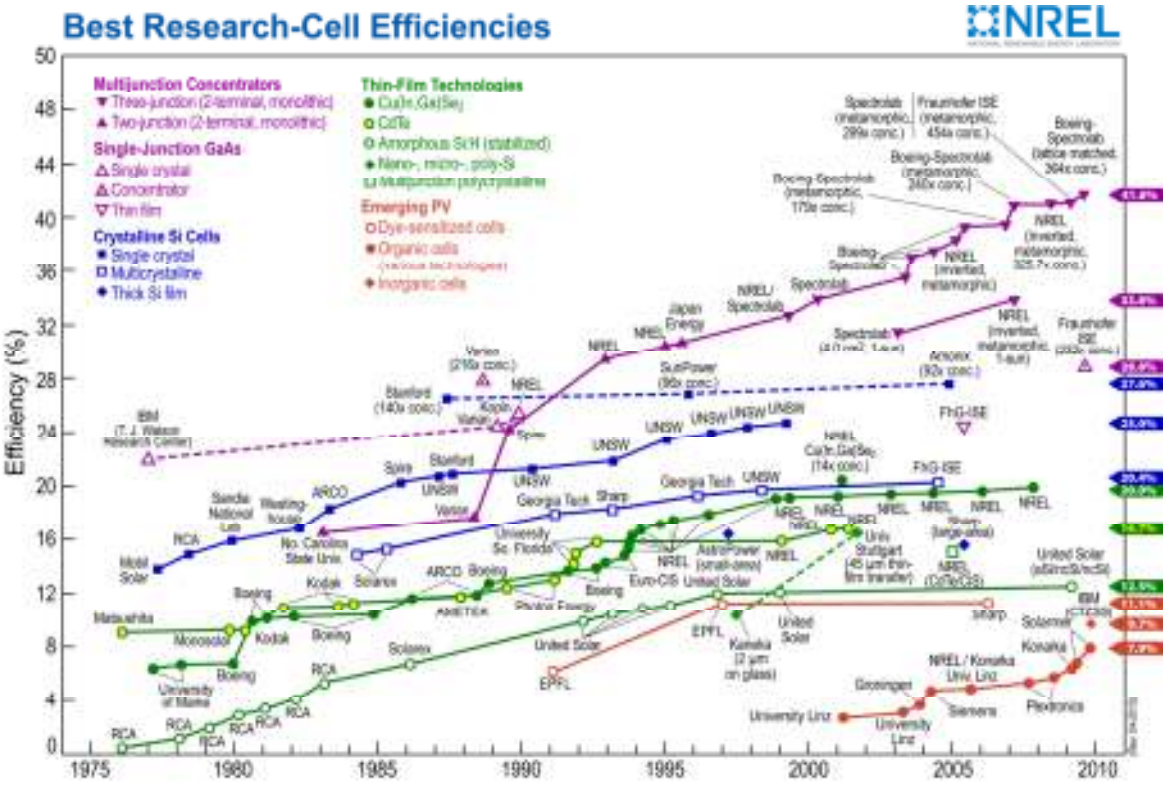

Figure 4.2. Development of OPV (in η (%)) over the years. [from ref. 9]

However, organic materials also introduce challenges not seen in conventional devices. The principal challenge is, producing devices which have high enough efficiencies and lifetimes and low enough cost to make them commercially viable. Market entry values are around 10 % device efficiency (and a module efficiency of 5 %), a lifetime of 3 - 5 years, and ideally a cost of less than US$ 1/Wp[12]. Organic light emitting diodes (OLEDs) are now showing reasonable lifetimes at high injection currents (over 20 000 hours at room temperature and luminance up to 100 cdm^{-2}[14]), and it would appear likely that organic photovoltaic devices can use these developing techniques to increase lifetimes. To improve the efficiency both material properties and device fabrication need to be optimized. The required improvement in the materials requires a greater understanding of the underlying physics involved, and it is in this area that this thesis

concentrates on. In the next two sections the parameters measured to calculate the power conversion efficiency are outlined, along with the various device structures used in organic solar cells.

4.3 Solar Cell Parameters

Photovoltaic devices convert sunlight into electricity. The power conversion efficiency of a cell, η, is the ratio of the maximum power generated by the device, P_{out}, to the incident power, P_{in}, due to sunlight, and is generally expressed as:

$$\boldsymbol{\eta = \frac{P_{out}}{P_{in}}} \quad (1)$$

The power generated by a device can experimentally be determined from a current versus voltage (I-V) curve. An example of such curve is shown in Fig. 4.3. The power generated is:

$$\boldsymbol{P_{out} = I_{mp} V_{mp}} \quad (2)$$

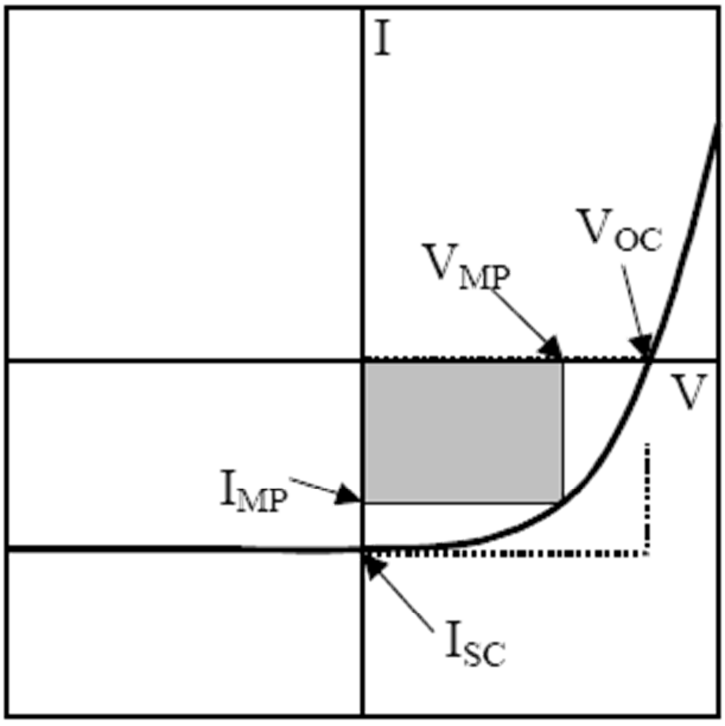

Figure 4.3. Typical I-V curve of a photovoltaic cell.

where P_{out} is the maximum power point and is given by the product of I_{mp} and V_{mp}, see Fig. 4.3. Alternatively, P_{out} can be expressed as:

$$\boldsymbol{P_{out} = FFV_{oc}I_{sc}} \quad (3)$$

where I_{sc} is short circuit current and is defined to be the current produced with zero bias voltage, V_{oc} is the open circuit voltage and is the applied bias at which no current flows since the photogenerated current exactly cancels the dark current. The fill factor (FF) describes how well the maximum power rectangle fills the area of the I-V curve. From Eqn. (2) and (3) the FF is defined to be:

$$\boldsymbol{FF = \frac{I_{mp}V_{mp}}{I_{sc}V_{oc}}} \quad (4)$$

I_{sc}, V_{oc}, and FF are often quoted along with the power conversion efficiency η, and in order to achieve maximum power conversion efficiency each of these parameters needs to be optimized.

4.4 Modeling of Organic solar cell

An organic solar cells (OSC) can be modeled as a current source in parallel to a diode. The equivalent circuit of an OSC is shown in Fig. 4.4a. The OSC behaves like a diode in the dark and the current which flows through it under an applied voltage is referred to as the dark current, $I_{dark}(V)$. Under illumination, the diode current I_D acts in a direction opposite to the photocurrent (I_{Ph}) reducing the net current. This diode current is approximated to be equal to I_{dark}. Although I_D is the diode current under illumination and is not formally equal to I_{dark}, the approximation is reasonable for most photovoltaic materials. The current I, which flows in an ideal OSC under illumination, can be written as.

$$\boldsymbol{I = I_{Ph} - I_D = I_{Ph} - I_{dark} = I_{Ph} - I_0\left(e^{\frac{eV}{KT}} - 1\right)} \quad (5)$$

where I_o is the saturation current of the diode, e is the elementary charge, K is the Boltzmann constant, T is the temperature and V is the produced OSC voltage or applied bias.

Fig. 4.4b shows a typical current-voltage (I-V) characteristic of an OSC in the dark and under illumination. The short circuit current (I_{sc}) is the current that flows under short circuit conditions. The open circuit voltage (V_{oc}) is the voltage at which the

photocurrent generated is zero or in other words the voltage across the open terminals of an OSC.

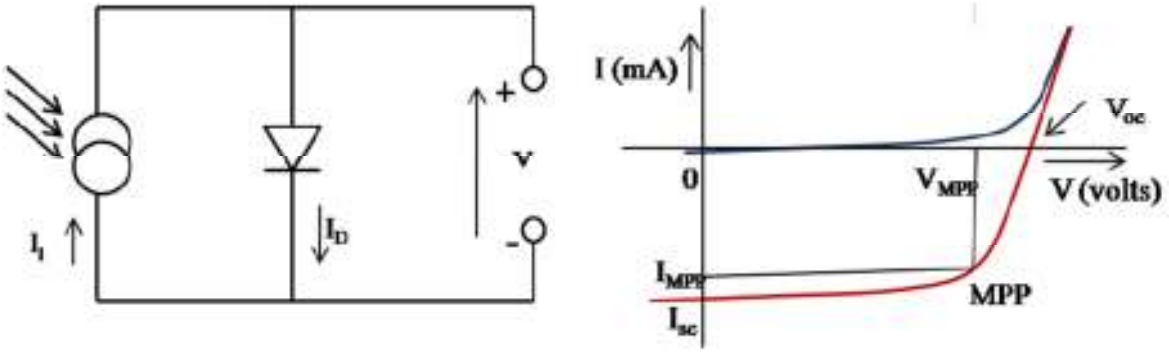

(a) **(b)**

Figure 4.4: (a) Equivalent circuit of an OSC. (b) Characteristic curve for an OSC in the dark (blue) and under illumination (red).

The operating region of an OSC is in a bias range from 0 to V_{oc}, where the OSC generates power. For this reason the fourth quadrant of the I-V curve is also known as the power quadrant.

A real OSC seldom reaches its theoretical best performance because power dissipates through internal resistance and current leakage. These effects are electrically equivalent to two parasitic resistances: the series resistance (R_s) arises from the active material resistivity to charge flow and from the contacts; the shunt (or parallel) resistance (R_{sh}) is due to current leakage. The equivalent circuit for an OSC when these two parasitic resistances are included is shown in Fig. 4.5 and the equation describing the current becomes:

$$\boldsymbol{I = I_{Ph} - I_0\left(e^{\frac{e(V+IR_S)}{nKT}} - 1\right) - \frac{(V+IR_{sh})}{R_{sh}}} \quad (6)$$

where n ($1 < n < 2$) is the diode ideality factor.

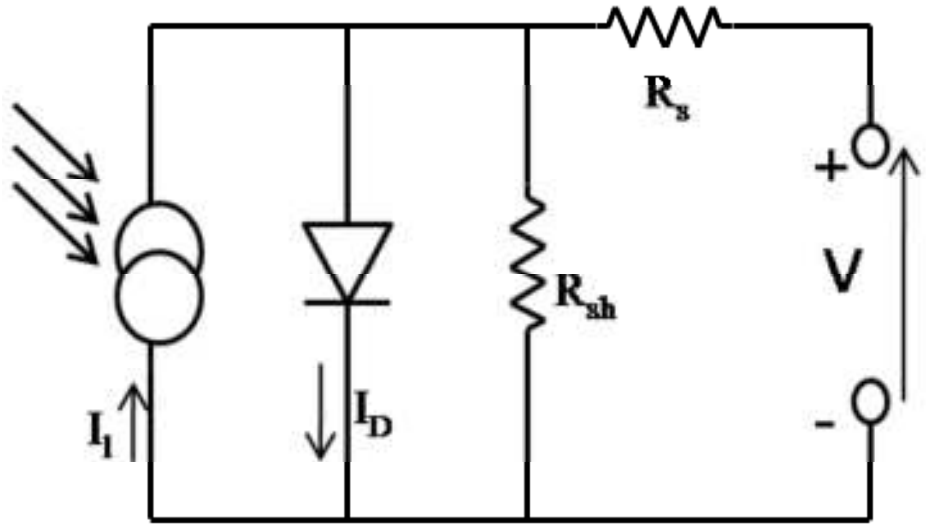

Figure 4.5: Equivalent circuit of an OSC with R_s and R_{sh}.

Ideally, for an efficient OSC, R_s should be minimized ($R_s \rightarrow 0$) and R_{sh} should be maximized ($R_{sh} \rightarrow \infty$). The effects of an increasing R_s or a decreasing R_{sh} on the I-V curves are shown in Fig. 4.6.

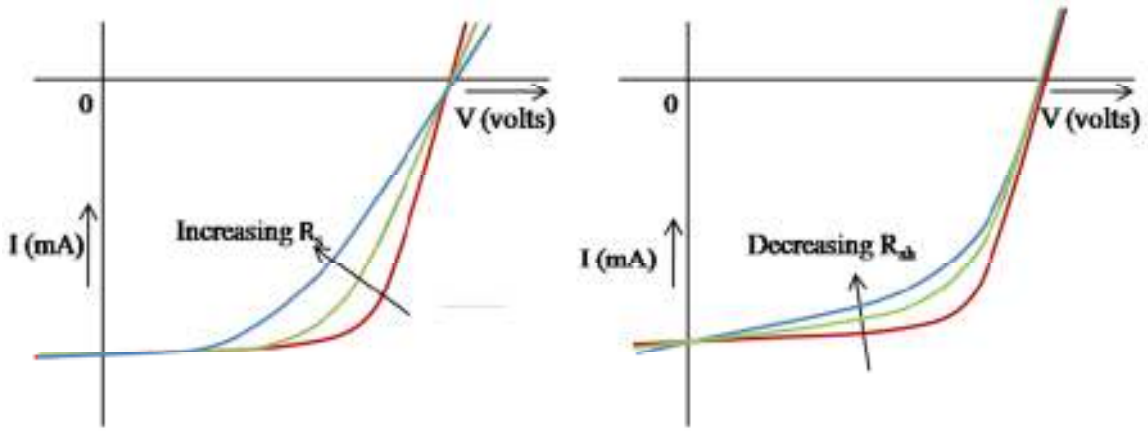

(a) **(b)**

Figure 4.6: Effect of increasing **(**a**)** R_s and **(**b**)** R_{sh}.

4.5 Device Structure of photovoltaic

The basic structure of a photovoltaic device is shown in Fig. 4.7, the active material is sandwiched between two metallic electrodes which act as anode and cathode. To allow photons to be absorbed in the active material, at least one of the electrodes must be transparent to sunlight. Indium tin oxide (ITO), which fulfills the transparency requirement (> 90%), is generally used. Materials for the second electrode include calcium with a layer of aluminium evaporated on top to prevent oxidization, aluminium by itself, lithium fluoride capped by aluminium, gold, and silver[15- 16]. In general, the two different electrodes will have different work functions, and this creates an electric field across the active material which may assist in drifting the photogenerated charge carriers. There is no generally consistent understanding within the literature as to how much the device parameters, particularly the open circuit voltage, are affected by the relative energy of the work function of the electrodes and of the frontier orbitals of the active material[17- 21].

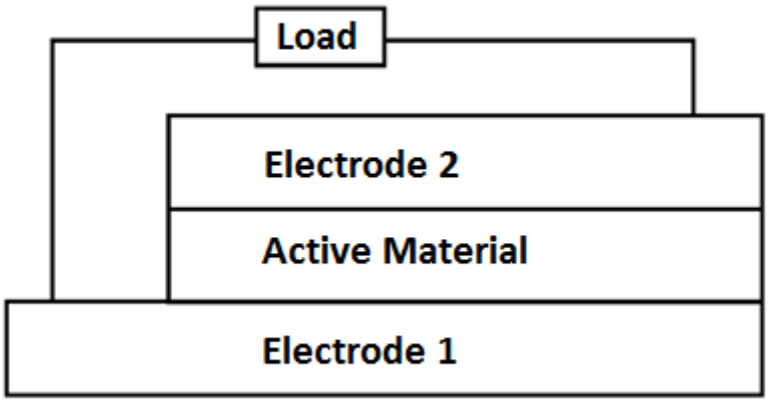

Figure 4.7. Photovoltaic device structure

There are several key requirements for the active materials. They should be broadband absorbers. Photo excitations in the active material produce excitons (excitons are basically bound electron-hole pairs), and these excitons must dissociate in order for charge transport to occur. Therefore, active materials should ideally have long exciton diffusion lengths, so that once an exciton is created it can reach an interface and be separated into charge carriers. In addition, the materials need to have good charge transport properties (mobility) for these charges to reach the respective electrodes rapidly,

before competing processes (trapping, recombination) can stop them. Finally, to be able to utilize these properties and to lower fabrication costs the material should be soluble (although this is not essential).

There can be different structures (commonly called heterojunctions when they include a junction between different materials) of OPV cells, as shown in Fig. 4.8. In the following the features of the main types of structures will be discussed.

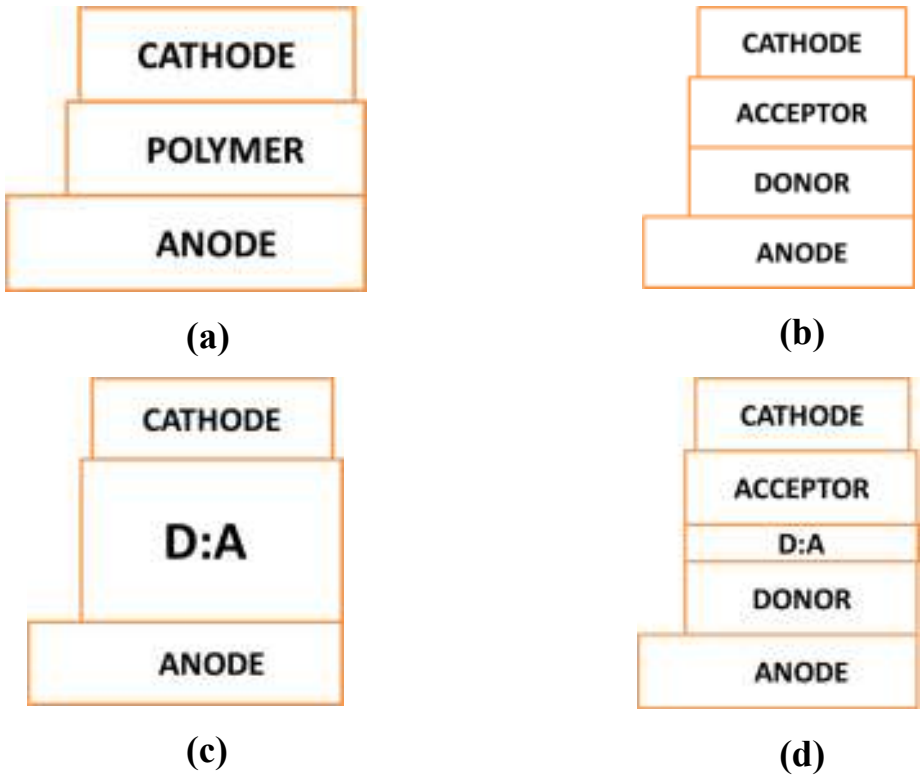

Figure 4.8: Schematic structure of three different molecular donor-acceptor heterojunction (HJ) structures: (a) single layer (b) planar or bilayer HJ, (c) mixed or bulk HJ, and (d) hybrid planar-mixed HJ.

4.5.1 Single Layer Devices

The first organic solar cells were based on a layer of polymer between two metal electrodes. In this structure there are only two interfaces at which excitons can dissociate. This, combined with the short exciton diffusion length in polymers (around 10 nm in polyphenylenevinylene (PPV)[22]) and poor electron mobility[23] results in very low efficiencies, generally between 10^{-3} and 10^{-1} %.

4.5.2 Bilayer Heterojunction Devices

The first demonstration of efficient photovoltaic response in an organic heterojunction structure was based on a bilayer or planer heterojunction (HT) structure[24]. In a bilayer heterojunction, donor (D) and acceptor (A) materials are stacked sequentially and sandwiched between two electrodes[25]. Charge separation occurs at the interface between the two active materials, with the highest occupied molecular orbital (HOMO) and lowest unoccupied molecular orbital (LUMO) levels of the donor higher than those of the acceptor[10, 26]. It is necessary to have a sufficiently large energy level offset at the DA interface to overcome the exciton binding energy, which is generally considered to be in the range of 0.1 to 0.2 eV[27- 29]. The separated charges then drift and diffuse towards the respective electrodes, where they are collected to contribute to a photocurrent or to a photovoltage. Again, due to the energy level misalignment at the DA interface, holes are confined and transported in the donor material, whereas electrons are confined and transported in the acceptor material, as shown in Fig. 4.9 Thus the opposite charges are physically separated from each other and unlikely to recombine.

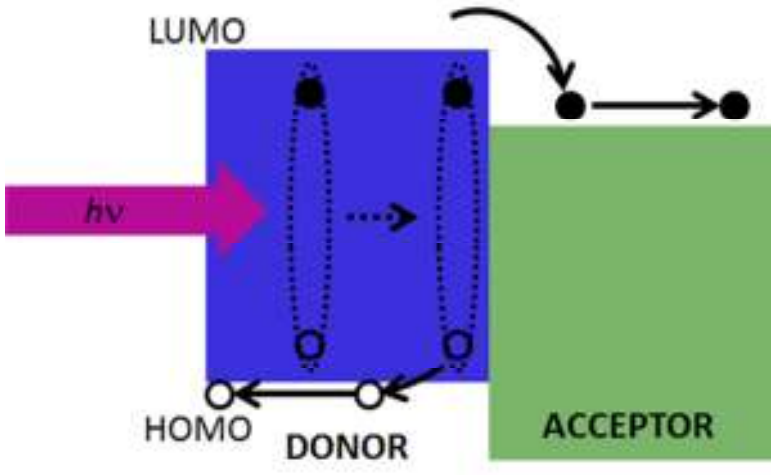

Figure 4.9: Schematic energy level diagram of a donor-acceptor heterojunction.

One of the major limiting factors to the efficiency of these planar HJ devices is the short exciton diffusion length of organic materials, L_{ED}, or the average distance excitons can diffuse in these materials before recombination. Due to the weak van der Waals type interactions among organic molecules[27] the exciton diffusion length is short, generally in

the order of a few nm[26]. In comparison, the light absorption length, L_A, for these photoactive organic materials are typically in the order of 50–100 nm (corresponding to an absorption coefficient of $(1–2)\times10^5$ cm^{-1}). Hence, only excitons created very close to the DA interface, e.g. roughly within an exciton diffusion length of the interface, can diffuse to the interface with a high probability and contribute to the generation of separated charge carriers. Excitons generated further away from the interface are more likely to undergo recombination and have less significant contribution to the photovoltaic process. To maximize the light absorption efficiency η_A, thick organic layers with thicknesses of at least L_A are needed; however, to maximize the internal quantum efficiency (η_{IQE}), thin layers with thicknesses of the order of L_{ED} are preferred so that most of the photogenerated excitons can diffuse to the interface and contribute to the photocurrent. As the external quantum efficiency $\eta_{EQE} = \eta_A \times \eta_{IQE}$, a fundamental trade-off exists between optical absorption and exciton diffusion in these planar HJ devices.

4.5.3 Bulk Heterojunction Devices (BHJ)

The idea of a bulk heterojunction is to blend the donor and acceptor materials so that an absorbing site is always within an exciton diffusion length of an interface. The donor and acceptor phases have to form an interpenetrating and bicontinuous network in order for the separated charges to have a percolation path to the electrode[10], as shown in Fig. 4.10. By controlling the phase separation of the two materials to several nanometers, the same length scale as the exciton diffusion lengths, one can expect most photogenerated excitons to have high probability of diffusing to a nearby DA interface and generate separated charge carriers upon dissociation. Furthermore, percolated pathways need to be formed for both materials in the bulk HJ for efficient collection of these charge carriers.

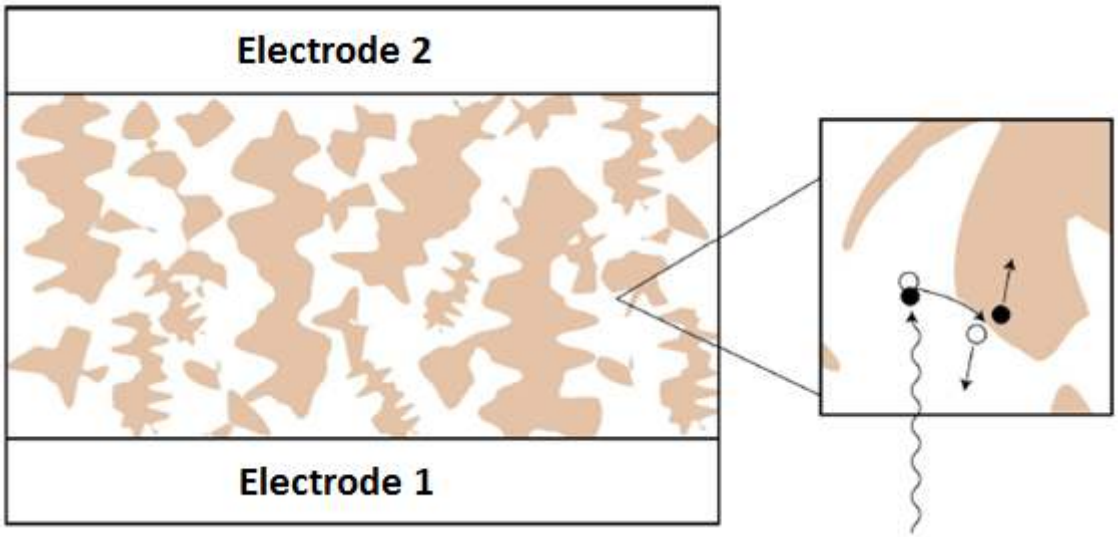

Figure 4.10. Morphology of bulk heterojunctions. The absorption of a photon leads to the formation of an exciton. The exciton can then diffuse to an interface between the two materials, and separate. The electron and hole travel to the appropriate electrode through the interpenetrating network.

Any morphological islands, bottlenecks, or cul-de-sacs in the BHJ will negatively affect the transport of charges and may lead to trapping and eventually the recombination of the charges. The formation of a good BHJ structure, however, is not trivial, as the morphology of the bulk HJ strongly depends on the properties of the donor and acceptor materials and the solution processing conditions, as well as any post-processing treatments.[30-33]. A minor modification on the polymer structure or a seemingly trivial change of the solvent used for the materials could lead to a significant change in the bulk HJ morphology, and eventually the performance of the corresponding PV cell.[34-36] .Devices using this structure are much more efficient than single layer devices, with efficiencies now around 7.0 %[34].

4.5.4 Planar-Mixed Donor-Acceptor Heterojunctions

As discussed above, exciton diffusion is a limiting process in a planar HJ cell, whereas charge transport/collection limits the performance of a mixed HJ cell. Hence, while thick layers are desired to maximize the absorption of the incident photons, thin layers are preferred to achieve high exciton diffusion efficiency η_{ED} (for planar HJ cells) or charge collection efficiency η_{CC} (for mixed HJ cells). A new type of HJ, called hybrid planar-mixed HJ, was therefore developed to combine the advantages of these two types

of HJs while mitigating their problems to some extent[37, 38]. The planar-mixed HJ (PM-HJ) consists of a mixed donor-acceptor layer sandwiched in between a pure donor layer and a pure acceptor layer. With relatively thin layers, the charge collection in the mixed layer and exciton diffusion in the pure layers are not seriously limited. The low absorption by thin layers is compensated by the fact that there are three layers in the PM-HJ all contributing to light absorption. Also due to the separate donor and acceptor layers at the opposite cathodes eliminates the possibility of recombination, which is one of the major disadvantages of bulk heterojunction solar cells.

4.6 Basic processes in an organic solar cell

Various device structures for organic solar cells have been investigated in recent years, as discussed above. In general, four important processes (as shown in Fig. 4.11) have to be optimized in order to obtain a high conversion efficiency of solar energy into electrical energy.

I. Absorption of light and generation of excitons. The incident light generates electron–hole pairs, in many cases due to electron transitions from π-HOMO to $\pi*$-LUMO levels (with the materials most commonly used, absorption is higher in the donor material); photon absorption depends on the value of the optical absorption coefficient and on the thickness of the active layer. The generation of an electron–hole pair, by photo excitation, results in an excited but neutral state with a limited, finite lifetime; this state is termed an exciton and consists of an electron and a hole paired by an energy (E_{ex}) that is smaller than the energy gap between the limits of the permitted bands (LUMO and HOMO bands, respectively). If E_G is the energy gap, then ($E_G - E_{ex}$) is the exciton binding energy (around 0.1 – 0.2 eV in organics).

II. Diffusion of the excitons. This quasi-particle diffuses as long as recombination processes (of the hole–electron pair which makes up the exciton) do not take place. Forster (long range, about 100 Å) or Dexter (between adjacent molecules, within 10 Å) transfers can take place between an excited molecule (considered as an excitation donor) and a molecule that receives the excitation (excitation acceptor). The exciton diffusion efficiency is always less than one because various recombination processes can occur.

III. Dissociation of the excitons with generation of "free" charge. If its diffusion length is sufficiently long that the exciton meets an internal field, hole and electron separation occurs. This is very different from what happens in inorganic materials, where the exciton binding energy is of the same order, or lower, than thermal energy and the dissociation does not require any additional driving force. In organics instead, the exciton binding energy is of the order of 0.5 eV, much higher than k_BT at room temperature. The internal field may be obtained at a donor – acceptor interface, provided the frontier orbitals energies of acceptor and donor are properly positioned.

IV. Charge transport and charge collection. In organic materials, charge transport involves the classical mechanism of hopping. Traps can reduce the mobility. If carriers are not infinitely trapped (as for example in lattice defects such as dislocations), the charge transport efficincy η_{tr} can be considered 100 %. For charge collection to occur most efficiently, the following conditions must be fullfilled: the work function of cathode < (E_{LUMO}) acceptor and work function of anode > (E_{HOMO}) donor. When this condition is fulfilled, the charge collection efficiency will be ~ 100 %.

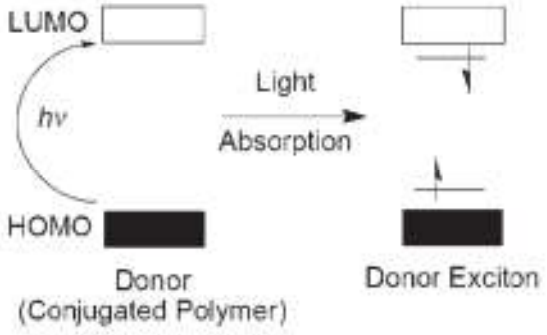

Step-1

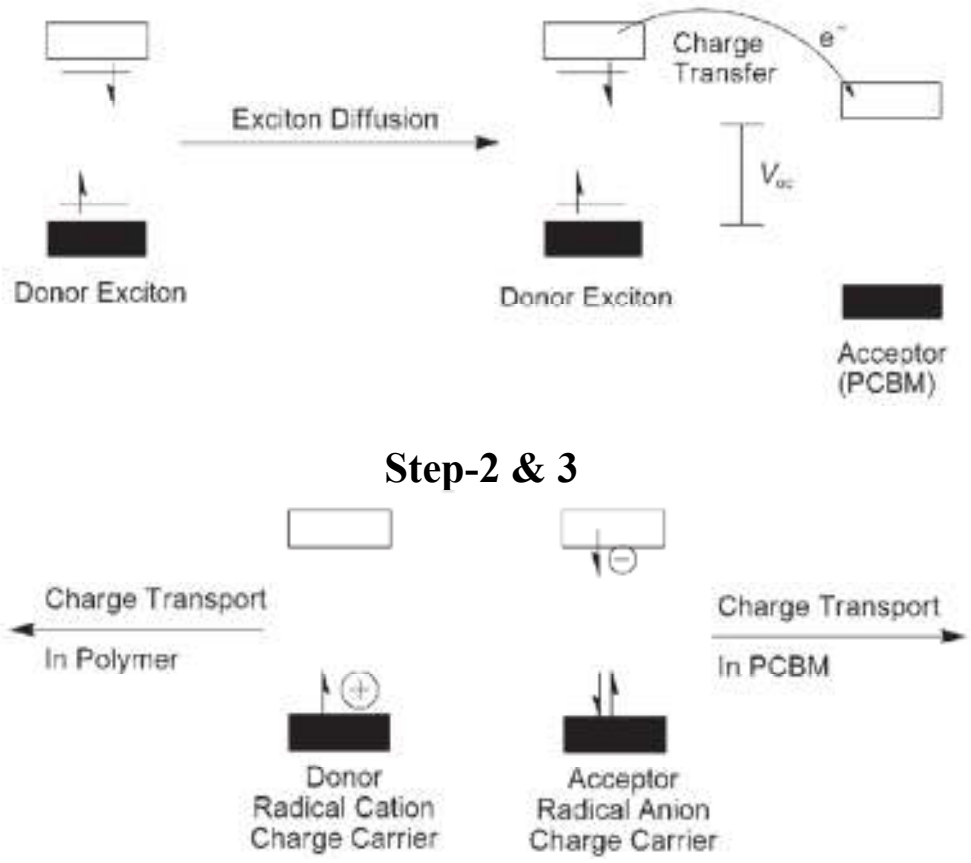

Figure 4.11: General mechanism of energy conversion in OPV when the absorption is in the donor material.

The elementary steps involved in the pathways from light absorption to the generation of free charges are shown in Fig 4.12.[39, 40].

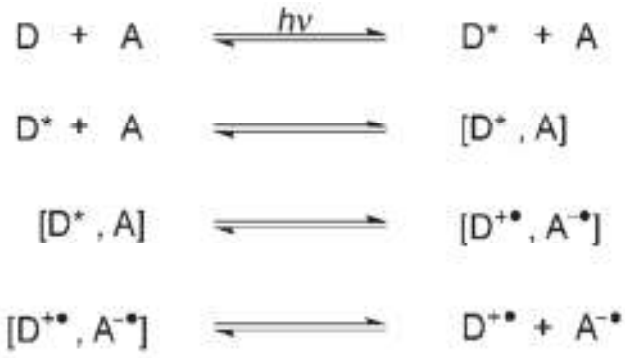

Figure 4.12: Elementary steps in the process of photoinduced charge separation for a donor (D) and an acceptor (A): 1) Photoexcitation of the donor; 2) diffusion of the exciton and formation of an encounter pair; 3) electron transfer within the encounter pair to form a geminate pair; 4) charge separation.

The processes can also occur in an analogous fashion in the case of an excited acceptor, and the details of these mechanistic steps have been described extensively in the literature[40].

It is apparent that the active layer of donor–acceptor composite governs all aspects of the mechanism, with the exception of charge collection, which is based on the electronic interface between the active layer composite and the electrodes. Besides the fundamental mechanistic steps, the open circuit voltage (Voc) is also governed by the energetic relationship between the donor and the acceptor (Fig. 4.11) rather than the work functions of the cathode and anode, as would be expected from a simplistic view of these diode devices. Specifically, the energy difference between the HOMO of the donor and the LUMO of the acceptor is found to most closely correlate with the Voc value[17, 20].

It is therefore apparent that the choice of the components in the active layer, as well as its morphology, which governs the physical interaction between the donor and acceptor, are the primary factors affecting the performance of the device.

4.7 Optimizing the bulk heterojunction nanomorphology

The requirement of an intimate intermixing of donor and acceptor phases in the bulk heterojunction makes this approach especially sensitive to the nanoscale morphology of the active layer. For solvent processed systems, there is a strong dependence of the final morphology of the active layer on the specific solvent used,[18, 30, 41, 42] solvent evaporation time,[43, 44] surface interactions[45] and post production annealing[46-50]. Moreover, the donor-acceptor composition is another factor determining the resulting morphology[51-53]. The main processes directly affected by the morphology are the exciton diffusion and subsequent dissociation as well as the charge transport to the electrodes. Therefore, the morphology has a strong impact on the overall solar cell performance.

To achieve high quantum efficiency, all photogenerated excitons have to reach and dissociate at a donor– acceptor interface, and subsequently all created charges have to reach the respective electrodes. However, power conversion efficiencies of solar cells using covalently attached mixtures of donor–acceptor materials are rather low, indicating loss mechanisms due to enhanced recombination and poor charge-carrier transport. This leads to the conclusion that intimate mixing may result in too small mean free paths.

Thus, the critical issue will not only be the relationship between molecular structure and device properties but also between nanomorphology and device properties (Fig. 13).

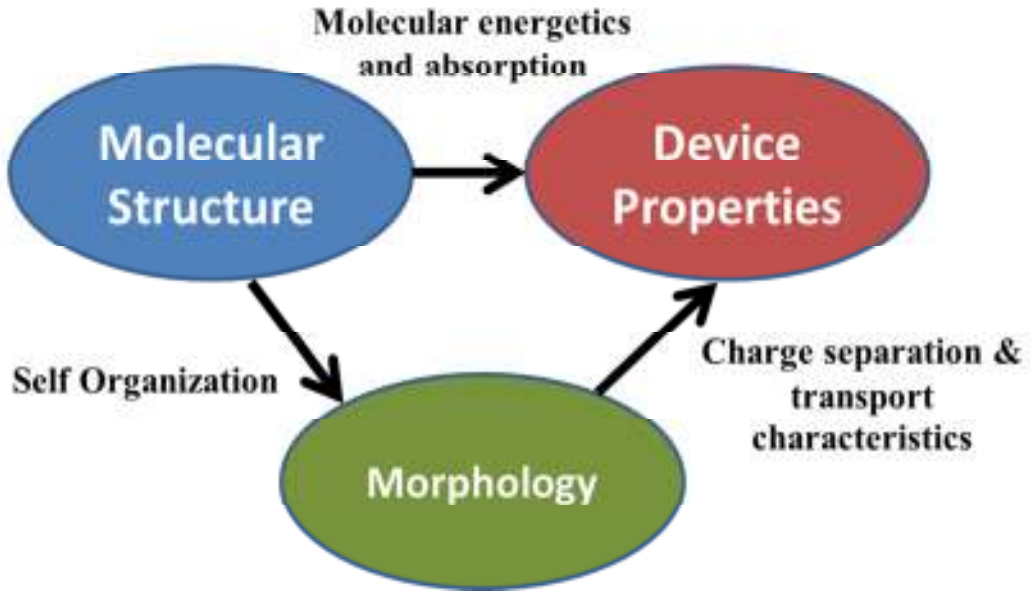

Figure 4.13: In organic or hybrid bulk heterojunction solar cells, the molecular structure, nano scale morphology and device properties are closely interrelated. Hence, the design of advanced organic solar cells requires the simultaneous optimization of these closely interconnected parameters.

4.8 How to improve BHJ efficiency

In order to improve the BHJ efficiency, new combinations of materials that are being developed in various laboratories focus on improving the three important parameters parameters *i.e.*

1. Short circuit current
2. Open circuit voltage
3. Fill factor

Such parameters and their dependence on the various factors will be discussed in detail in the following.

4.8.1 Tuning of short circuit current

Tuning of short circuit current for an efficient solar cell can be achieved by:

1. One of the crucial parameters for increasing the short circuit currentt is the absorption of more photons. This may be achieved by increasing the layer thickness and by shifting the absorption spectrum of the active layer to longer wavelengths. Although the first improvement may seem trivial at first sight, an increase of the layer thickness is presently limited by the charge carrier mobility and lifetime. When the mobility is too low or the layer too thick, the transit time of photogenerated charges in the device becomes longer than the lifetime, resulting in charge recombination. The absorption of the active layer in state-of-the-art devices currently spans the wavelength range from the UV up to about ~650 nm. In this wavelength range the monochromatic external quantum efficiency can be as high 70% under short-circuit conditions, implying that the vast majority of absorbed photons contribute to the current. The intensity of the solar spectrum, however, maximizes at ~700 nm and extends into the near infrared. Hence, a gain in efficiency can be expected when using low-band gap materials.
2. By efficient charge generation and transfer between donor and acceptor materials.
3. Increasing the charge transport properties, material morphology in the active layer and optimizing active layer film thickness.

4.8.2 Tuning open circuit voltage

For ohmic contacts the open-circuit voltage of bulk-heterojunction polymer photovoltaic cells is governed by the difference between the energy levels of HOMO and the LUMO of donor and acceptor, respectively. In most polymer/fullerene solar cells, the positioning of these band levels of donor and acceptor is such that up to ~0.4–0.8 eV is lost in the electron-transfer reaction. By more careful positioning of these levels, it is possible to raise the open-circuit voltage well above 1 V. A very encouraging result in this respect is PFDTBT that gives Voc = 1.04 V in combination with PCBM[54] compared to 0.8–0.9 V for MDMO-PPV and 0.5–0.6 V for P3HT. Because, the open-circuit voltage of bulkheterojunction solar cells is governed by the HOMO of the donor and the LUMO levels of the acceptor, the most promising strategy seems to lower the band gap by

adjusting the other two levels, *i.e.* decrease the LUMO of the donor, or increase the HOMO of the acceptor, or both.The tradeoff of increasing the donor-HOMO to acceptor-LUMO energy is that eventually a situation will be reached in which the photoinduced electron transfer is held back by a loss of energy gain.

The value of V_{oc} is also influenced by the contacts between active layer with the electrodes and the morphology of active layer. Mentioned earlier that, efficiency of a solar cells mainly depends on the V_{oc}, I_{sc} and FF. With a fill factor to 65% and neglecting any contribution from photons absorbed by the fullerene, Scharber et al. calculated the expected efficiency of a bulk heterojunction as a function of the band gap and the LUMO level of the donor[21] demonstrating that solar cell efficiency up to 10% is possible as shown in Fig. 4.14.

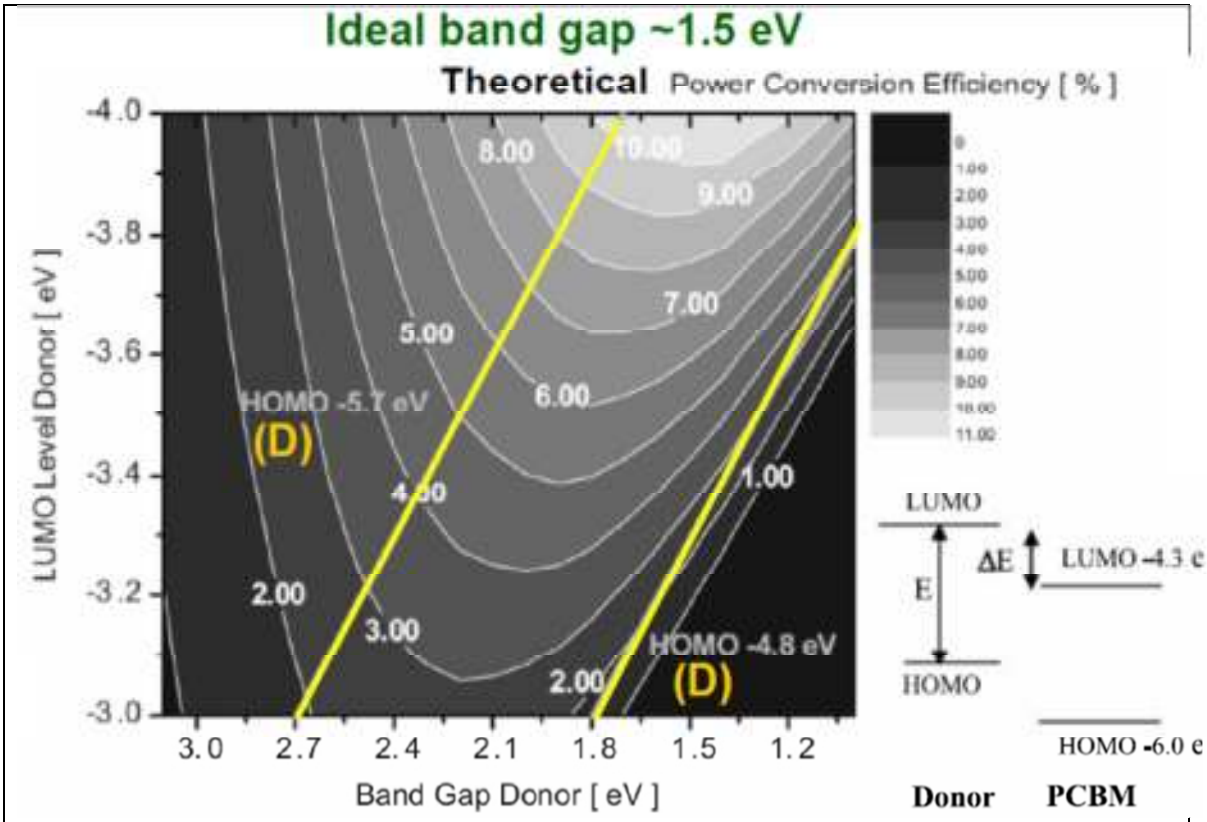

Figure 4.14: Contour plot showing the calculated energy-conversion efficiency (contour lines and colours) versus the bandgap and the LUMO level of the donor polymer. Straight lines starting at 2.7 and 1.8 eV indicate HOMO levels of -5.7 and -4.8 eV, respectively. A schematic energy diagram of a donor PCBM system with the band-gap energy (E_g) and the energy difference (ΔE) is also shown. [from ref. 21]

4.8.3 Tuning Fill Factor

A high fill factor (strongly curved *J-V* characteristic) is advantageous and indicates that fairly strong photocurrents can be extracted close to the open-circuit voltage. In this range, the internal field in the device that assists in charge separation and transport is fairly small. Consequently a high fill factor can be obtained when the charge mobility of both charges is high. Presently the fill factor is limited to about 60% in the best devices, but values up to 70% have been achieved recently[55].

Moreover, the fill factor of a device also depends on the series resistance[56] of the solar cell. Series resistance in solar cell is attributed to the finite conductivity of the semiconducting material, the contact resistance between the semiconductors and the adjacent electrodes, and the resistance associated with electrodes and interconnections. In a solar cell, lower the series resistance better will be the fill factor. Morphology of the active layer also governs the fill factor of the cell and hence must be kept into account.

Adding an addition thin layer of calcium or lithium floride[57] between the active layer and cathode were also help in improving the fill factor, however, it is still the research topic that whether it is due to the ohmic contact or dipole moment induced by these layers between the active layer and cathode.

Apart from developing improved materials, a further gain in device performance can be expected from the combined optimization of the optical field distribution present in the device. Optical effects, such as interference of light in multilayer cavities, have received only limited attention so far but will likely contribute to a better light-management in these devices.

4.9 Some higher efficiency materials for BHJ solar cells

Some high prforming materials in organic photovoltaics based on both, conjugated polymers and low molecular weight materials are discussed in following:

4.9.1 Polymer based systems

During the last few years, progress in polymer/fullerene based solar cells was so rapid that new efficiency records were frequently claimed in various published articles. Recently, world record 7.6% efficiency was announced by Solarmer[58]. Progress has been continuous, with successive developments in material design and synthesis and control of the morphology of the bulk heterojunction polymer-based composites. Some of the most useful polymers are shown in Fig. 4.15.

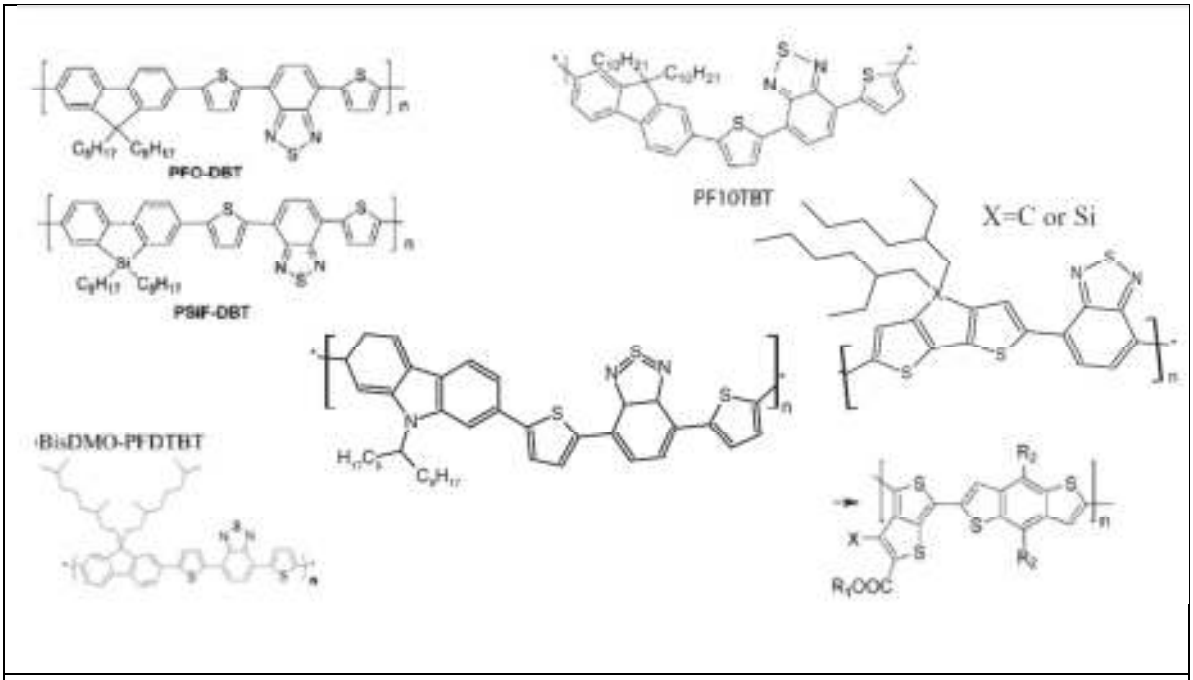

Figure 4.15: Chemical structure of a few prominent polymers which gave efficiencies in the order of or above 5%. [from ref. 59]

4.9.2 Low molecular weight (LMW) based systems

Although most research in the field of organic bulk heterojunction solar cells has focused on combinations of a p-type conducting polymer as a donor and a fullerene-based acceptor, recent work has demonstrated the viability of solution-processed heterojunctions composed entirely of low molecular weight (LMW) materials. LMW

offer potential advantages over conjugated polymer systems in terms of structural definition, synthesis, easier purification, amenability to mass-scale production and better batch-to-batch reproducibility.

Recent work has demonstrated that it is possible to solution process BHJ comprising non-polymeric donor and acceptor phases, that are able to achieve power conversion efficiencies comparable to some of the best known polymer systems[60], such as poly 3-hexylthiophene (P3HT)[61, 62]. Some of the more recent successes in the field of LMW bulk heterojunction[63, 64], highlighting outstanding results from representative classes of materials including oligothiophenes, acenes, diketopyrrolopyrroles and push-pull type oligomers, as well as a few other dye-based materials, are shown in Fig. 4.16. Recently J. Zhou et. al. have reported a power conversion efficiency of 5.84 %, which is so far the best for all solution-processed bulk heterojunction based on LMW materials[65].

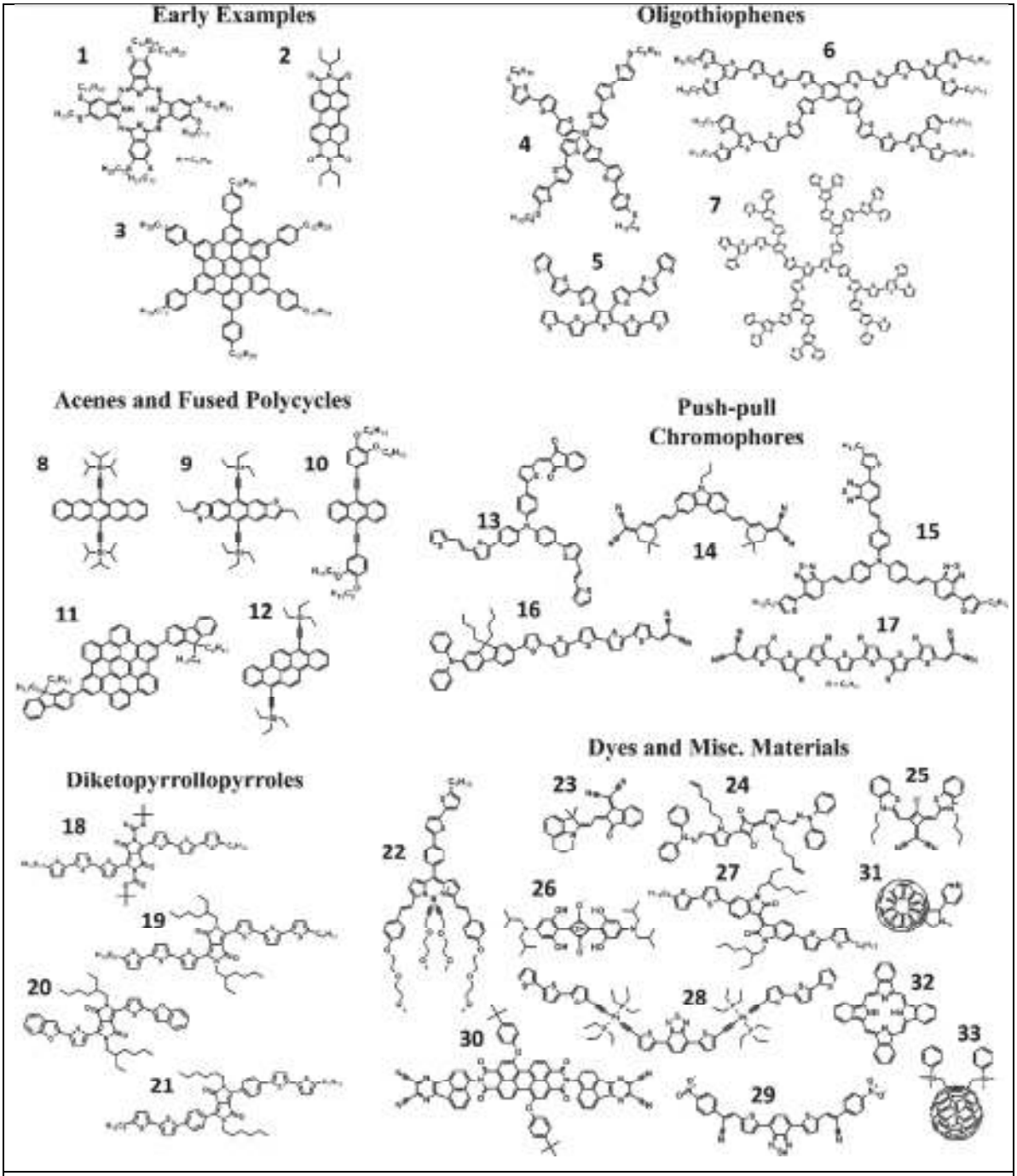

Figure 4.16: Examples of some most successful chemical structures reported in solution-processed organic solar cells using small molecules as donors reported in the literature. [from ref.66]

BIBLIOGRAPHY

1. United Nations Environment Programme (UNEP), *Global environment outlook (GEO year book 2004/5)*, Web site: www.unep.org/geo/yearbook.
2. A. Goetzberger, C. Hebling, H.W. Schock, *Materials Science & Engineering R-Reports,* 40, 1, 2003.
3. A.E. Becquerel, *Comptes Rendus de L'Academie des Sciences*, 9, 561, 1839.
4. C.E. Fritts, *American Journal of Science*, 26, 465, 1883.
5. D.M. Chapin, C.S. Fuller, G.L. Pearson, *Journal of Applied Physics*, 25, 676, 1954.
6. J. Nelson, The Physics of Solar Cells, Imperial College Press, 2003.
7. M.A. Green, *Progress in Photovoltaics*, 13, 447, 2005.
8. S.E. Shaheen, D.S. Ginley, G.E. Jabbour, *MRS Bulletin*, 30, 10, 2005.
9. http://www.nrel.gov/analysis/pubs_solar.html
10. H. Hoppe, N.S. Sariciftci, *Journal of Mater. Res.*, 19, 1924, 2004.
11. P. Schilinsky, C. Waldauf, C.J. Brabec. *Adv.Funct. Mater.*, 16, 1669, 2006.
12. C.J. Brabec, J.A. Hauch, P. Schilinsky, C. Waldauf, *MRS Bulletin*, 30, 50, 2005.
13. M. Al-Ibrahim, H.K. Roth, U. Zhokhavets, G. Gobsch, S. Sensfuss. *Solar Energy Materials & Solar Cells*, 85, 13, 2005.
14. B. Geffroy, P. Le Roy, *Polymer International*, 55, 572, 2006.
15. C. Waldauf, M.C. Scharber, P. Schilinsky, J.A. Hauch, C.J. Brabec, *Journal of Appl. Phys.*, 99, 104503, 2006.
16. C.J. Brabec, S.E. Shaheen, C. Winder, N.S Sariciftci, P. Denk, *Appl. Phys. Lett.*, 80, 1288, 2002.
17. C.J. Brabec, A. Cravino, D. Meissner, N.S. Sariciftci, T. Fromherz, M.T. Rispens, L. Sanchez, J.C. Hummelen, *Adv. Funct. Mater.*, 11, 374, 2001.
18. J. Liu, Y.J. Shi, Y. Yang. *Solvation. Adv. Funct. Mater.*, 11, 420, 2001.
19. H. Frohne, S.E. Shaheen, C.J. Brabec, D.C. Muller, N.S Sariciftci, K. Meerholz, *Chem. Phys. Chem.*, 3, 795, 2002.
20. A. Gadisa, M. Svensson, M.R. Andersson, O. Inganas., *Appl. Phys. Lett.*, 84, 1609, 2004.
21. M.C. Scharber, D. Muhlbacher, M. Koppe, P. Denk, C. Waldauf, A.J. Heeger, C.J. Brabec, *Adv. Mater.*, 18, 789, 2006.
22. J.J.M. Halls, K. Pichler, R.H. Friend, S.C. Moratti, A.B. Holmes. *Appl. Phys. Lett.*, 68, 3120, 1996.
23. N. Marks, J.J.M. Halls, D.D.C. Bradley, R.H. Friend, A.B. Holmes., *Journal of Physics-Condensed Matter*, 6, 1379, 1994.
24. C.W. Tang, *Appl. Phys. Lett.*, *48*, 183, 1986.
25. J.J.M. Halls, C.A. Walsh, N.C. Greenham, E.A. Marseglia, R.H. Friend, S.C. Moratti, A.B. Holmes, *Nature*, 376, 498, 1995.
26. P. Peumans, A. Yakimov, S.R. Forrest, *J. Appl. Phys.*, 93, 3693, 2003.
27. M. Pope, C.E. Swenberg, *Electronic Processes in Organic Crystals and Polymers*; Oxford University Press: New York, 1999.
28. I.G. Hill, A. Kahn, Z.G. Soos, R.A. Pascal, *Chem. Phys. Lett.*, 327, 181, 2000.
29. M. Chandross, S. Mazumdar, S. Jeglinski, X. Wei, Z.V. Vardeny, E.W. Kwock, T.M. Miller, *Phys. Rev. B*, 50, 14702, 1994.

30. S.E. Shaheen, C.J. Brabec, N.S. Sariciftci, F. Padinger, T. Fromherz, J.C. Hummelen, *Appl. Phys. Lett.*, 78, 841, 2001.
31. W.L. Ma, C.Y. Yang, X. Gong, K. Lee, A.J. Heeger, *Adv. Funct. Mater.*, 15, 1617, 2005.
32. G. Li, V. Shrotriya, J.S. Huang, Y. Yao, T. Moriarty, K. Emery, Y. Yang, *Nat. Mater.*, 4, 864, 2005.
33. J. Peet, J.Y. Kim, N.E. Coates, W.L. Ma, D. Moses, A.J. Heeger, G.C. Bazan, *Nat. Mater.*, 6, 497, 2007.
34. H.Y. Chen, J.H. Hou, S.Q. Zhang, Y.Y. Liang, G.W. Yang, Y. Yang, L.P. Yu, Y. Wu, G. Li, *Nat. Photon.*, 3, 649, 2009.
35. S.R. Forrest, *Chem. Rev.*, 97, 1793, 1997.
36. A. Yakimov, S.R. Forrest, *Appl. Phys. Lett.*, 80, 1667, 2002.
37. J. Xue, B.P. Rand, S. Uchida, S.R. Forrest, *Adv. Mater.*, 17, 66, 2005.
38. J. Xue, B.P. Rand, S. Uchida, S.R. Forrest, *J. Appl. Phys.*, 98, 124903, 2005.
39. R. Koeppe, N.S. Sariciftci, *Photochem. Photobiol. Sci*., 5, 1122, 2006.
40. Photoinduced Electron Transfer (Eds.: M. A. Fox, M. Chanon), Elsevier, Amsterdam, 1988.
41. M.M. Wienk, J.M. Kroon, W.J.H. Verhees, J. Knol, J.C. Hummelen, P.A. van Hall, R.A.J. Janssen, *Angew. Chem. Int. Ed.,* 42**,** 3371, 2003.
42. M.T. Rispens, A. Meetsma, R. Rittberger, C.J. Brabec, N.S. Sariciftci, J.C. Hummelen, *Chem. Commun.,* 17**,** 2116, 2003.
43. J.J.M. Halls, A.C. Arias, J.D. MacKenzie, W. Wu, M. Inbasekaran, E.P. Woo, R.H. Friend, *Adv. Mater.,* 12, 498, 2000.
44. T. Martens, Z. Beelen, J. D'Haen, T. Munters, L. Goris, J. Manca, M. D'Olieslaeger, D. Vanderzande, L.D. Schepper, R. Andriessen, In *Organic Photovoltaics III,* edited by Z.H. Kafafi, D. Fichou, Proceedings of SPIE Vol. 4801 (SPIE, Bellingham, WA, 2003), 40.
45. A.C. Arias, N. Corcoran, M. Banach, R.H. Friend, J.D. MacKenzie, W.T.S. Huck, *Appl. Phys. Lett.,* 80**,** 1695, 2002.
46. F. Padinger, R.S. Rittberger, N.S. Sariciftci, *Adv. Funct. Mater.,* 13**,** 1, 2003.
47. J.J. Dittmer, R. Lazzaroni, P. Leclere, P. Moretti, M. Granström, K. Petritsch, E.A. Marseglia, R.H. Friend, J.L. Bredas, H. Rost, A.B. Holmes, *Sol. Energy Mater. Sol. Cells,* 61**,** 53, 2000.
48. J.J. Dittmer, E.A. Marseglia, R.H. Friend, *Adv. Mater.,* 12**,** 1270, 2000.
49. L. Schmidt-Mende, A. Fechtenkotter, K. Müllen, E. Moons, R.H. Friend, J.D. MacKenzie, *Science,* 293**,** 1119, 2001.
50. N. Camaioni, G. Ridolfi, G. Casalbore-Miceli, G. Possamai, M. Maggini, *Adv. Mater.,* 14**,** 1735, 2002.
51. H. Hoppe, M. Niggemann, C. Winder, J. Kraut, R. Hiesgen, A. Hinsch, D. Meissner, N.S. Sariciftci, *Adv. Funct. Mater.,*14, 1005, 2004.
52. T. Martens, J. D'Haen, T. Munters, Z. Beelen, L. Goris, J. Manca, M. D'Olieslaeger, D. Vanderzande, L.D. Schepper, R. Andriessen, *Synth. Met.,* 138**,** 243, 2003.
53. H.J. Snaith, A.C. Arias, A.C. Morteani, C. Silva, R.H. Friend, *Nano Lett.* 2, 1353, 2003.
54. M. Svensson, F. Zhang, S.C. Veenstra, W.J.H. Verhees, J.C. Hummelen, J.M. Kroon, O. Inganäs, M.R. Andersson, *Adv. Mater.,* 15, 988, 2003.
55. A.J. Mozer, P. Denk, M.C. Scharber, H. Neugebauer, N.S. Sariciftci, P. Wagner, L. Lutsen, D. Vanderzande, *J. Phys. Chem. B*, 108, 5235, 2004.

56. M.S. Kim, B.G. Kim, J. Kim, *Appl. Mater. & Inter*., 1, 1264, 2009.
57. C.J. Barbec, S.E. Shaheen, C. Winder, N.S. Sariciftci, P. Denk, *Appl. Phys. Lett.,* 80, 1288, 2002.
58. http://www.pv-tech.org/news/
59. C. J. Brabec, S. Gowrisanker , J.J.M. Halls, D. Laird , S. Jia, S.P. Williams, *Adv. Mater*., 22, 3839, 2010.
60. B. Walker, A.B. Tamayo, X.D. Dang, P. Zalar, J.H. Seo, A. Garcia, M. Tantiwiwat, T.Q. Nguyen, *Adv. Funct. Mater*., 19, 3063, 2009.
61. G. Li, V. Shrotriya, J. Huang, Y. Yao, T. Moriarty, K. Emery, Y. Yang, *Nat. Mater*., 4, 864, 2005.
62. W. Ma, C. Yang, X. Gong, K. Lee, A.J. Heeger, *Adv. Funct. Mater*., 15, 1617, 2005.
63. M.T. Lloyd, J.E. Anthony, G.G. Malliaras, *Mater. Today,* 10, 34, 2007.
64. J. Roncali, *Acc. Chem. Res*., 42, 1719, 2009.
65. J. Zhou, X. Wan, Y. Liu, G. Long, F. Wang, Z. Li, Y. Zuo, C. Li, Y. Chen, *Chem. Mater*. 23, 4666, 2011.
66. B. Walker, C. Kim, T.Q. Nguyen, *Chem. Mater.,* 23, 470, 2011.

Chapter 5

COLUMNAR MESOPHASE: MATERIALS AND METHODS

This chapter will review the materials used in the studied OPV devices and it will describe the experimental set-up built in order to characterize their most important features, including external and internal quantum efficiency.

5.1 Materials

All materials used in organic photovoltaics devices can be roughly divided into donors and acceptors. As described in chapter 4, donor and acceptor materials must be combined in a device structure to allow excitons to be separated and then the resulting charges to be transported to the electrodes. As the electrons travel through the acceptor material and the holes through the donor material, acceptor and donor can also be termed electron transport and hole transport materials, respectively.

In the following, the materials used to obtain bulk heterojunction (BHJ) structures based on low molecular weight (LMW) donors, with fullerene derivatives (such as $PC_{61}BM$ and $PC_{71}BM$) as acceptors, will be illustrated.

5.1.1 Photoconducting donors

The photoconductor chosen in order to be used in BHJ is a cyclopalladated Nile Red complex (***"complex 1"***). It belongs to a new class of photoconductors [1] and was used to with $PC_{61}BM$ as an acceptor. Complex **1** was synthesised in the Chemistry Department of the University of Calabria through a two steps procedure which involves the formation, by reaction of Nile Red with $Pd(OAc)_2$, of the acetato-bridged dimer **I,** [2] followed by its rupture upon addition of the Schiff base ligand, as illustrated in Fig. 5.1.

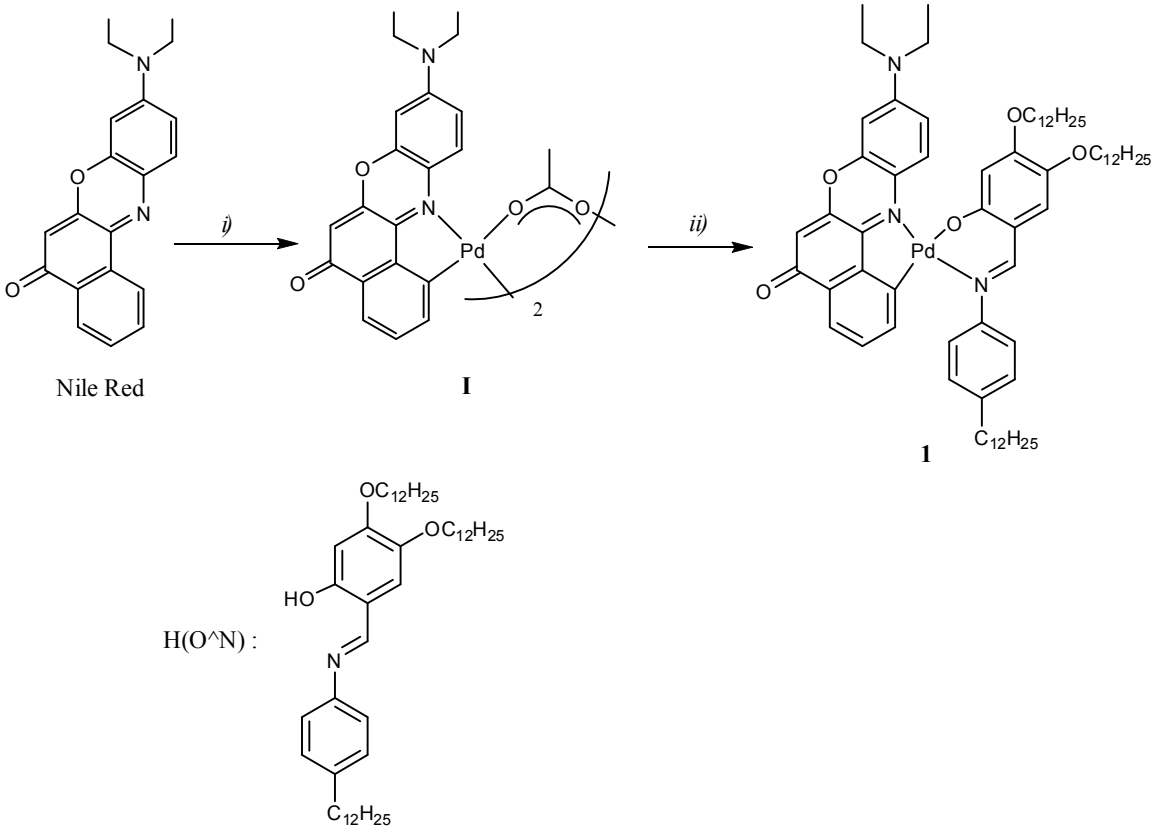

Figure 5.1: Reagents and Experimental Conditions: i) $Pd(OAc)_2$, Acetic Acid, 55ºC, 4h, ii) H(O^N), Ethanol, reflux, 2 days.

The required Schiff base **H(O^N)** has been quantitatively obtained by condensation of 4-dodecylaniline with 4,5-bis(dodecyloxy)-2-hydroxybenzaldehyde in refluxed ethanol.

The chemical structure of the fullerene derivatives, $PC_{61}BM$ and $PC_{71}BM$ used during the experiments are shown in Fig. 5.2.

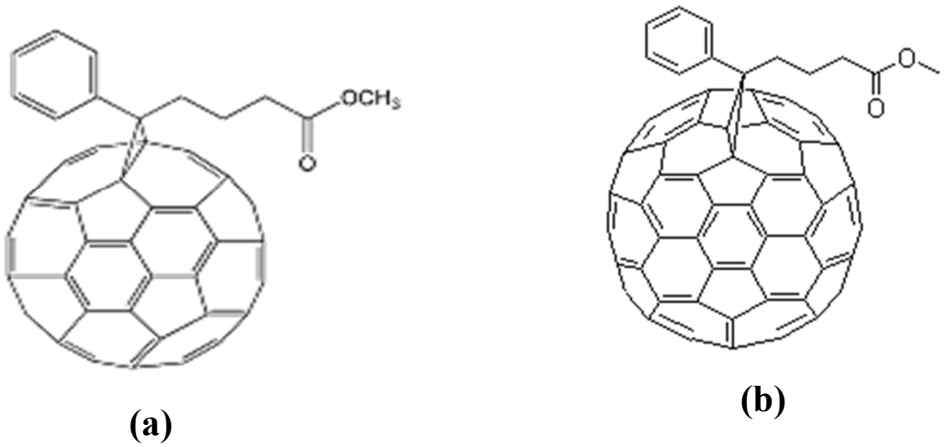

Figure 5.2. Chemical structure of (a) $PC_{61}BM$ and (b) $PC_{71}BM$

5.1.2 Hydrazonic donors

Two new hydrazonic donors for the preparation of bulk heterojunction solar cells were tested, in combination with fullerene derivatives, $PC_{61}BM$ or $PC_{71}BM$, as acceptors. The chemical structure of donors **2** and **3** is shown in Fig. 5.33a,b. Their HOMO and LUMO levels match well enough those of the fullerene derivatives.

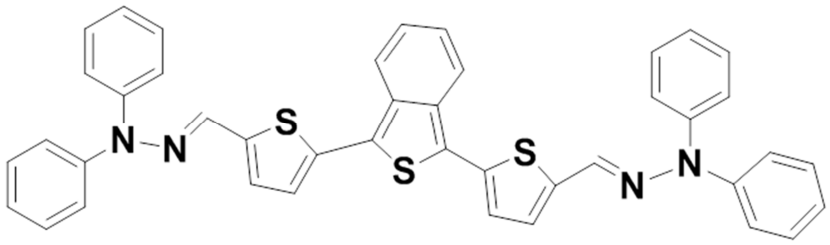

(a) **HOMO - 5.25**
LUMO -2.90

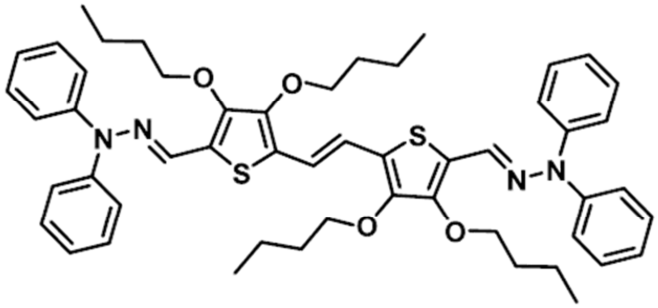

HOMO - 5.08
(b) **LUMO -2.57**

Figure 5.3. Chemical structure of (a) compound **2** and (b) compound **3**

In the subsequent subsections the development of the experimental set up for the photovoltaic characterization will be discussed.

5.2 The Sun

The sun is a source of luminous energy with an essentially constant power output. From this point of view, it is an excellent light source when testing the power conversion efficiency of a device and it is of course also the real source of light energy against which one has to measure the efficiency of a given device when it comes to energy production using a device in a real application. As practice would have it, the incident intensity of sunlight at the surface of the earth is, in many regions, highly variable and depends on the

weather (cloud cover, rain, snow, etc.), the time of the day (day, night), and the time of the year (summer, winter). For this reason it is practical to have a light source that can be used inside the laboratory, such that measurements can be carried out repeatedly at any point in time. The spectral distribution of the sunlight follows blackbody radiation from a source with the surface temperature of the sun (5800 K). In space, the distribution is continuous and near perfect, while at the surface of the earth various atmospheric gases absorb part of the spectrum giving it a particular spectrum, depending on where you are on the globe. The light sources that are available in the lab are exclusively electric arc lamps. For this reason the spectrum of simulated sunlight cannot exactly reproduce the spectrum of the sun. Generally, there is a tendency to have too much ultraviolet and visible light intensity and too little infrared light intensity. Furthermore, the spectrum often has discrete emission lines from the elements present in the arc lamp. In practice, different filters are employed and this can significantly improve on the resemblance to the solar spectrum.

5.3 Air mass (AM)

The spectrum of the sunlight changes as it is transmitted through the earth's atmosphere, as shown in Fig. 5.4. Aside from the transmission loss, there is selective absorption in certain wavelength regions by atmospheric gases. The amount of atmosphere that the light has to pass before reaching the surface of the earth is described as the air mass (AM). The spectrum obtained after passage through a certain air mass is often described by the abbreviation AM followed by a numeric figure that, in essence, indicates how much air mass the sunlight has been transmitted through. In space, just outside the earth's atmosphere, the spectrum of the sun is virtually undisturbed since it has not passed through any atmosphere but mostly empty space. The solar constant there is 1366.1 W m^{-2} and the spectrum is termed AM 0 according to the ASTM E490-00 standard. The shortest distance light can travel through the atmosphere to reach the surface of the earth is at the equator. There, the sun's spectrum is termed AM 1.0. At higher latitudes the sunlight has to travel longer distances through the atmosphere to reach the surface, so that the common air mass standard is termed AM 1.5, which corresponds to a receiving surface tilted 37° toward the equator. Alternatively, it can be viewed as a receiving surface where the sun has an elevation of 48.2° at zenith, as shown in Fig. 5.5.

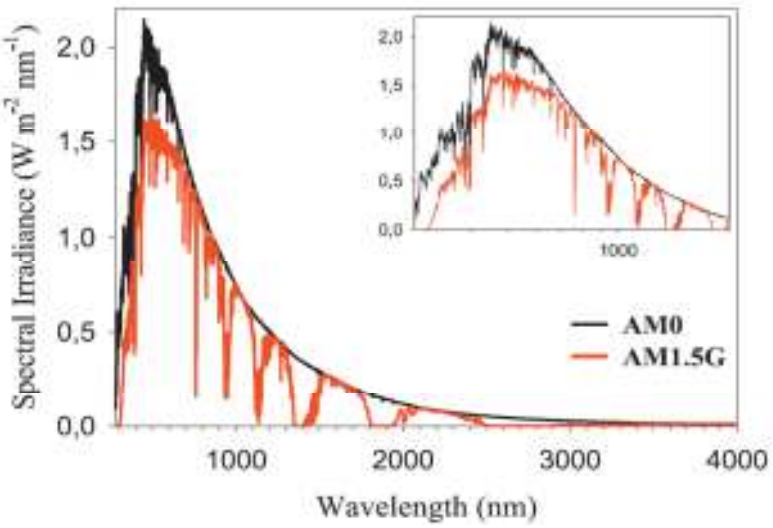

Figure 5.4: Comparing the sun spectrum in space just outside the earth's atmosphere (AM 0) and the sun's spectrum as received at the surface of the earth AM 1.5G. The inset shows the spectrum up to 2000 nm on a logarithmic scale.

Apart from the transmission loss through the atmosphere due to scattering, there are some distinct bands due to absorption mainly by oxygen, ozone, water, and carbon dioxide in the atmosphere. Ozone absorbs efficiently in the ultraviolet region and water absorbs at 940 nm and at 1130 nm. Both water and carbon dioxide absorb at 1400 nm, 1850 nm, and 2700 nm. Oxygen gives rise only to minor absorption bands.

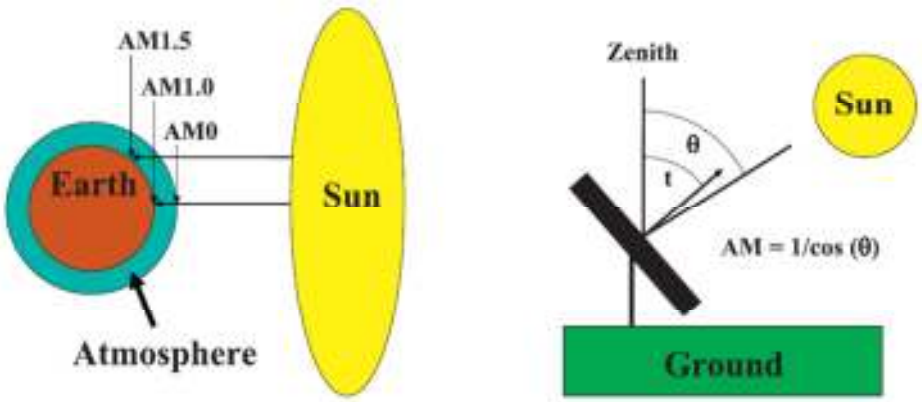

Figure 5.5: (a) Illustration of the air masses AM 0, AM 1.0 and AM 1.5. (b) Illustration of the receiving surface for the solar cell along with a calculation of the air mass. The normal of the receiving surface is tilted by an angle, t, towards the equator. The angle between the ground normal and the sun at zenith, θ, is used to calculate the air mass as the inverse of cos(θ). For AM 1.5 the tilt angle t = 37° and the zenith angle θ = 48.2°.

5.3.1 The AM 1.5D (or Simply AM 1.5) versus the AM 1.5G spectrum

Data on the emission from the sun can be downloaded from National Renewable Energy Laboratory (NREL) in Colorado, U.S., and are contained in the standard tables for solar spectral irradiance[3]. The AM 1.5 spectrum is also called the AM 1.5D spectrum where D stand for the direct, and circumsolar is the spectrum obtained when viewing the sun through a circular aperture with an opening angle of 5.8 degree (the sun being at the center of the aperture). AM 1.5D is the easiest solar spectrum to obtain reproducibly. The sunlight that is received through such an aperture includes the irradiance from the solar disk plus irradiation from the corona. The total power contained in this spectrum, obtained by integration, amounts to 901 W m^{-2}. Thus, this is the power that a solar cell will receive per unit area when viewing the sun.

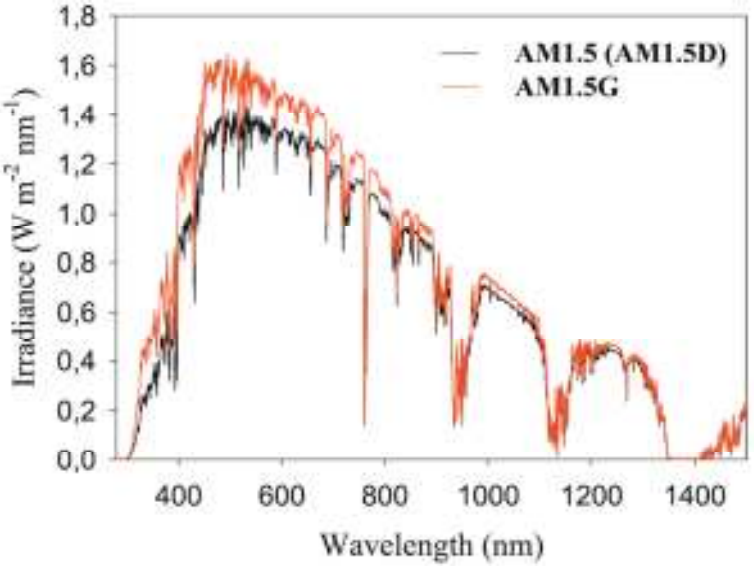

Figure 5.6. A comparison between the AM 1.5 (AM 1.5D) and the AM 1.5G spectra. The integral of the AM 1.5G is ~ 1000 W m^{-2} and includes contributions from diffusely scattered light and ground reflection from soil.

Furthermore, not all the available sunlight is received by the solar cell in this manner because there is a considerable amount of scattered and diffused light that can be harvested. From this point of view, a more practical setup is to use a viewing platform that faces south (for northern latitudes) and is tilted at an angle with respect to the surface of the earth at the viewing location. For AM 1.5, this angle is 37°. Such a surface receives the direct and circumsolar sunlight, but also reflection from the ground in front of the

viewing platform and diffusely scattered light from the truncated hemisphere above the viewing surface. Light from the sky dome to the north of the viewing platform is not received. The total power received at such a surface is 1002 W m^{-2} and is called AM 1.5G, where G stands for global. The larger amount of energy in the AM 1.5G spectrum is concentrated at shorter wavelengths (Fig. 5.6).

The reason for the higher concentration of photons at short wavelengths in the AM 1.5G spectrum is due to scattering of the light out of the direct beam by aerosols and gas molecules in the atmosphere. AM 1.5G also contains a contribution from ground reflection in front of the tilted viewing surface. From this point of view, AM 1.5G is the correct standard to use because it is what one would typically experience during an experiment on a tilted viewing surface, but it is not as rigorously defined as AM 1.5D since many components enter into the formation of it (surface albedo, aerosol depth, water vapor, ozone level, carbon dioxide, etc).

In our measurement setup we use a solar simulator of standard IEC 904-9/A, purchased from Sciencetech (Canada), model number SS150W. We used this solar simulator in order to obtain an AM 1.5G spectrum of the sun, using an AM1.5G filter in front of the collimated light of the simulator. A photograph of the solar simulator is shown in the I-V setup section. The important data for the solar simulator[4] model SS150W are summarized in Table 5.1

DATA	SS150W
Total output power on target	9W
Uniformity	Constant within 15% over specified area
Stability of power on target (Short term)	± 1% after 10 minutes
Stability of power on target	-20% (after 1000 hours)
(Long term-due to aging of the lamp)	
Wavelength control	Solar and Bandpass filters
Uniform area diameter	2” at 15” from edge of the solar simulator
Power density (W/m^2)	2350 W/m^2
(Without filters on 2” diameter target)	
Distance to target (typical range)	15”-35” from edge of the solar simulator
Standard/Class	IEC 904-9/A

Table 5.1. Data for the Sciencetech solar simulator model SS150W.

5.4 Calibration of a solar simulator

The performance of a solar cell is most commonly rated in terms of its efficiency with respect to standard reporting conditions (SRC) defined by temperature, spectral irradiance and total irradiance[5]. The SRC for rating the performance of a solar cells are 100 mW/cm^2 irradiance, AM 1.5G reference spectrum and 25 ^{0}C cell temperature [6-10].

The power conversion efficiency of a solar cell is given by

$$\boldsymbol{\eta = \frac{P_{max}}{E_{tot}A} \times 100} \quad (1)$$

where P_{max} is the measured peak power of the cell, A is the device area and E_{tot} is the total incident irradiance. In order to get an accurate value of efficiency, the value of E_{tot} must be measured. The irradiance incident on the PV cell is typically measured with a reference cell. For I-V measurements with respect to a reference spectrum, there is a spectral error between the reference spectrum standard and the solar simulator spectrum, which produces an error in the measured short circuit current of the photovoltaic cell. This error can be derived upon the assumption that the photocurrent is the integral of the product of cell responsivity and incident spectral irradiance and it can be expressed as a spectral mismatch correction factor (M) [11-12].

$$\boldsymbol{M = \frac{\int_{\lambda_1}^{\lambda_2} E_{Ref}(\lambda) S_R(\lambda) d\lambda}{\int_{\lambda_1}^{\lambda_2} E_{Ref}(\lambda) S_T(\lambda) d\lambda} \frac{\int_{\lambda_1}^{\lambda_2} E_S(\lambda) S_T(\lambda) d\lambda}{\int_{\lambda_1}^{\lambda_2} E_S(\lambda) S_R(\lambda) d\lambda}} \quad (2)$$

where $E_{Ref}(\lambda)$ is the reference spectral irradiance, $E_S(\lambda)$ is the source spectral irradiance, $S_R(\lambda)$ is the spectral responsivity of the reference cell, and $S_T(\lambda)$ is the spectral responsivity of the test cell, each as a function of wavelength (λ). The limits of integration λ_1 and λ_2 in the above equation should encompass the range of the reference cell and the test-device spectral responses, and the simulator and reference spectra should encompass λ_1 and λ_2 to avoid error[13]. A matched PV reference cell is typically used as the reference detector and a solar simulator is used as the light source to minimize the deviation of M from unity. Only the normalized values and not the absolute of $E_S(\lambda)$, $S_R(\lambda)$, and $S_T(\lambda)$ need to be measured for Equation 2. Equation 2 is valid for any thermal or PV detector or light source, provided none of the integrals are zero. In the extreme case of a laser as the light source and a thermal detector with a wavelength-independent responsivity, the uncertainty in M is dominated by the uncertainty in the spectral responsivity.

The total effective irradiance of the light source (E_{eff}), which is the total irradiance seen by the cell, can be determined from the short-circuit current of the reference cell under the source spectrum ($I^{R,S}$) from the equation:

$$\boldsymbol{E_{eff} = \frac{I^{R,S}M}{CN}} \tag{3}$$

where *CN* is the calibration number (in units of A W^{-1} m^2) for the instrument used to measure the incident irradiance. E_{eff} is different from E_{tot} in Eq. (1), since E_{tot} usually refers to the total irradiance integrated over the entire spectrum, and not just the part of the spectrum the cell responds to. Both *E*eff and *E*tot are derived from integrating $E_S(\lambda)$ over an appropriate range of wavelength. The short-circuit current of a test cell ($I^{T,R}$) at the reference total irradiance (E_{Ref}) is given as: [5,13]

$$\boldsymbol{I^{T,R} = \frac{I^{T,S}E_{Ref}CN}{I^{R,S}M}} \tag{4}$$

where $I^{T,S}$ is the short-circuit current of a test cell measured under the source spectrum. Once *M* is known, the simulator is adjusted so that E_{eff} is equal to E_{Ref}, or

$$\boldsymbol{I^{T,R} = \frac{I^{R,R}I^{T,S}}{I^{R,S}M}} \tag{5}$$

where $I^{R,R}$ is the calibrated short-circuit current of the reference cell under the reference spectrum and total irradiance. This is the standard simulator-based calibration procedure.

5.5 Spectral responsivity measurements

The calibration procedure described above requires the knowledge of *M* for a given light source and a given test-cell/reference-cell combination. This, in turn, requires the knowledge of spectral irradiance of the light source and of the spectral responsivities of the test and reference cells. The spectral responsivity, $S(\lambda)$, is calculated from the quantum efficiency, $QE(\lambda)$, by[5]

$$\boldsymbol{S(\lambda) = \frac{q\lambda}{hc}QE(\lambda)} \tag{6}$$

where the constant term q/hc equals 8.0655×10^5 for wavelengths in units of meters and $S(\lambda)$ in units of AW^{-1}. The term $QE(\lambda)$ is basically the number of electron–hole pairs generated per incident photon in the device multiplied by 100.

In our case, to calibrate our solar simulator we used a calibrated Hamamatsu Si diode (model S2386-44K). The spectral response of the S2386-44K diode is shown in Fig. 5.7. As for silicon diodes M ~ 1, in our calibration of the solar simulator the value of M was assumed to be 1[14-15].

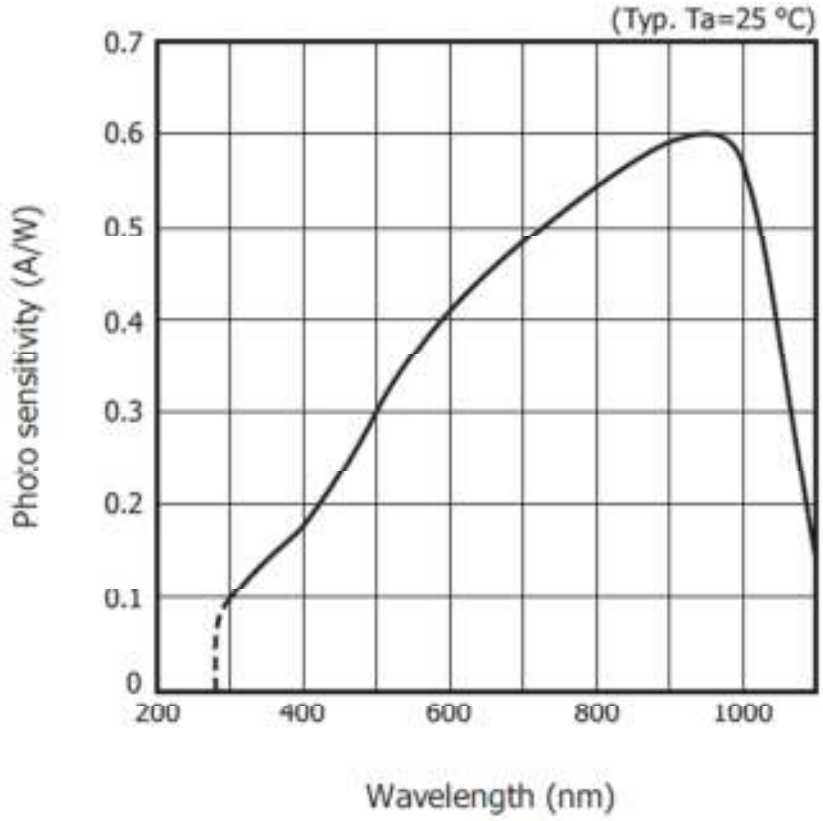

Figure 5.7: Photosensitivity of the Hamamatsu Si diode (S2386-44K) as a function of wavelength, used for solar simulator calibration.

5.6 Current-Voltage (I-V) Characteristics and Solar Cell Parameters

Current/voltage characteristics were measured (Keithley 2400 Source Meter) inside a N_2 glove box under simulated solar illumination (Sciencetech, Model SS150 solar simulator, Air Mass 1.5G, 100 mW/cm^2). The solar simulator intensity was tuned by using a calibrated Si photodiode (Hamamatsu S2386-44K).

From the J/V curves (as shown in Fig. 5.8a) it is possible to extract the efficiency of devices. The power conversion efficiency η is defined by

$$\eta = \boldsymbol{FF}\frac{\boldsymbol{J_{sc}V_{oc}}}{\boldsymbol{I}} \tag{7}$$

Where I is light intensity, Jsc is the measured short circuit current density, V_{oc} is the open circuit voltage and FF is the fill factor. The FF is defined considering the maximum power P_{max} (obtained from characteristic curves) as:

$$\boldsymbol{FF} = \frac{\boldsymbol{P_{max}}}{\boldsymbol{J_{sc}V_{oc}}} = \frac{\boldsymbol{I_{max}V_{max}}}{\boldsymbol{J_{sc}V_{oc}}} \tag{8}$$

Fig. 8 b, shows typical curves obtained during measurements.

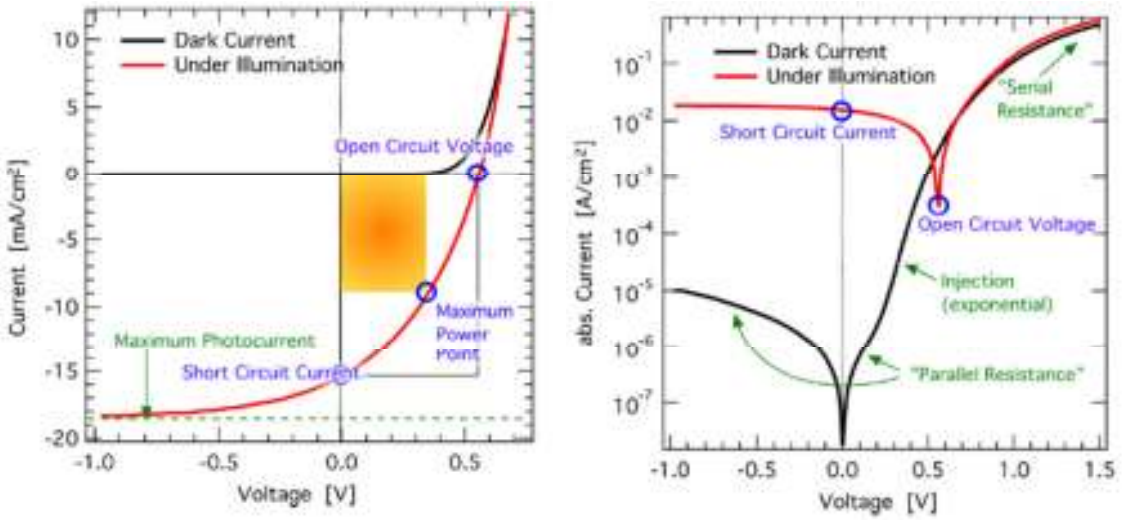

(a) **(b)**

Figure 5.8: Typical J/V curves for a solar cell and (a) a linear and (b) logaritmic scale. Dark current in black and curves obtained under illumination in red.

5.7 Current-Voltage (I-V) characteristics, set-up

The schematics of the experimental set up for the photovoltaic I/V characterization is illustrated in the Fig. 9 a, whereas in Fig. 9 b a picture of the actual set up is shown. When the solar simulator is switched on, stabilized and calibrated, the experimenter is ready to conduct measurements on devices. The most common method for characterization involves recording the electrical response of the OPV device in the dark and under illumination. The electrical response is measured using a source-measure unit (SMU), also called a source meter. The source meter has the capacity to apply a voltage to a two-terminal device under test (DUT), such as a solar cell, and measure the current. In usual practice, the voltage is applied and the current is measured. The reason for this lies in the fundamental nature of the OPV device, which is a thin film. It is rather unpredictable what current range a given device will respond in and the passage of a

particular current set by the experimenter may require unrealistic voltages, leading to breakdown and destruction of the device. Therefore, it is almost exclusively the voltage that is swept. Typical voltage ranges for devices measured are from − 1.5 V to + 1.5 V.

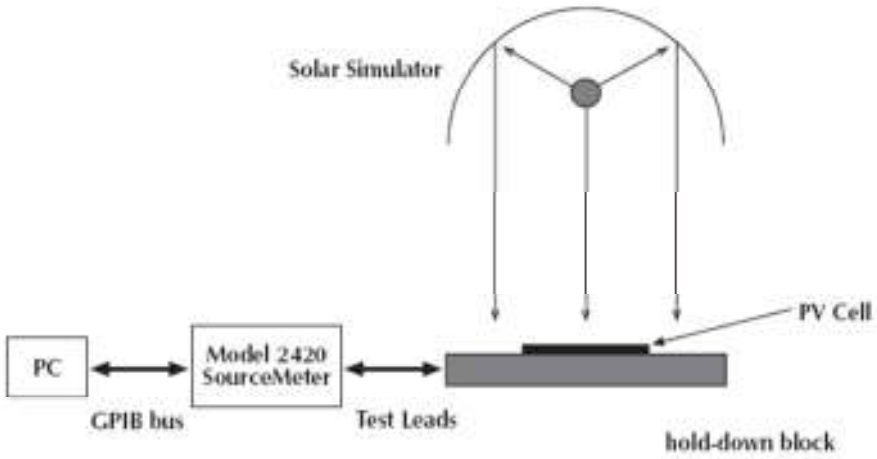

(a)

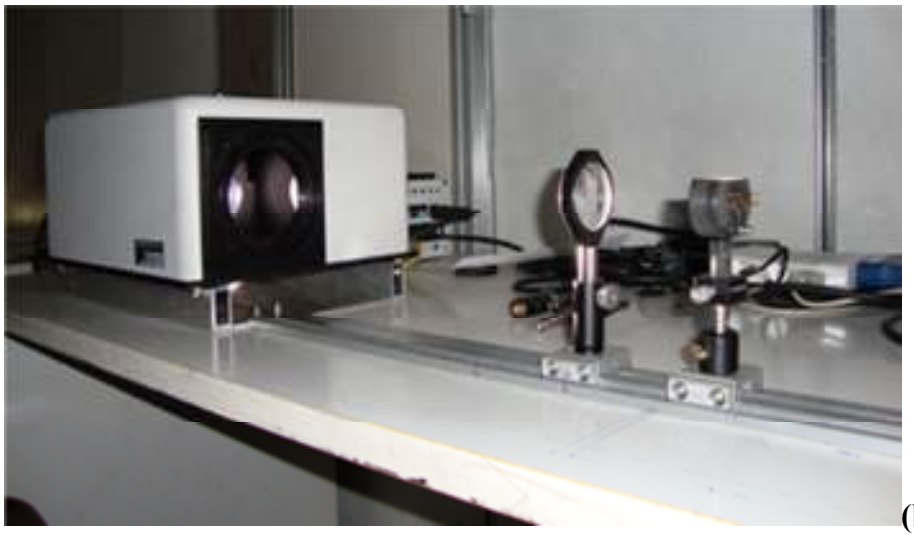

(b)

Figure 5.9: (a) Schematic of the I/V characteristic setup, (b) actual set up used for I/V characterization.

The front view of the program in LABView to acquire the I-V curve parameters is shown in the Fig. 5.10. With the help of this block diagram the user can set the parameters such as sweep voltage, sweep direction, sample area, input optical power etc and at the end of the execution of the program all the related I-V cure parameters are calculated and displayed along with the curve in the IV quadrant according to the virtual instrument libraries which are necessary in order to interface one or more instruments using LABview.

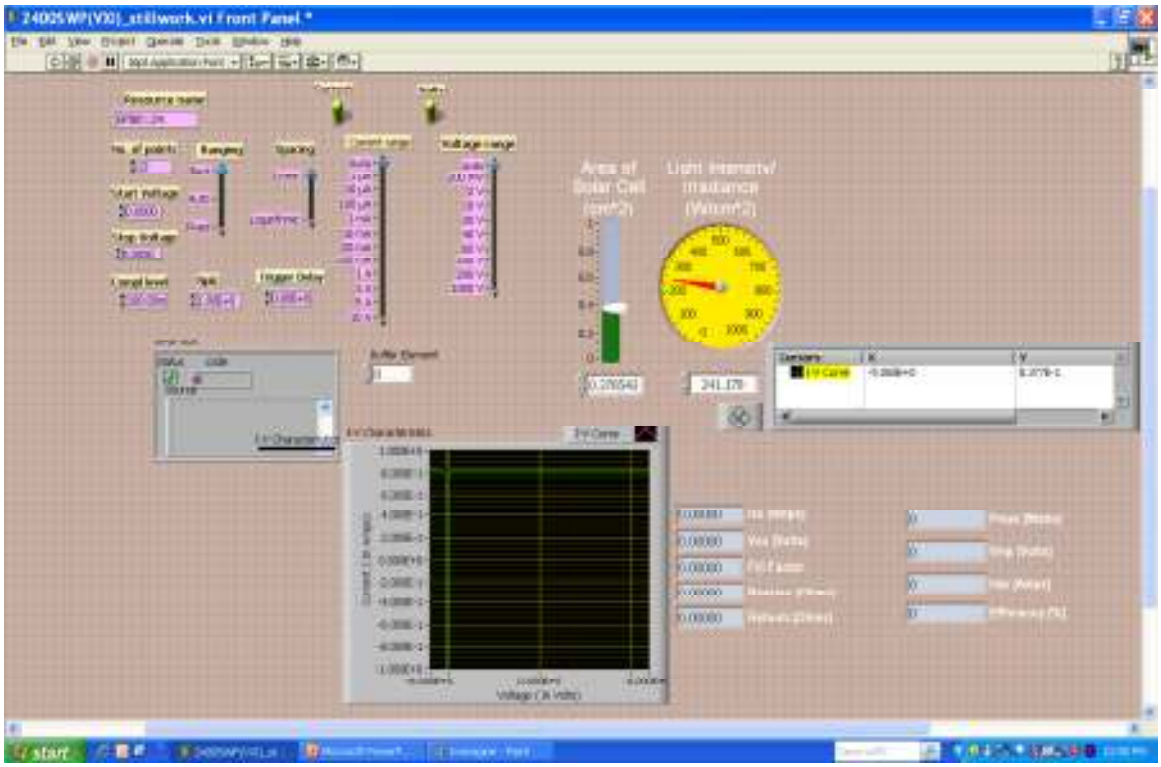

Figure 5.10: Front panel view of data acquisition program to acquire I/V curve parameters in LABView

The internal block diagram of the program is also shown in the Fig 11. In this window one can observe the exact execution of the sequences which occur when the program runs and calculates the various parameters. In the internal block diagram there are 5 main sub virtual instrument (VI) programs which calculate:

1. Short circuit current (I_{sc}) and open circuit voltage (V_{oc})
2. Maximum power point (P_{max}) and corresponding V_{max} and I_{max}
3. Fill factor (FF)
4. Efficiency (η) of the device
5. Series resistance (R_s) and shunt resistance (R_{sh})

The internal block diagram of each sub VI are shown in Fig. 5.12.

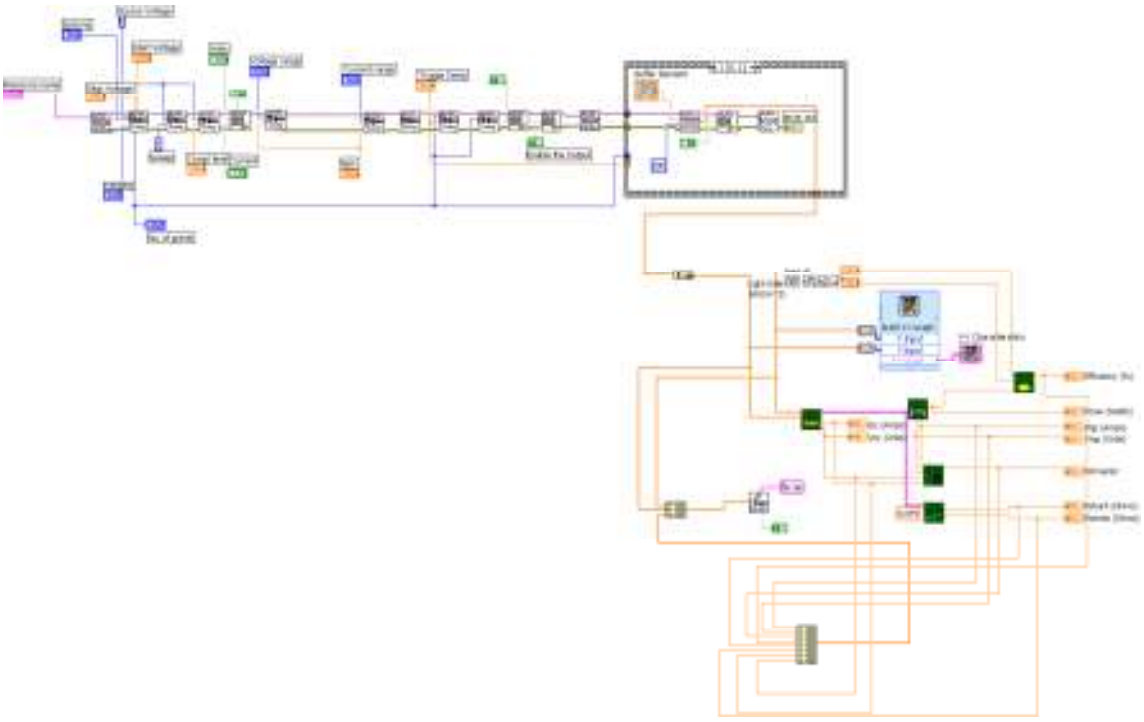

Figure 5.11: internal block diagram of data acquisition program to acquire I/V curve parameters in LABView

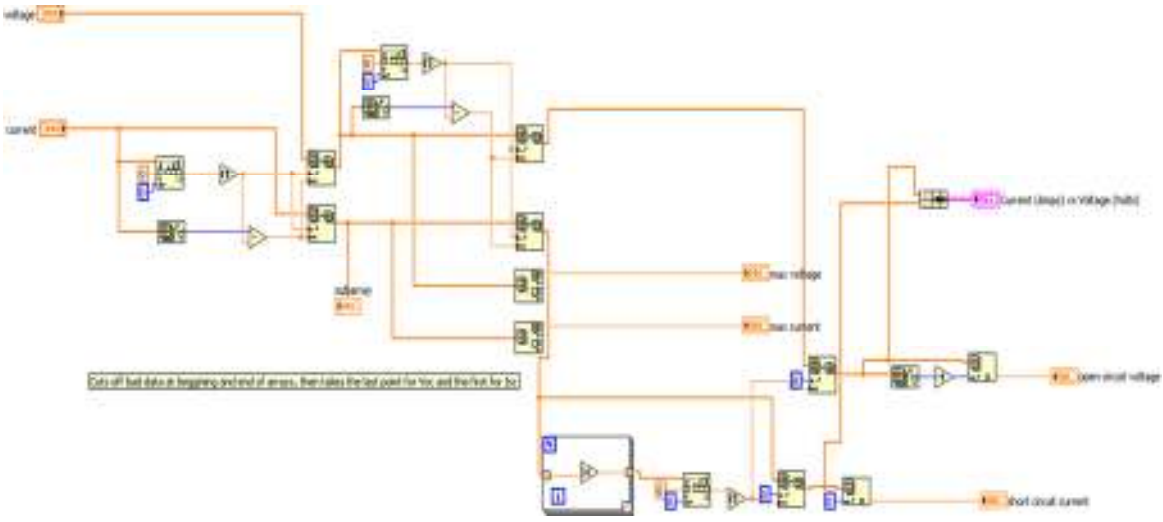

(1)

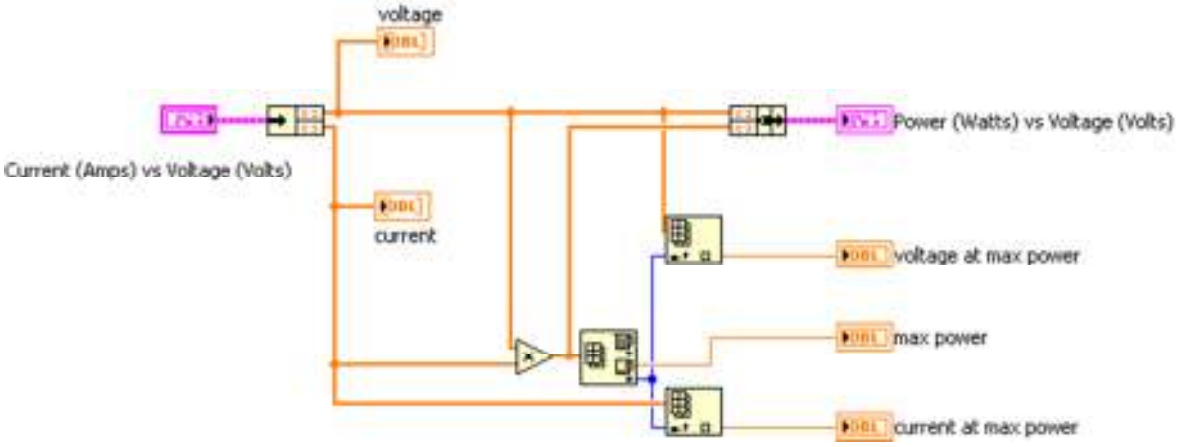
voltage
Power (Watts) vs Voltage (Volts)
Current (Amps) vs Voltage (Volts)
current
voltage at max power
max power
current at max power

(2)

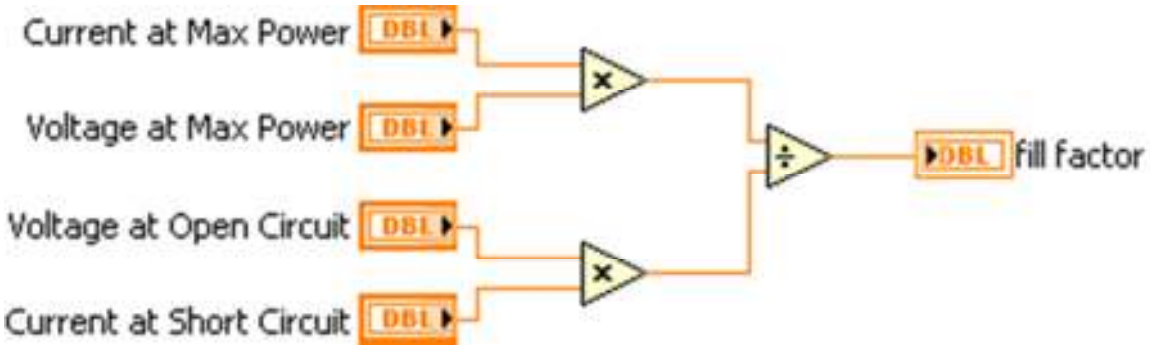
Current at Max Power
Voltage at Max Power
Voltage at Open Circuit
Current at Short Circuit
fill factor

(3)

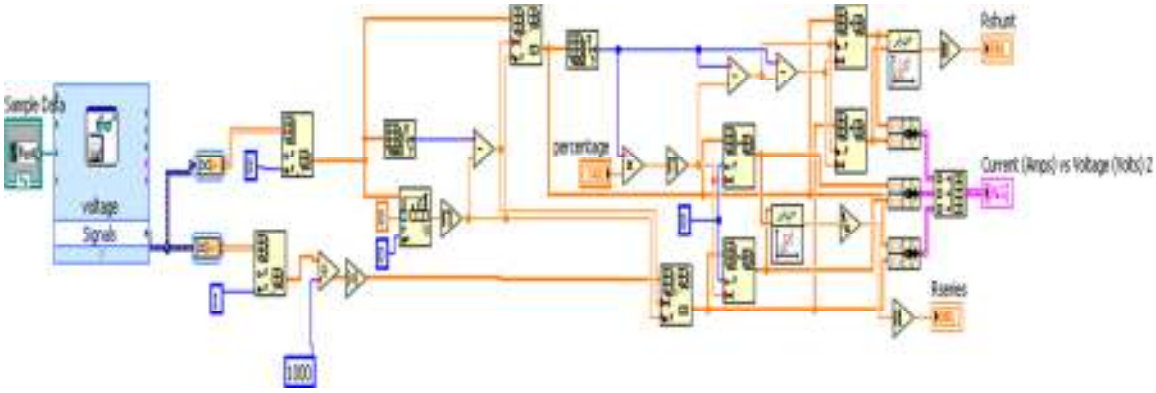

(4)

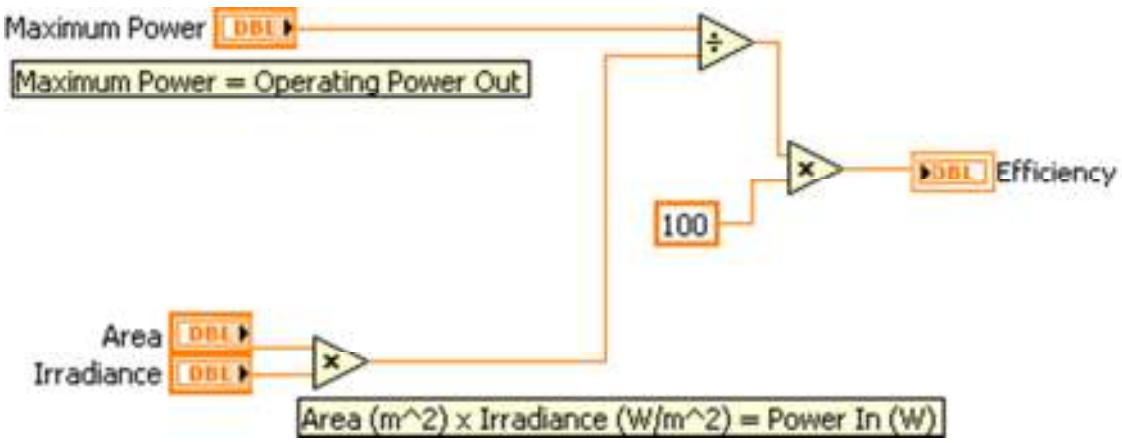

(5)

Figure 5.12: internal block diagram of data acquisition program to calculate (1) I_{sc} and V_{oc}, (2) P_{max} and corresponding V_{max} and $I_{max,}$ (3) Fill factor, (4) Efficiency (ŋ) and (5) R_s and R_{sh}

5.7.1 The source meter

There are many commercially available source meters for photovoltaic measurements but the most extensively (and almost exclusively) used source meter is the Keithley 2400 shown in Fig. 5.13. It has a tangible size and it is accurate and reliable. Furthermore, it has many possible means for interfacing to computers, such as a serial interface, an IEEE-488 interface, and an Ethernet port (IP address). It is possible to perform two-contact and four-contact measurements, but for most OPVs, two-contact measurements are performed. In our testing, the two contact method was used.

Figure 5.13. front and back view of the Keithley 2400 source measure unit.

5.7.2 Speed of IV-curve measurement, dielectric relaxation, and capacitive loading

The speed of recording the I-V-curve is, for small devices under ideal conditions, unimportant and the IV data can be recorded at arbitrary speeds and in arbitrary directions (i.e., −1.5 V → +1.5 V or +1.5 V → −1.5 V). When performing measurements on devices of larger areas, the capacitance of the device may influence the measurement. An OPV device is also a capacitor and it is charged by an amount of current that generates a charge that can be stored at the given voltage according to the capacitance. The impedence of the system determines how fast this process takes place and the time constant for this process is given by

$$\tau = RC \tag{9}$$

where τ is the time constant in seconds, R is the resistance through which the device has to charge/discharge in ohms, and C is the capacitance of the device in farads. Normally, the impedence of the source meter is large but many systems perform the measurement by subjecting the device under test to a low-impedance period for the purpose of charging /discharging; for such source meters this is not a problem. The impedance during measurement may be very high ($>10^9$ Ω). The capacitance for OPV devices depends on the thickness of the active layer. Typical values for a 100-nm thick device have relative dielectric constants, ε_r, for polymer blends of around 2–4, giving device capacitances of around 20–40 nF cm^{-2}. If the device has a low impedance due to shunts, there will not be any problem with capacitive charging. It can always be tested by recording IV-curves very slowly and very quickly in both sweep directions. The curves should be superimposable, but if they are not, the speed should be decreased. Another related effect that can take place is dielectric relaxation in the active layer of the materials. Especially soft, lossy dielectrics exhibit this behavior where the molecular dipoles are rearranged in response to the electric field. The process is indistinguishable from the capacitive charging/discharging effect except for the time dependence. The advice is to make sure that there is no dependence of the IV-curve on speed and direction.

5.7.3 Sample holder

The sample holder was designed in order to measure the I-V curve and external quantum efficiency of four different areas in one sample, without disturbing the alignment

of the sample with respect to the solar simulator light. A slot was also provided in the sample holder to accommodate a filter in the case when a monochromator was used for external quantum efficiency measurements. This filter may be necessary to avoid illuminating the sample with the second harmonic light when using the monochromator above 550 nm. Fig. 5.14 shows the front and back view of the sample holder. The electrical contacts were made using spring loaded pins, which ensure a good contact and minimize damage to the aluminium cathode on the back side of the sample holder. A switching box using a rotatory switch was also prepared with proper electrical connections to ensure switching of the applied voltage, with minimum electrical noise, on the four samples.

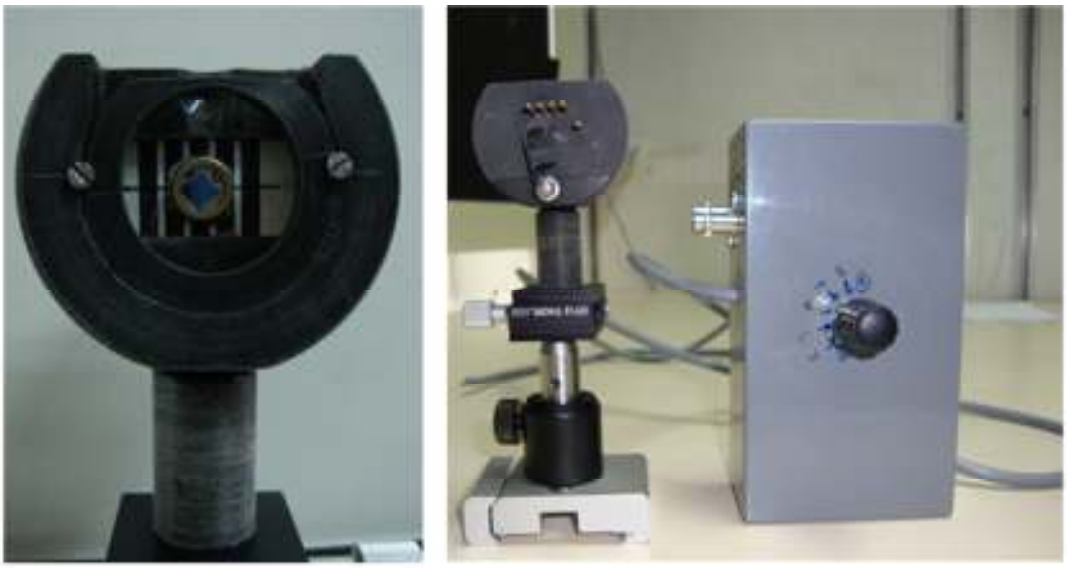

Figure 5.14: Front and back view of the sample holder along with the switching box.

5.8 External Quantum Efficiency Characterization (EQE)

External Quantum Efficiency gives the spectral response of the photovoltaic device. EQE measurement systems generally consist of a solar simulator, a monochromator, and a source meter. In order to develop this setup we purchased all the required instruments, which were then aligned on a metallic rail. The distances between the instruments and the height above the working plane were adjusted carefully, as shown in Fig 5.15. in order to obtain the best alignment and results.

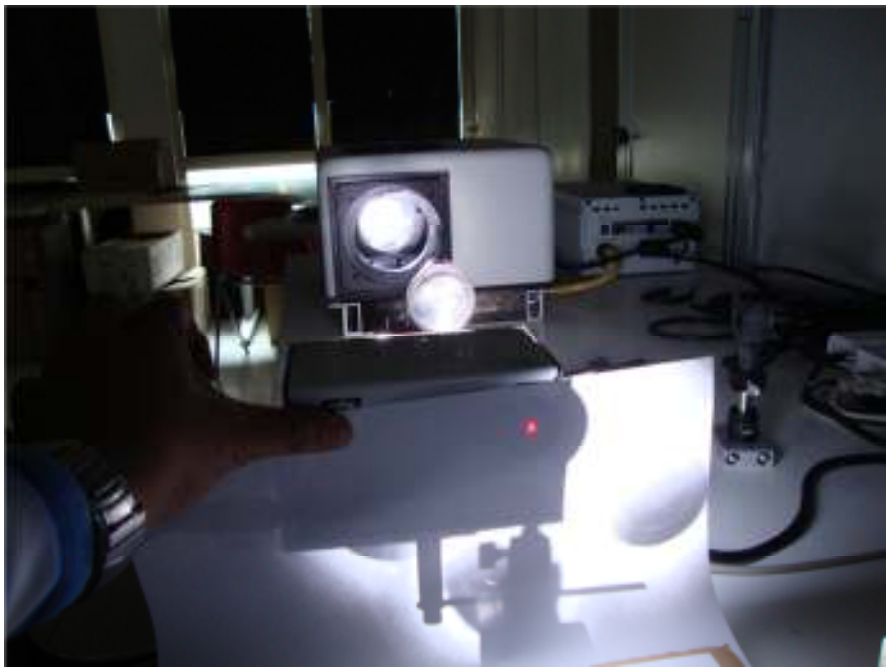

Figure 5.15: Experimental set-up for EQE characterization

For measuring EQE spectra, an AM 1.5G solar simulator provides the light. Photons with specific wavelengths are filtered out by a monochromator and then directed onto the OPV device to generate current at that particular wavelength in the absence of external bias voltage. The corresponding current can be read out using a Keithley 2400 source meter. The scanning wavelength is generally located within the absorption range of the active materials.

The data acquisition program was written by me in LABView. The corresponding front panel view and internal block diagram of the program are shown in Fig. 5.16.

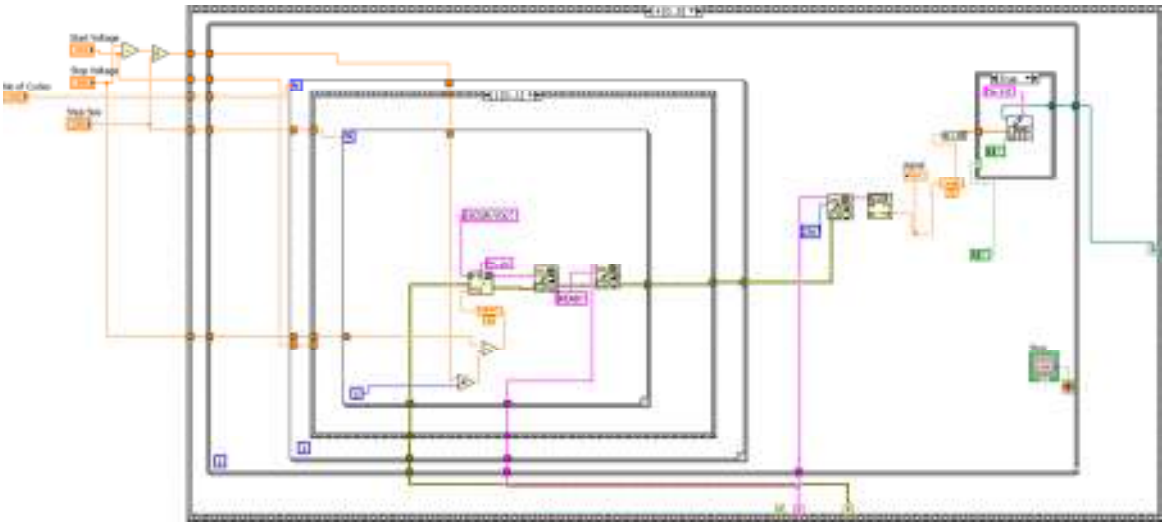

Figure 5.16: Front panel view (Blue/green) and internal block diagram of data acquisition program to acquire EQE in LABView.

The external quantum efficiency (EQE) is defined by the ratio between the number of charges N_e extracted at the electrode and the total number of photons N_{ph} incident on the device at a particular wavelength as:

$$\boldsymbol{EQE(\lambda) = \frac{N_e}{N_{ph}}} \tag{10}$$

In the experiment, the EQE(λ) was obtained by first measuring the photocurrent density of a calibrated Si photodiode J_{Si} and then the photocurrent density of the device J_D. EQE was calculated as:

$$\boldsymbol{EQE(\lambda) = QE_{Si}\frac{J_{Si}}{J_D}} \tag{11}$$

where QE_{Si} is the quantum efficiency of the calibrated Si photodiode.

5.9 Internal Quantum Efficiency Characterization (IQE)

The internal quantum efficiency (IQE) is defined by the ratio between the number of charges N_e extracted at the electrode and the total number of absorbed photons N_{ab} in the device at a particular wavelength. The internal quantum efficiency IQE was obtained as:

$$\boldsymbol{IQE(\lambda) = \frac{EQE(\lambda)}{(1-e^{\alpha d})}} \tag{12}$$

where α is the extinction coefficient of a device of thickness d. By knowing the EQE and α, IQE can be easily calculated for the device.

5.10 Absorption measurement (α)

Absorption spectra in the transmitted configuration were obtained using a Perkin Elmer 900 UV-Vis spectrophotometer.

In the absorption measurements a white light source is used (Xe-Arch Lamp), this light is passed through a monochromator, which is then divided into the two beams of equal intensity I_0. The one beam is called as the reference beam and the another one is allowed to pass through a sample of thickness d, then both the beams are collected at the suitable detectors and the intensities are measured. If the transmitted intensity of the detector 1 is I and that of detector 2 is I_0 (Reference beam) then according to Bear's law:

$$\boldsymbol{I = I_0 e^{-\alpha d}} \tag{13}$$

or $$\boldsymbol{\alpha = \frac{1}{d} ln\left(\frac{I}{I_0}\right)} \tag{14}$$

Where α is the absorption coefficient of the material

However, when the thickness of the sample is of the order of the wavelength used, the absorption measured using the transmittance technique is inaccurate due to interference effects. In such cases, for an accurate measurement of the absorption of the material, a reflection technique can be used. The setup for the absorption measurement with such technique is shown in Fig. 5.17. In this type of measurements the back of the sample is totally reflective, a property usually achieved by using an aluminium coating. Light at a particular wavelength, controlled by a monochromator is reflected by the sample. The intensity of the reflected light (I) is measured by using a detector and compared with the light intensity reflected by a blank (I_0). The absorption coefficient of the material will be given by:

$$\boldsymbol{\alpha = \frac{1}{2d.cos\theta} ln\left(\frac{I}{I_0}\right)} \tag{15}$$

where is 2θ is the angle between the incident and reflected light.

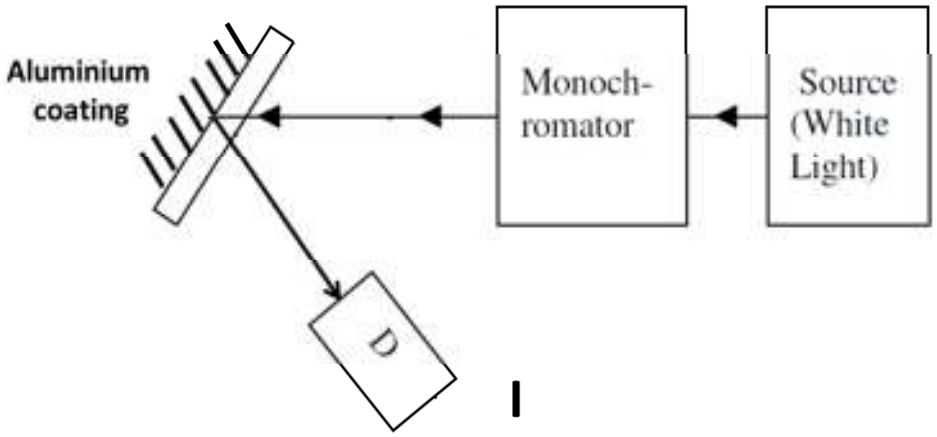

Figure 5.17: Schematic of the absorption measurement by reflection method.

5.11 Sample preparation

Samples for photovoltaics cells were prepared on ITO coated (UNAXIS, 110 nm ITO thickness, sheet resistivity 12 Ω/cm^2) glasses as anode. For the other electrode (cathode) a different combination of Al or LiF/Al and Ca/Al was used, depending upon the active materials combination. The different steps involved in complete sample preparation are discussed in the following.

5.11.1 The substrate

Photo-lithographically patterned ITO glasses (The photolithographic process is described in detail in Chapter 2) were obtained using the mask shown in Fig. 5.18.

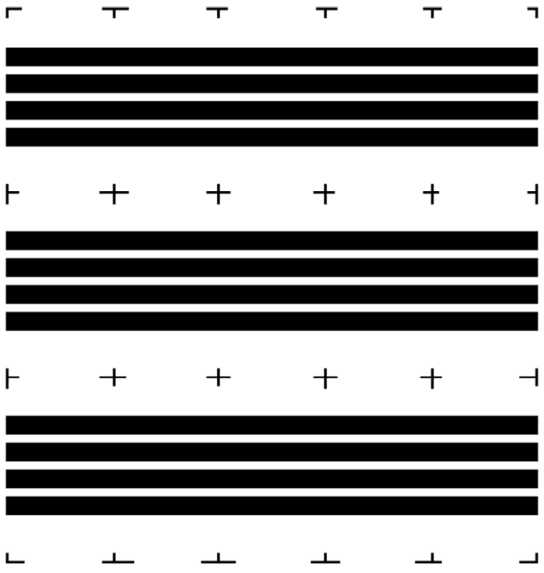

Figure 5.18. Mask used during photolithography to obtain ITO electrodes for photovoltaic cells.

The samples were then successively cleaned in an ultra-sonicator using distilled water (DW) with soap, DW, acetone and isopropyl alcohol. The cleaned substrates were dried in a vacuum oven at 90 ^{0}C overnight. A treatment with air plasma (Diener Electronics, Model Femto) was then performed at 100% power for 5 minutes and 30 seconds before applying the PEDOT:PSS layer, in order to lower the ITO work function.

5.11.2 The PEDOT:PSS layer

It is common practice to interpose a layer of a hole conducting material between the anode and the active layer, in order to improve the surface roughness of the substrate and to stabilize the electrical contact between ITO and the active layer. We used Poly(3,4-ethylenedioxythiophene) poly(styrenesulfonate) (PEDOT:PSS, CLEVIOS P VP 4081, H.C. Starck), with a chemical structure shown in Fig. 19. It is possible to make devices without PEDOT:PSS if none is available. However, in this case the efficiency will be lower.

PEDOT:PSS is best applied by spin coating (CaLCTec instruments, Model Fr10KPA-HC). The patterned substrate is placed in the spin coater with the ITO slide facing up. The spin coating of PEDOT:PSS dispersion (typically 1.3% wt./V) has to be performed at high speed; 2000–5000 rpm gives a very thin homogenous layer. Depending on the spinning rate one can obtain thicknesses ranging from 20 nm to 60 nm. Spinning has to be continued for a few minutes because the dispersion dries slowly. The application of the PEDOT:PSS dispersion can be done with a pipette or with a plastic syringe through a micro filter (in our case we used a 0.45 μm PVDF filter). After coating, the connection area to the ITO electrode is cleaned with a cotton stick dipped in water / without water. If the spin coater is stopped before the film has set, particles may form, resulting in a dishomogeneous PEDOT:PSS layer.

PEDOT:PSS coated substrates were annealed at 200 °C for 10 min on a hot plate to remove any residual solvents left after spin coating. This was found to be the optimum condition for our samples, after multiple sets of experiments using different annealing temperatures. We observed that a 20-50 nm thick layer of PEDOT:PSS gives the best photovoltaic parameters.

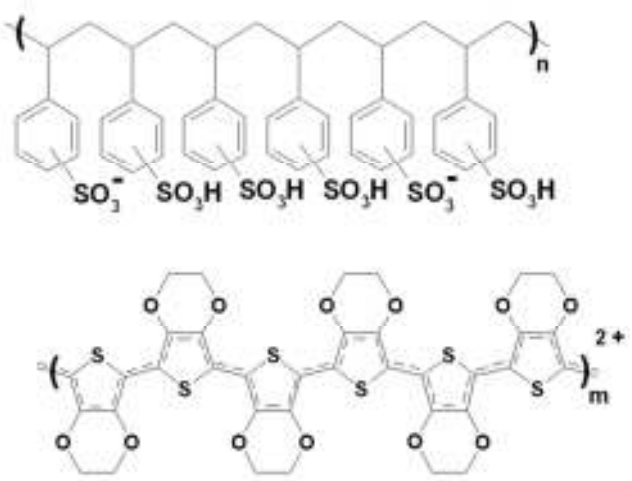

Figure 5.19. Chemical Structure of PEDOT:PSS

5.11.3 The active layer

After the deposition of PEDOT:PSS, substrates were immediately transferred inside a nitrogen glove box to avoid any further absorption of water and oxygen by the PEDOT:PSS layer. The active layer was then spin coated onto the PEDOT layer. The exact spinning speed and time employed was highly dependent on the materials and solvent used, but were generally ranging from 800 to 8500 rpm and from 30 to 300 seconds, respectively. In attempts to find the best preparation conditions, different solvents, with different evaporation temperatures, were used. The spin coated films were then placed immediately into the evaporator connected to the glove box, for the evaporation of the cathode.

5.11.4 Cathode deposition

A metal electrode was evaporated on the substrate, using a metal shadow mask. The masks more commonly used produced four devices per substrate, each with either 8.75 mm^2 or 5.0 mm^2 of active area. Typically, 20 nm of calcium were first deposited at a rate of 0.8 – 1.0 Å/s, followed by the deposition of 200 nm of aluminium at a rate of 1.0 – 1.3. Å/s, at a base pressure of approximately 10^{-6}-10^{-7} mbar. Whenever LiF was used (to replace calcium), it was evaporated at a rate of 1.0 Å/sec to obtain a thickness of 0.7-0.8 nm. Once made, devices were stored in the nitrogen glove box until testing.

The thicknesses of the different layers of the devices were measured by using a Dektak 8 surface profilometer.

Atomic Force Microscopy (AFM, Bruker Nanoscope IIIa) has been used in the tapping mode. A home-made set up allows to detect shifts in the phase angle of vibration when the oscillating tip interacts with the sample surface.

BIBLIOGRAPHY

1. Ghedini, M., Golemme, A., Aiello, I., Godbert, N., Termine, R., Crispini, A., La Deda, M., Lelj, F., Amati, M. & Belviso, S., (2011). J. Mater. Chem., 21, 13434
2. Aiello, I., Ghedini, M., La Deda, M. (2002), J. Lumin., 96, 249.
3. ASTM international, Standard Specification for solar simulation for photovoltaic testing, E 927-05, 2005; IEC 904-9, Photovoltaic devices—Part 9: Solar simulator performance requirements, IEC 904-9:1995(E) (1995).
4. http://www.sciencetech-inc.com/Midicart/shop/Brochures%5CSS150%, 20Brochure.pdf (2007).
5. K. Emery, in *Handbook of Photovoltaic Science and Engineering* (Eds: A. Luque, S. Hegedus),Wiley, Chichester, UK **2003**, Ch. 16.
6. Standard IEC 60904-3, Measurement Principles for Terrestrial PV Solar Devices with Reference Spectral Irradiance Data, International Electrotechnical Commission, Geneva, Switzerland.
7. Standard IEC 60904-1, Photovoltaic devices Part 1: Measurement of Photovoltaic Current-Voltage Characteristics, International Electrotechnical Commission, Geneva, Switzerland.
8. ASTM Standard G159, Standard Tables for Reference Solar Spectral Irradiances: Direct Normal and Hemispherical on 37° Tilted Surface, American Society for Testing and Materials, West Conshocken, PA, USA.
9. ASTM Standard G173, Standard Tables for Reference Solar Spectral Irradiances: Direct Normal and Hemispherical on 37° Tilted Surface, American Society for Testing and Materials, West Conshocken, PA, USA.
10. Standard ASTM E948, Standard Test Method for Electrical Performance of Non-Concentrator Photovoltaic Cells Using Reference Cells, American Society for Testing and Materials, West Conshocken, PA, USA.
11. K. Emery, C. R. Osterwald, T. W. Cannon, D. R. Myers, J. Burdick, T. Glatfelter, W. Czubatyj, J. Yang, in *Proc. 18th IEEE Photovoltaic Specialist Conf.*, IEEE, New York **1985**, p. 623.
12. C. R. Osterwald, *Sol. Cells* **1986**, *18*, 269.
13. H. Field, K. Emery, in *Proc. 23rd IEEE Photovoltaic Specialist Conf.,* IEEE, New York **1993**, p. 1180.
14. S. E. Shaheen, C. J. Brabec, F. Padinger, T. Fromherz, J. C. Hummelen, N. S. Sariciftci, *Appl*. *Phys*. *Lett.* **2001**, *78*, 841.
15. M. M. Wienk, J. M. Kroon, W. J. H. Verhees, J. Knol, J. C. Hummelen, P. A. van Hal, R. A. J. Janssen, *Angew*. *Chem*. *Int*. *Ed.* **2003**, *42,* 3371.

CHAPTER 6

OPV: RESULTS AND DISCUSSION

Results will be illustrated by separately discussing the two different lines of research that were developed in this work

6.1 Using a photoconductor as a donor in BHJ

During the current photogeneration process in BHJ, photon absorption is followed by excitons generation. Excitons are bound electron-hole pairs which are difficult to separate at room temperature in the bulk of organic materials. These excitons diffuse, eventually reaching the interface between the donor and the acceptor phases. At the heterojunction, excitons may separate into free charge carriers (electrons and holes), which drift and diffuse towards the electrodes, where they are collected, entering the external circuit.

The performance of bulk heterojunctions depends on many factors. Among these, we can mention light absorption, exciton diffusion, efficiency of exciton dissociation at the heterojunction and charge mobility in the donor and acceptor materials. Although exciton dissociation at the heterojunction is extremely important in determining photocurrents, it is still poorly understood, because of the intrinsic difficulties of both experimental studies and modellizations, and methods for boosting exciton dissociation are needed.

The use of intrinsic photogenerators (i.e. substances that already exhibit a tendency for photogeneration in the bulk, were no interface is present) in OPV has never been reported in the literature, although in principle it could give an important contribution in order to increase the efficiency of exciton dissociation. In fact, a substance that intrinsically photogenerates charges in the bulk, may very well keep such property in the BHJ mixture. One of the aims of this dissertation is to establish if such hypothesis holds.

We choose to explore BHJ formed by $PC_{61}BM$ and the cyclopalladated Nile Red complex 1 (for the structure, see the previous chapter), that belongs to a new class of photoconductors[1] in which the HOMO is positioned on the ancillary Schiff base and the LUMO on the cyclometallated ligand, both coordinated by either a Pt(II) or a Pd(II) metal atom, as shown in Fig. 6.1.

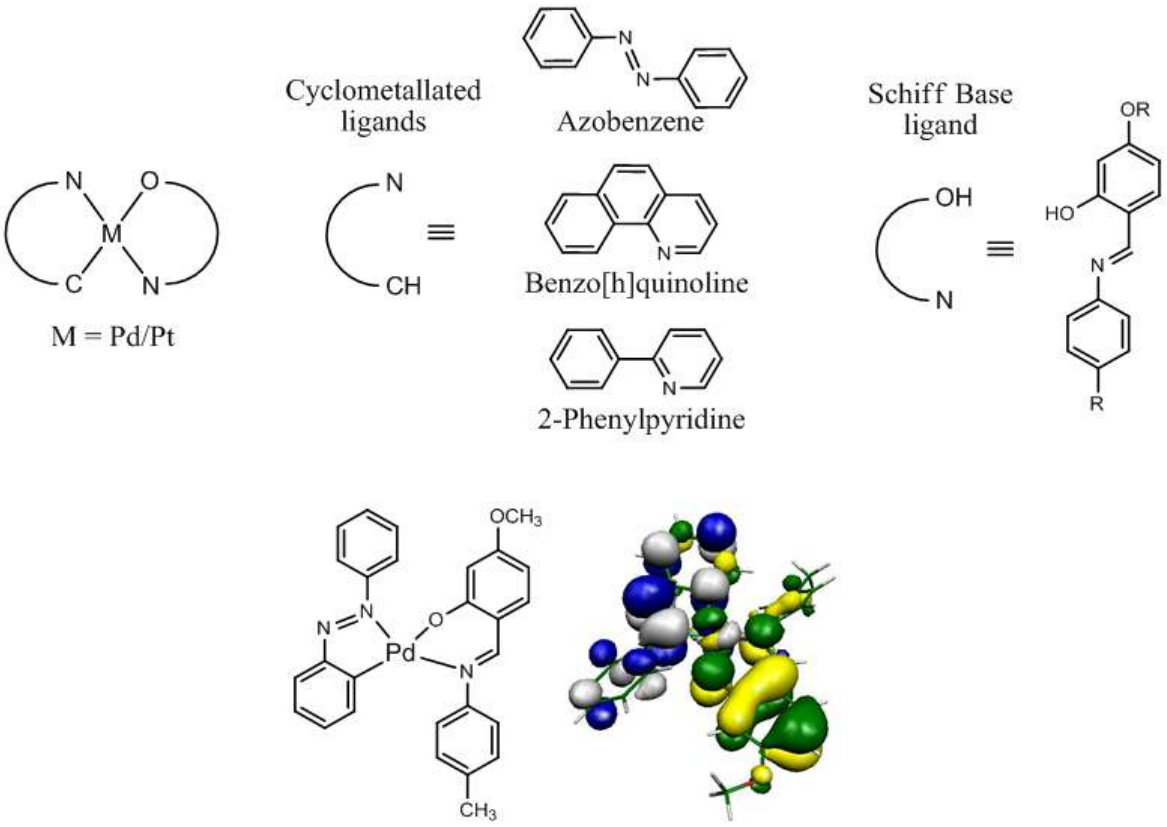

Figure 6.1: Above: general chemical structure of photoconductive cyclometallated complexes. Below: chemical structure in the case of the azobenzene complex, with HOMO (in green/yellow) and LUMO (in white/blue) distribution.

It is believed that this physical separation is at the origin of the intrinsic charge photogeneration properties of these materials. However, the HOMO/LUMO separation is also important for another reason. In fact, the proper choice of ligands is an easily accessible method for tuning absorption wavelengths. Complex **1** was chosen because, when compared to other compounds of the same class (see Fig. 6.2) it exhibits an extended absorption range, up to $\lambda \sim 650$ nm, which is desirable for photovoltaic applications. In addition, the presence of long alkyl chains improves processability during spin coating.

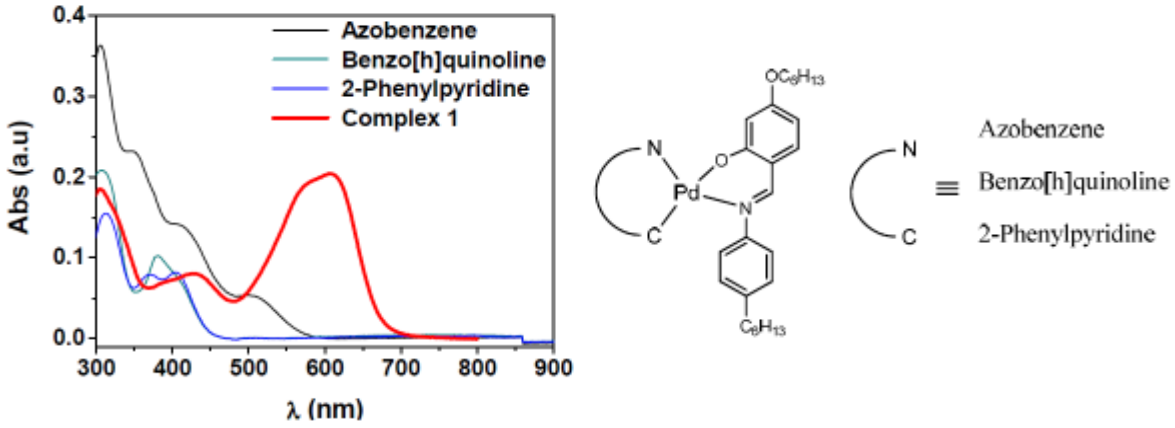

Figure 6.2: Comparison between the absorption of complex **1** and of other cyclometallated complexes of the same class.

As in the case of other complexes of the same class[2-5], complex **1** is also a photoconductor. Photoconductivity measurements were carried out both on pure **1** and on samples doped with less than 1% of C_{60}. As it is evident from the results, illustrated in Fig. 6.3, the photoconductivity increases by two orders of magnitude in the presence of C_{60}, without a measurable increase in absorption. Since C_{60} is a well known electron acceptor, such increase in photoconductivity shows that i) there is a significant electron transfer from the excited state of **1** to C_{60} and ii) complex 1 is a hole conductor, as already known for the other complexes of the same class[1]. On the basis of these observations, the use of **1** in BHJ devices, in combination with soluble derivatives of C_{60}, seemed possible.

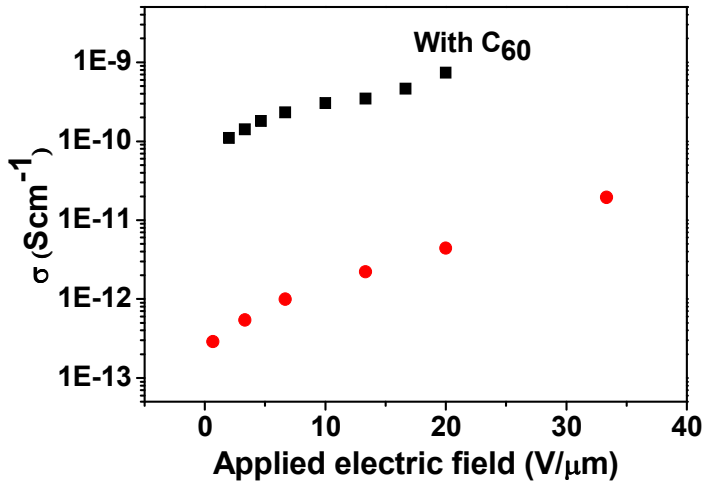

Figure 6.3: Photoconductivity of pure complex **1** and of complex **1** doped with C_{60}, as a function of the applied electric field. The measurements were carried out at $\lambda = 633$ nm, with a light intensity $I = 0.65$ W/cm^2.

The most common soluble commercial C_{60} compound that plays the role of acceptor in BHJ is $PC_{61}BM$, which was used, in combination with **1**, to obtain BJH photovoltaic cells, as described in the experimental section. The chemical structure of $PC_{61}BM$ is shown in Fig. 6.4, together with a schematic diagram of the energy level alignment of frontier orbitals for the donor (**1**), the acceptor ($PC_{61}BM$), the PEDOT:PSS hole injection layer and the work functions of the electrodes.

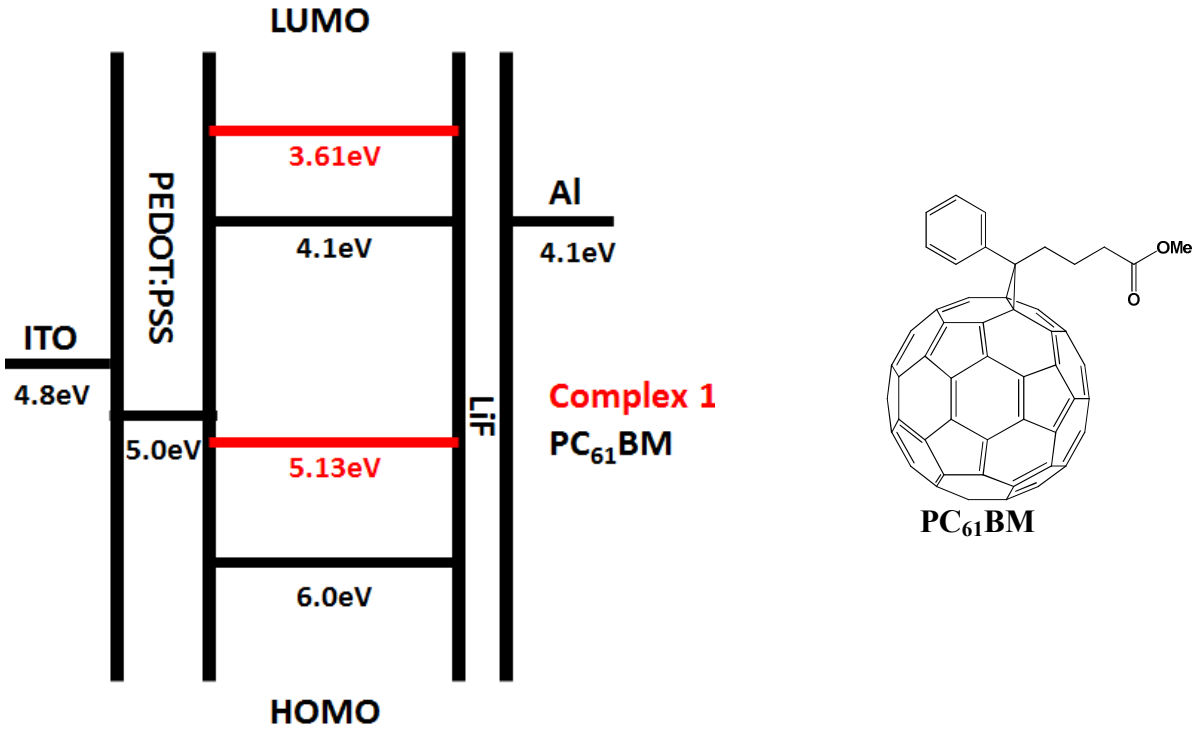

Figure 6.4. Schematic illustration of the energy levels alignment of the materials used in the devices. The chemical structure of $PC_{61}BM$ is also shown.

It is well known that in BHJ solar cells, performance is strongly affected by the morphology of the interpenetrating phases, which, in turn, depends on both the solvent and the composition[6]. BHJ cells were prepared as mentioned in the experimental section by using different solvents, such as dichloromethane, chloroform and chlorobenzene. The best performing solvent was chlorobenzene and only results obtained by using such solvent will be illustrated in the following.

Typical J-V curves in the dark and under illumination are shown in Fig. 6.5 for the **1**:$PC_{61}BM$ weight ratio 1:4, which gave the best results.

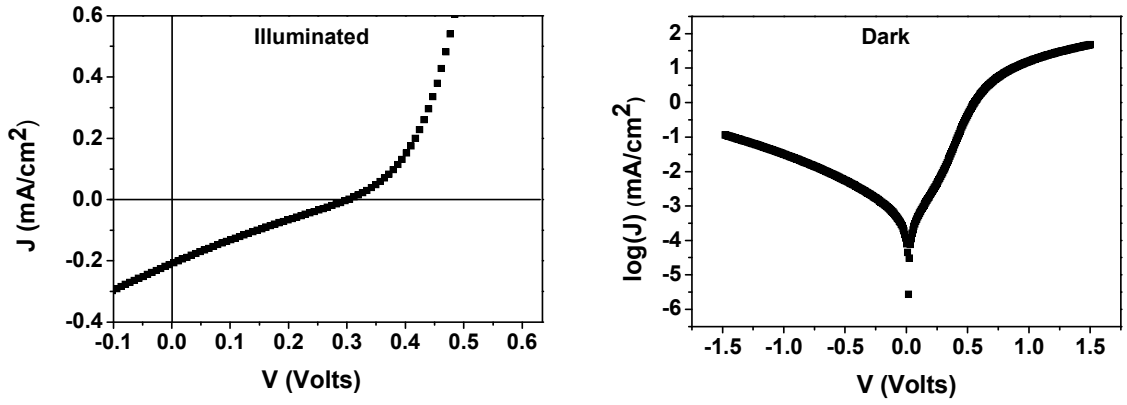

Figure 6.5: Typical J-V curves for the **1**:$PC_{61}BM$ system with a 1:4 weight ratio, under 100 mW/cm^2 light illumination (AM 1.5) and in the dark.

The various parameters of the devices with different compositions are summarized in Table 6.1. With a 1:1 composition, no diode behaviour was observed in the dark and it was not possible to perform measurements. It is evident from Table 1 that as the concentration of $PC_{61}BM$ is increased Jsc increases, which is the main reason leading to a higher efficiency, whereas all the other parameters remains almost constant and independent from composition. However, when the content of complex **1** becomes too low (1:5 composition) the efficiency decreases.

1:$PC_{61}BM$ Weight Ratio	Jsc (mA/cm^2)	Voc (Volts)	Efficiency	Fill Factor
1:2	0.017	0.24	0.001	0.25
1:3	0.035	0.34	0.003	0.26
1:4	0.195	0.30	0.014	0.24
1:5	0.06	0.35	0.005	0.25

Table 6.1. Typical parameters of devices at different compositions of the active layer.

An explanation for the improved performance at higher $PC_{61}BM$ concentration can be found by considering the atomic force microscopy (AFM) images obtained in the phase mode, shown in Fig. 6.6.

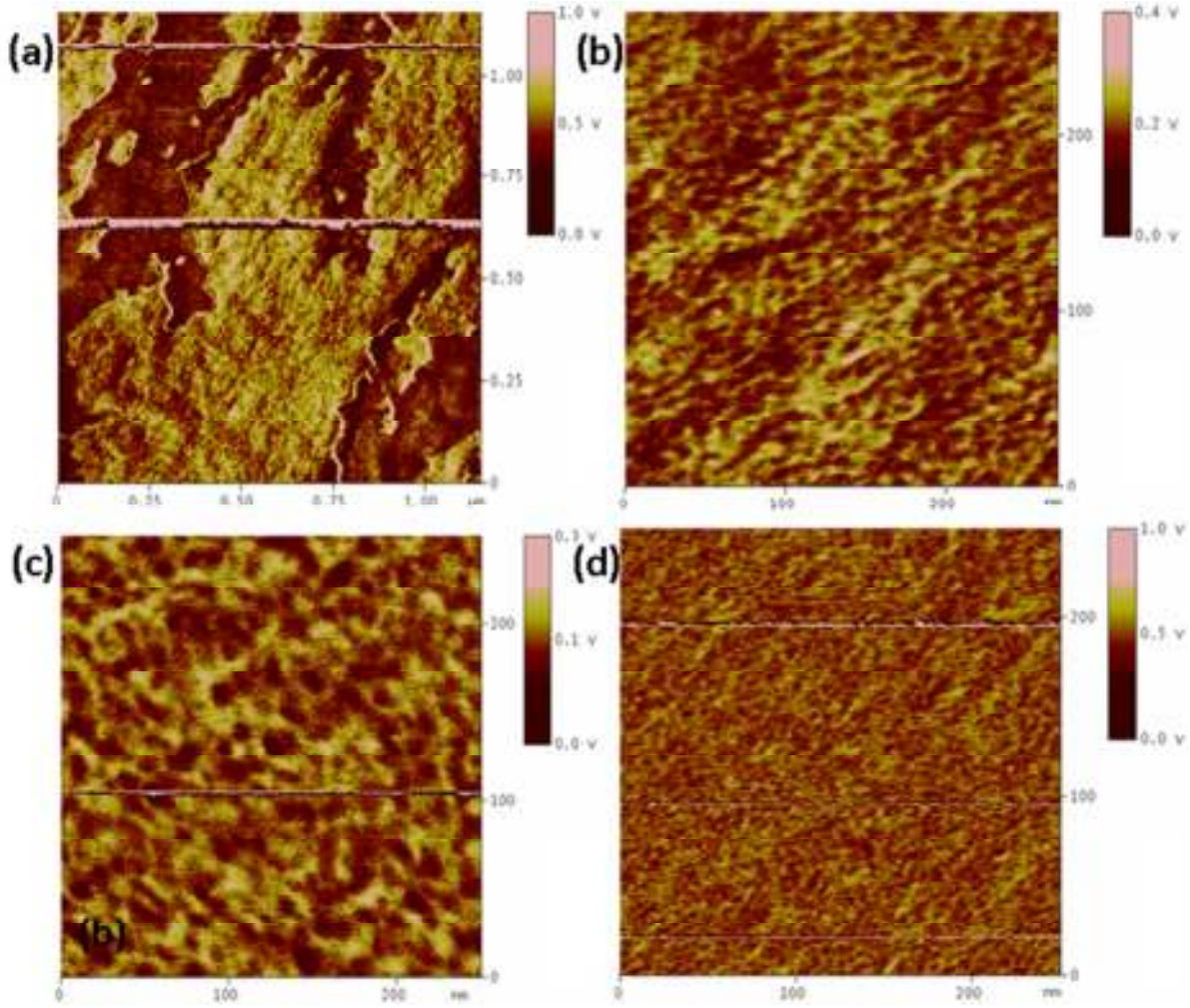

Figure 6.6: AFM phase images of the **1**:$PC_{61}BM$ active blend with weight ratios 1:1 (a), 1:2 (b), 1:3 (c) and 1:4 (d).

For a 1:1 composition, large patches of the two phases with dimensions of several hundred nanometers can be observed. As the $PC_{61}BM$ concentration is increased, the morphology evolves towards an interpenetrated network, with typical dimensions of the domains ~ 25 nm for the 1:3 composition and ~ 10 nm for the 1:4 composition. A better performance in BHJ with well-connected domains in this size range is expected, because it induces a higher current photogeneration and reduces the series resistance[7].

However, even for the best samples, efficiency is rather low, by roughly two orders of magnitude when compared to the best performing materials in BHJ[8]. One of the possible reasons for the low performance can be found in the difficulty in obtaining a good morphology of the interpenetrating phases in the BHJ, which is typical in devices using LMW materials. Thermal annealing, often used in order to improve morphology[9], was also performed on our samples at 70 °C and 120 °C, but it did not lead to an improvement of the

efficiency, that actually decreased, indicating that the morphology of the active layer becomes even worse after thermal treatments.

Another reason for the low performance is the low absorption of **1**, which is more than one order of magnitude lower than what would be required for a good efficiency. The absorption of a film with a 1:4 composition is shown in Fig. 6.7. Even at the peak for $\lambda \sim 600$ nm the absorption coefficient is $\alpha < 10^4$ cm^{-1}, corresponding to an absorption of less than 20 % of the incident photons in a 100 nm thick device.

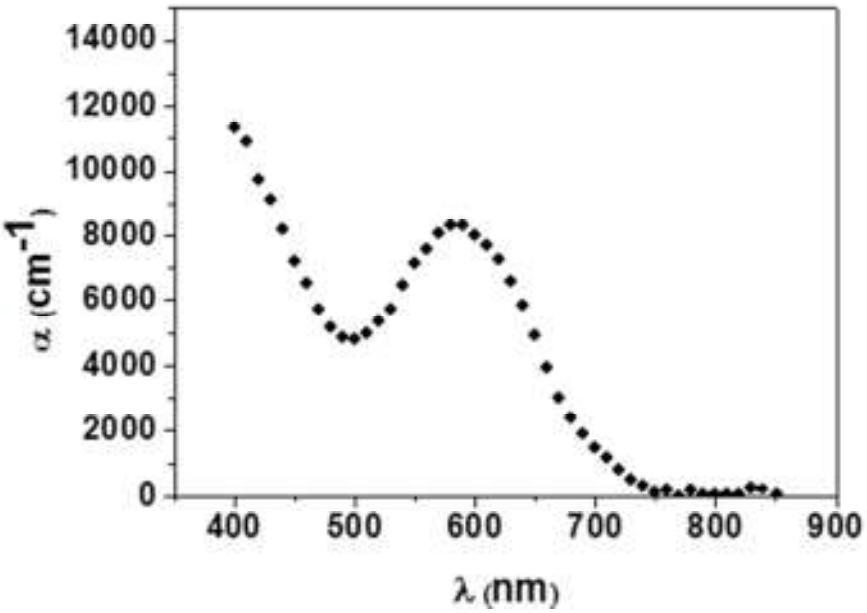

Figure 6.7. Absorption of a sample with a **1**:$PC_{61}BM$ = 1:4 weight ratio.

Despite the low performance, a deeper level of analysis of the data can be interesting in assessing the importance of using a photoconducting component in organic photovoltaic devices. The external and internal quantum efficiencies of a device with a 1:4 composition is shown in Fig. 6.8.

As expected, the EQE follows absorption rather well, except for a shift of the efficiency towards higher wavelengths, but what is more revealing is the wavelength dependence of IQE. It is evident that at higher wavelengths, where the contribution of **1** to absorption is higher, higher values of IQE are observed. There is a monotonic decrease of IQE throughout the visible region (data below 750 nm, where the absorption of the devices are very low, are greatly affected by error and are not shown). In other words, light absorbed at higher wavelengths is more effective in generating photocurrent. Although IQE dependences on

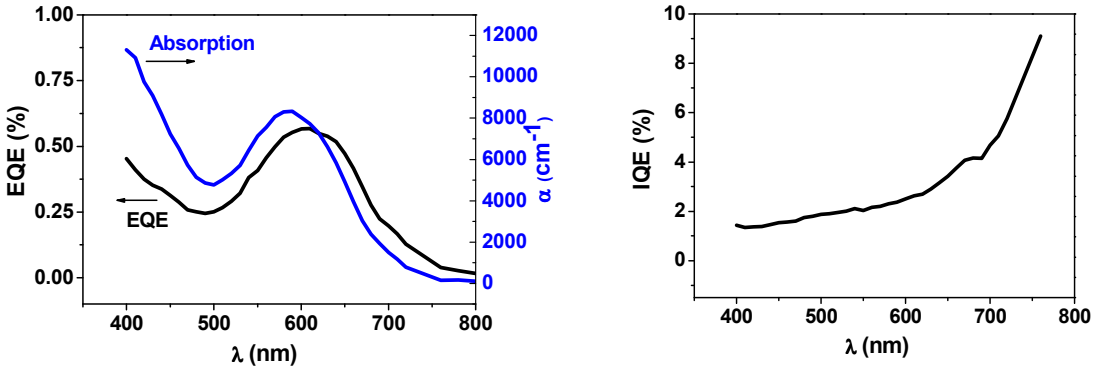

Figure 6.8. (a) Wavelength dependence of external quantum efficiency and absorption in a film of 1:$PC_{61}BM$ with a 1:4 composition. (b) Internal quantum efficiency of the same film

wavelength reported in the literature are never flat, in this case the behaviour is rather unusual, with IQE varying by a factor 6 between λ ~ 400 nm and λ ~ 750 nm.

In order to rationalize this observation it is necessary to consider the relative contribution to light absorption of the two components of the active layer, as shown in Fig. 6.9.

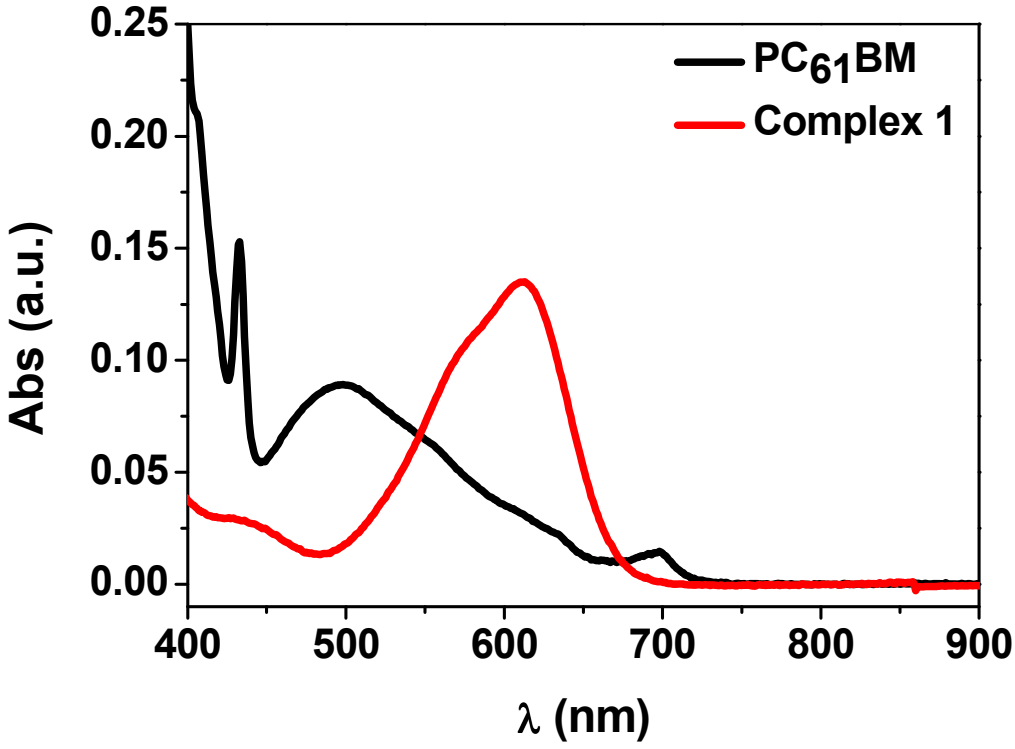

Figure 6.9. Absorption in solution of Complex **1** and of $PC_{61}BM$.

Complex **1** exhibits an absorption maximum at $\lambda \sim 600$ nm, with an absorption edge at $\lambda \sim 700$ nm and residual absorption up to $\lambda \sim 800$ nm. Absorption decreases at wavelengths below $\lambda \sim 600$ nm, but not dramatically. $PC_{61}BM$ instead shows very little light absorption at high wavelengths, with an extinction coefficient almost monotonically increasing as the wavelength decreases. Simplifying, and considering that $PC_{61}BM$ is much more abundant in the films, we can say that at high wavelengths the contribution to absorption is due mainly to complex **1** and, as the wavelength is decreased, the contribution of $PC_{61}BM$ becomes more and more important. Note how the IQE curve is roughly shaped like the mirror image of the absorption curve for $PC_{61}BM$.

It is clear from the wavelength dependence of quantum efficiency that light absorption by complex **1** leads to a much higher photon-to-collected-charge conversion than absorption by $PC_{61}BM$. The comparison between experiments carried out with different relative concentrations of the components do not show a decrease of the effect when the size of the domains decreases, ruling out the hypothesis that the different performance of the two components could be due to different exciton diffusion lengths of the two materials. Similarly, the contribution of "hot excitons"[10], can be excluded, as the higher conversions are obtained for higher wavelengths.

Results can instead be explained by considering the intrinsic photogeneration properties of complex **1**. The tendency of **1** towards charge photogeneration, even in the bulk, could be the explanation for the easy charge transfer to $PC_{61}BM$, when compared to other donors. In contrast, absorption by $PC_{61}BM$ is less efficient. In addition, given the fact that complex **1** is an intrinsic photoconductor, a contribution to charge photogeneration far from the interface could also be important. In other words, the thickness of the interface which is relevant for exciton dissociation might not be reduced to a single layer of molecules when the exciton is produced in the complex **1** side of the heterojunction.

The data presented above clearly show an unusual behaviour that, at least in the case of the compounds studied, indicates that the use of a photoconductor as a component of excitonic solar cells can dramatically affect exciton dissociation efficiency.

6.2 Hydrazonic low molecular weight donors for OPV

In another research line, the effectiveness of new hydrazonic donors in bulk heterojunction solar cells was investigated. The chemical structure of compounds **2** and **3** is shown in Fig. 6.10. These compounds were chosen because their structure is similar to the structure of donors recently used as effective components in BHJ[11]. Their HOMO and LUMO levels make them suitable as BHJ donors in combination with different PCBM derivatives, such as $PC_{61}BM$ and $PC_{71}BM$, as acceptors.

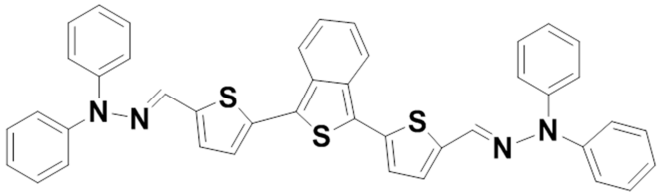

(2)

HOMO - 5.25
LUMO -2.90

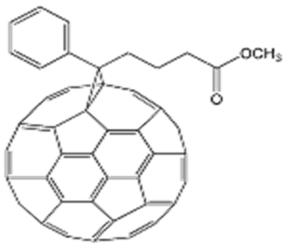

$PC_{61}BM$

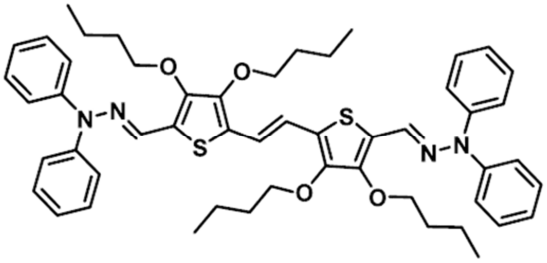

(3) **HOMO - 5.08**
LUMO -2.57

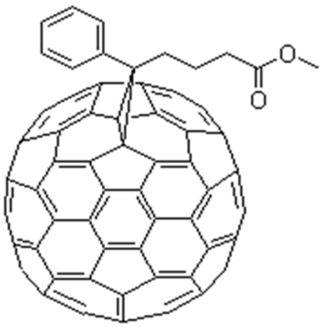

$PC_{71}BM$

Figure 6.10: Chemical structure of compound **2** and **3** along with their HOMO and LUMO values (Donor). The structure of the $PC_{61}BM$ and $PC_{71}BM$ is also shown.

Let us first discuss the results obtained with **2**. Bulk heterojunctions were prepared by using the techniques described in the materials and methods section. In order to optimize efficiency, the following different parameters were varied and optimized:

1. Composition
2. Solvents for spin-coating
3. PEDOT:PSS thickness
4. Active layer thickness
5. Al evaporation rate

6. Temperature during spin-coating
7. Solvent vapour pression during spin-coating
8. Nature of the acceptor
9. Nature of cathode

6.2.1 Effect of sample composition and solvents

It is well known that the performance of BHJ solar cells is strongly affected by the morphology of the interpenetrating phases, which in turn, depends on both the **solvent** and the **composition**[6]. BHJ cells of compound **2** and $PC_{61}BM$ were prepared using spin coating, as mentioned in the materials and methods section, by using different solvents, such as dichloromethane, chloroform, chlorobenzene and dichlorobenzene. The effect of different compositions and different solvents will be discussed in this section. In all cases, both the PEDOT:PSS and the active layer thickness were kept at 50 nm each.

In table 6.2 , the I/V parameters of BHJ with three different compositions (1:2, 1:3 and 1:4) obtained from chlorobenzene solutions are summarized. It can be noticed that by decreasing the composition of **2**, the open circuit voltage decreases monotonically. The best efficiency was observed in the case of the 1:3 composition. From the table it is also clear that this is mainly due to a major increase in the short circuit current of the device. This can be attributed to the improved active layer morphology, as it will be show in one of the following sections.

Sample Composition 2:$PC_{61}BM$	**Fill Factor (FF)**	**Efficiency (η) %**	**Short circuit current (I_{sc}) mA/cm^2**	**Open circuit voltage (V_{oc}) Volts**
1:2	0.30	0.20	1.25	0.54
1:3	**0.32**	**0.29**	**1.73**	**0.53**
1:4	0.36	0.19	1.24	0.42

Table 6.2: I/V parameters of BHJ of 2:$PC_{61}BM$ with different composition.

The effect on the I/V parameters of using different solvents during spin-coating was studied on BHJ formed by **2** and PCBM at a 1:3 composition. Spin coating was always performed at room temperature. Results are summarized in table 6.3.

Solvent (boiling temperature)	Fill Factor	Efficiency %	Short circuit current mA/cm^2	Open circuit voltage Volts
Dichloromethane (40 ^{0}C)	0.30	0.25	1.45	0.56
Chloroform (60 ^{0}C)	0.31	0.27	1.70	0.52
Chlorobenzene (133 ^{0}C)	**0.32**	**0.29**	**1.73**	**0.53**
Dichlorobenzene (184 ^{0}C)	0.31	0.28	1.61	0.57

Table 6.3: I/V parameters of BHJ of 2:$PC_{61}BM$ with different solvents.

The effect of using solvents with different volatility on the I/V parameters is almost negligible, except in the case of dichloromethane, where the efficiency is lower.

6.2.2 Effect of PEDOT:PSS thickness

In organic solar cells, a layer of PEDOT:PSS between the active layer and the electrode improves the interface properties[12]. Use of PEDOT:PSS also changes the shape of the EQE curve, an effect which is due to the doping of the active layer by PSS[13, 14]. It is observed that the use of PEDOT:PSS increases the open circuit voltage in fullerene based cells[15]. Apart from this, in solar cells, recombination of charge carriers can take place at the "wrong" electrodes, e.g. a negative charge may reach the positive electrode (ITO). To prevent this loss mechanism, charge blocking layers can be introduced between the molecular highway structure and the respective electrode, preventing the charge carriers of opposite sign from reaching the electrode. This can be done by using PEDOT:PSS on the ITO. However, the effect of such layer is not completely clear. There are contradictions among different experimental investigations on the influence of PEDOT:PSS on the solar cell performance, mainly due to the fact that the device performance is dependent on PEDOT:PSS thickness[16] and that PEDOT:PSS properties are dependent on the thermal treatments[17].

So, the PEDOT:PSS layer thickness should be optimized for each set of materials used, considering also that very thin layers yield more pin holes, while thicker layers cause larger increase in the series resistance[16]. During our experiments, in order to optimize the thickness of the PEDOT:PSS layer, we prepared samples with four different thicknesses at one optimized active layer thickness for compound **2**. Results are summarized in table 6.4 while the dark current of the devices is shown in Fig. 6.11.

OPV Parameter	PEDOT:PSS 20 nm	PEDOT:PSS 35 nm	PEDOT:PSS 50 nm	PEDOT:PSS 90 nm
Fill Factor (FF)	0.30	0.31	**0.31**	0.35
Efficiency (η)	0.20	0.22	**0.24**	0.25
Short circuit current (I_{sc}) mA/cm^2	1.29	1.38	**1.43**	1.49
Open circuit voltage (V_{oc}) Volts	0.50	0.50	**0.55**	0.49

Table 6.4. I/V parameters of BHJ of 2:$PC_{61}BM$ with different PEDOT:PSS thickness.

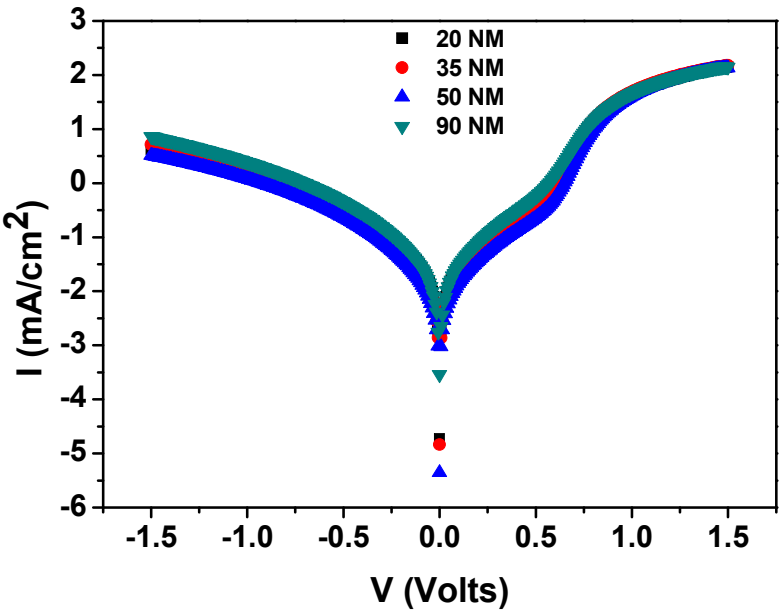

Figure 6.11: Typical dark current of BHJ of 2:$PC_{61}BM$ with different PEDOT:PSS thickness

It can be observed that as the thickness of the PEDOT:PSS is increased the short circuit current increases monotonically, but after a certain thickness the open circuit voltage goes down. During our experiments we observed that the Fill Factor remains almost constant. The best efficiency was obtained with thick PEDOT:PSS layers. However, a thickness of 50 nm was chosen for the following optimizations, because easier to obtain than even higher thicknesses. In addition, a 50 nm thickness gives a better (lower) dark current than a 90 nm one.

6.2.3 Effect of different active layer thickness

There is a trade-off between absorption, exciton diffusion length, and carrier mobility of organic materials. Because short exciton diffusion length and poor carrier mobility limit the total thickness of active layers in photovoltaic devices, one cannot increase the thickness of the active layer to increase absorption. Generally, thickness influences electrical performance and optical field distribution within photovoltaic devices.

I/V parameters for BHJ of **2** and PCBM (1:3 composition) for different active layer thicknesses are summarized in table 6.5. Dichloromethane was used as a solvent for spin coating. In Fig. 6.12, typical dark current associated with different active layer thicknesses are shown.

Active layer thickness nm	Efficiency (η)	Open circuit voltage (V_{oc}) Volts	Short circuit current (I_{sc}) mA/cm^2	Fill Factor (FF)
50	**0.25**	**0.56**	**1.45**	**0.30**
70	0.22	0.58	1.31	0.30
90	0.18	0.58	1.10	0.30
110	0.16	0.59	0.91	0.29

Table 6.5. I/V parameters of BHJ of 2:$PC_{61}BM$ with different active layer thickness

It is evident that OPV not all parameters are highly dependent on the active layer thickness of a BHJ cells. The main variation is with the short circuit current, that decreases for thicker samples. This is the main reason pushing the efficiency up in thinner cells. Below a 50 nm thickness, samples do not show any diode behaviour in the dark, probably because of shortening.

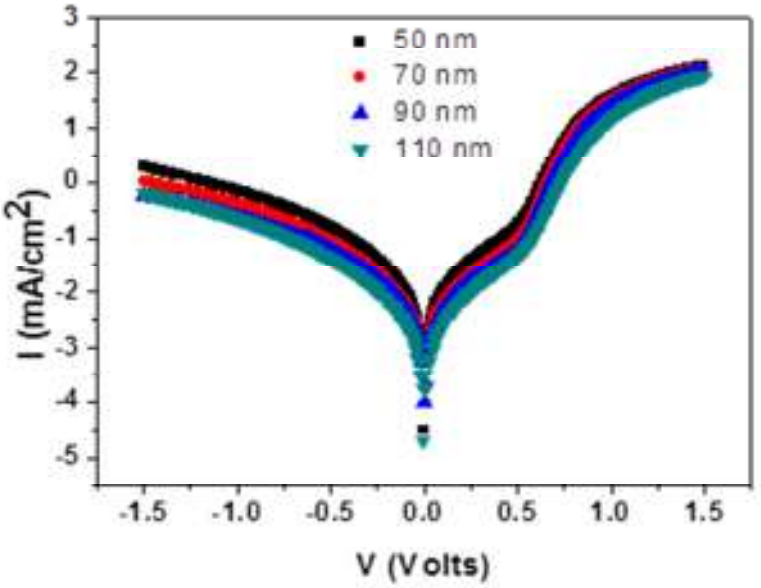

Figure 6.12: Dark current of BHJ of 2:$PC_{61}BM$ with different active layer thickness

6.2.4 Effect of different Al evaporation rate.

Aluminium odidation was observed during cathode evaporation on the sample of BHJ of **2**:$PC_{61}BM$. There could be many reasons for this such as : PEDOT:PSS is highly hygroscopic in nature, and water absorbed by PEDOT:PSS from ambient air results in the degradation of cell performance [18]. In addition, PSS is an acidic material. Therefore, there is concern that PEDOT:PSS accelerates the degradation of photovoltaic cells by oxidizing certain components of the cells. Apart from that the slow evaporation rate of aluminium during thermal evaporation can lead to the oxidation.

The oxidation of the aluminium in our samples were attributed dueto the slow evaporation rate (0.3 Å/sec) used for thermal evaporation[19]. When we increased the aluminium evaporation rate the oxidation problem of the samples were eliminated.were observed that the quality of the aluminium is degraded just after taking out the samples from the thermal evaporator. This was due to the the

6.2.5 Effect of Temperature during spin-coating

Most bulk heterojunction devices are prepared by spin coating. In most cases, post-fabrication thermal annealing is performed, in order to improve the morphology of the active layer[20]. It is necessary to optimize the phase separation between the donor-rich and the acceptor-rich phases (in other words morphology), with the aim of increasing the interface area, adjusting the domains size to the exciton diffusion length and assuring a good connectivity of the two phases. However, in our BHJ formed by **2** and PCBM annealing was not effective. Actually, the performance of the devices was worse after annealing.

An alternative way of tuning morphology consists in performing spin coating at different temperatures. Temperature controls a series of relevant parameters of spin coating, such as solvent evaporation rate and viscosity, affecting both the final thickness and the morphology. The spinning rate was adjusted in order to obtain always the same thickness of the active layer, regardless of the temperature. Experiments were performed by spin coating a mixture of **2** and $PC_{61}BM$ with a 1:3 composition in dichlorobenzene at four different different temperatures: room temperature, 60, 90 and 130 $^{\circ}C$. In each sample, other parameters, such as PEDOT:PSS thickness, and the LiF/Al electrode thickness, were kept constant for better comparison. The resulting I/V parameters are summarized in table. 6.6 and the corresponding I-V characteristics are shown in Fig. 6.13.

Temperature (^0C) (active layer thickness)	Open circuit voltage Volts	Short circuit current mA/cm^2	Fill Factor	Efficiency %
25 (65 nm)	**0.58**	**1.58**	**0.29**	**0.27**
60 (60 nm)	0.49	1.37	0.34	0.22
90 (60 nm)	0.27	1.20	0.33	0.11
130 (85 nm)	0.41	0.95	0.30	0.12

Table 6.6. I/V parameters of BHJ of 2:$PC_{61}BM$ with different temperature during spin coating.

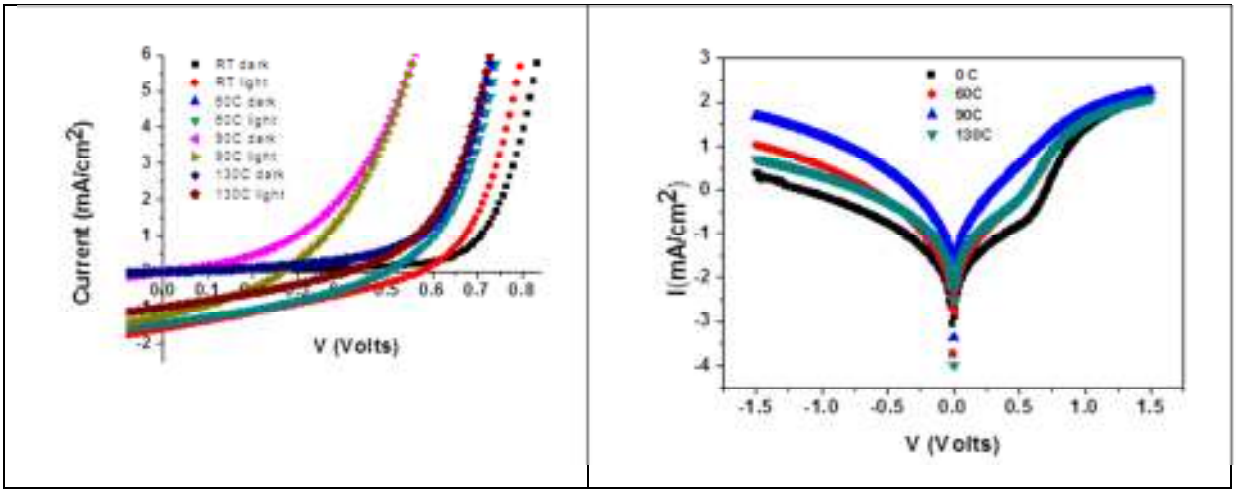

Figure 6.13: I/V characteristics of BHJ of 2:$PC_{61}BM$ with different temperature during spin coating

It is evident that the best results are obtained at room temperature. Both the short circuit current and the open circuit voltage were lower in the samples coated at higher temperature, inducing a lower efficiency. Only the fill factor improved slightly, but not enough to compensate the deterioration of the other parameters. This trend is in accordance with the results discussed in the previous section, where we studied the effect of using different solvents with different evaporation rate (boiling temparature): the higher the boiling point of the solvent, the better the I/V parameters. In terms of evaporation rate, the effect of spin coating at higher temperatures is the same as the effect of using solvents with a lower boiling temparature.

6.2.6 Effect of Solvent vapour pression during spin-coating

As discussed in the previous sections, a low evaporation rate seems to induce a better performance, that can be attributed to a better morphology. However, the two most obvious ways of reducing the solvent evaporation rate were not experimentally accessible. Using a temperature below RT during spin coating was not allowed by our experimental setup, while using a solvent with a boiling temperature above 184 °C (the boiling point of dichlorobenzene) would have negatively affected sample homogeneity.

It was then decided to lower the evaporation rate by spin coating in a solvent atmosphere. We prepared different samples by placing an open container with the solvent in the closed spin coater chamber and waiting for a different amount of time before

starting the spin coating process. The resulting I/V parameters of BHJ of **2** and $PC_{61}BM$ with a 1:3 composition obtained from spinning from dichlorobenzene solutions are summarized in table 6.7 The corresponding I-V curves are shown in Fig. 6.14.

Time for solvent atmosphere	Fill Factor (FF)	Efficiency (η)	Short circuit current (I_{sc}) mA/cm^2	Open circuit voltage (V_{oc}) Volts
Without solvent	**0.31**	**0.25**	**1.47**	**0.55**
1 min	0.30	0.20	1.23	0.55
3 min	0.30	0.22	1.34	0.56
5 min	0.31	0.19	1.38	0.45

Table 6.7: I/V parameters of BHJ of **2** and $PC_{61}BM$ with a 1:3 composition obtained from spinning from dichlorobenzene solutions

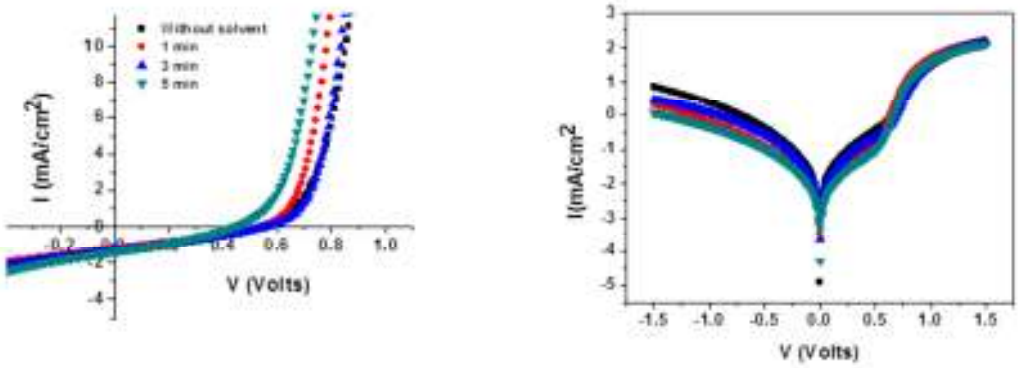

Figure 6.14: I/V characteristics of BHJ of 2:$PC_{61}BM$ with different solvent vapor pression during spin coating.

Experimental results show that spin coating in a solvent-reach atmosphere does not affect the fill factor whereas it induces a decrease in the efficiency. This is mainly due to a decrease in the short circuit current. In conclusion, the results of this experiment were different from what we expected. It is hard to say wether this is due to a real lack of effect of a solvent-rich atmosphere in slowing down the evaporation rate or to the poor control of the experimental (partial pressure of the solvent) conditions.

6.2.7 Effect of the nature of accepter and cathode

After optimizing other parameters, the effect of using different PCBM derivatives as well as different cathode electrode combinations was investigated. The anode and cathode directly influence the built-in potential within the OPV devices, due to the difference of work function between them[21,22]. The variation in work function of a specific electrode also changes the built-in electrical field and sometimes affects the V_{OC} of the device[23,24]. Even OPV devices with different electrode materials, but with the same work function, may have a different efficiency, an effect attributed to differences in the polarity of the metal[25].

In order to campare the effect of different PCBM acceptors we chose the usual 1:3 composition and built BHJ devices with either $PC_{71}BM$ or $PC_{71}BM$. The two different cathodes were Ca/Al and LiF/Al. The PEDOT:PSS and active layer thicknesses were both kept at 50 nm in all samples. Results are summarized in table 6.8 while the I-V curves are shown in Fig. 6.14.

I/V Parameter	LiF/Al $PC_{61}BM$	LiF/Al $PC_{61}BM$	Ca/Al $PC_{61}BM$
Fill Factor (FF)	0.32	0.32	0.35
Efficiency (η)	0.29	0.48	0.59
Short circuit current (I_{sc})	1.67	2.66	2.69
Open circuit voltage (V_{oc})	0.54	0.57	0.62

Table 6.8: I/V parameters of BHJ obtained using **2** with different electrodes and different PCBM acceptors, with a 1:3 sample composition.

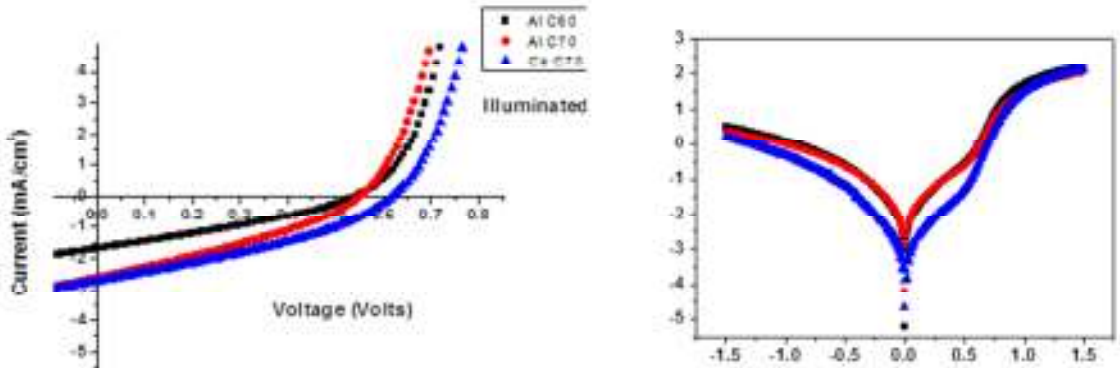

Figure 6.14: Typical I-V curve of BHJ obtained using **2** with different electrodes and different PCBM acceptors, with a 1:3 sample composition.

The efficiency increases by more than 65% when $PC_{71}BM$ is used as an acceptor instead of $PC_{61}BM$. This improvement was mainly due to increase in the short circuit current, with a little contribution from an increase of the open circuit voltage. The increase in I_{sc} was expected because $PC_{71}BM$ shows higher absorption in the visible range when compared to $PC_{61}BM$. However, the increase in the open circuit voltage is mailnly due to the different LUMO level of $PC_{71}BM$ (- 4.3 eV) when compared to that of $PC_{61}BM$ (- 4.1 eV).

It is also evident that the use of Ca/Al as a cathode further improves the efficiency. On giving a close look to the I/V parameters, it is clear that this increase is mainly due to an increase in the open circuit voltage of the solar cell. This can be attributed to an increase of the built in potential in the active layer[26].

The atomic force images of devices prepared with compound **2** and $PC_{71}BM$, both in topography as well as in phase contrast are shown in Fig. 6.15 The tapping mode of AFM was used for acquisition.

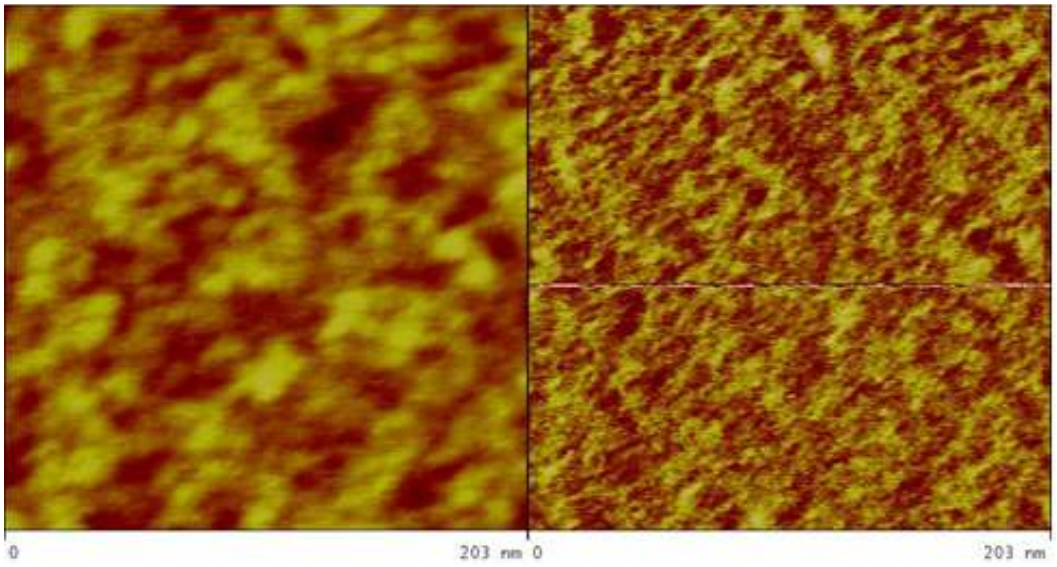

(a)

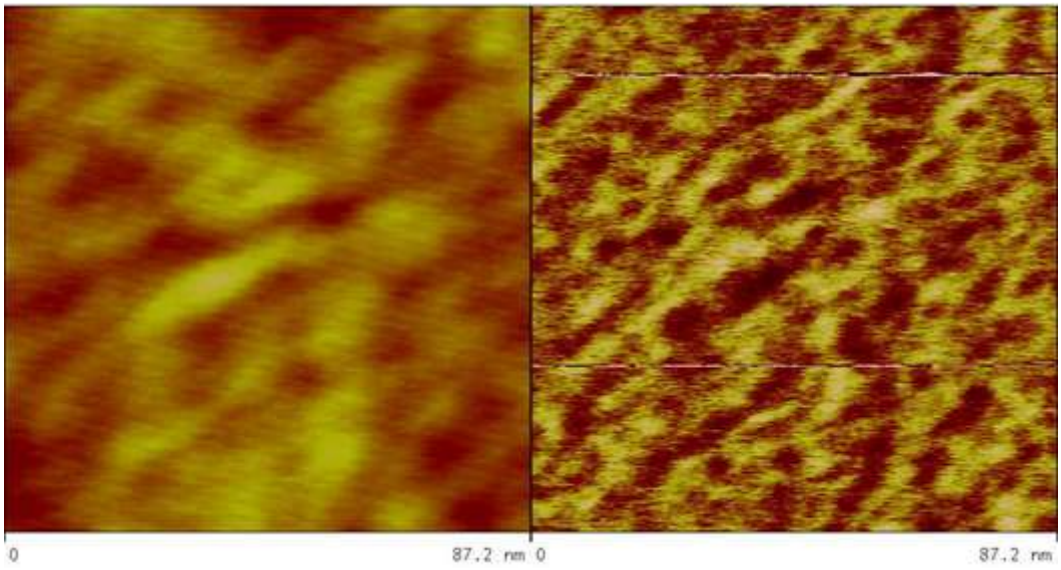

(b)

Figure 6.15: AFM images with (left) topographic and (right) phase contrast of compound **2**:$PC_{71}BM$ BHJ.

The external and internal quantum efficiencies for the same composition are shown in Fig. 6.16 Together with the absorption spectrum.

EQE follows absorption well at higher wavelengths, and it is almost flat in the wavelength range from 370 nm to 570 nm. The internal quantum efficiency (IQE) is also rather flat, but with a dip at lower wavelengths a. The average IQE value was found to be around 35 %.

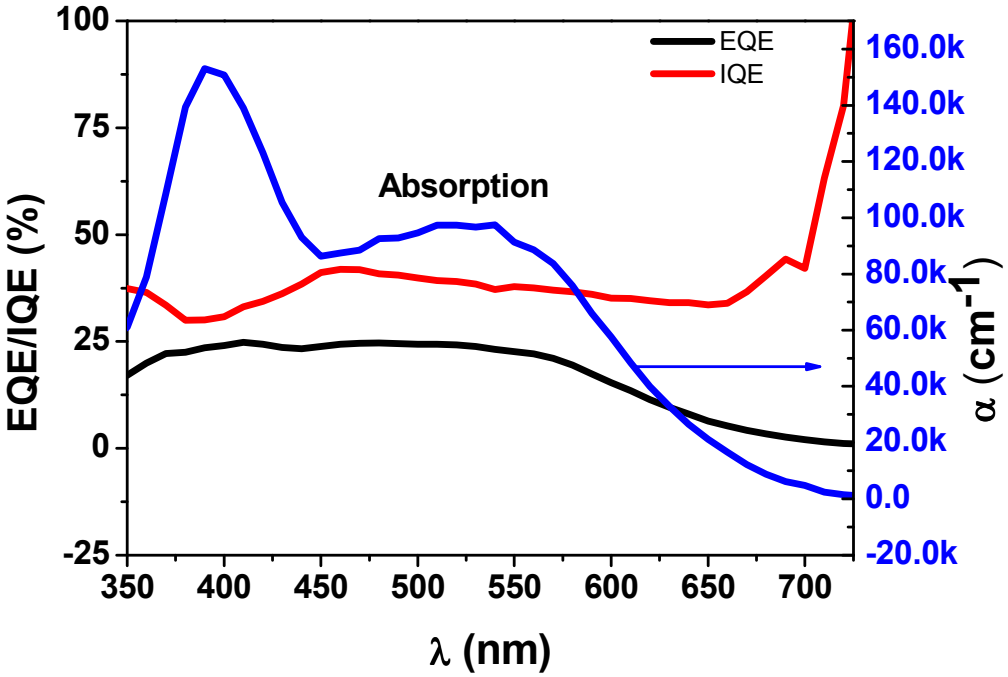

Figure 6.16: EQE and IQE curves for BHJ of **2** and $PC_{71}BM$ with a 1:3 weight ratio. The absorption curve is also shown (blue).

After optimizing the performance of BHJ prepared using **2** by changing various processing parameters, the same was done by using **3.** The structure of **3** is shown in Fig. 6.17

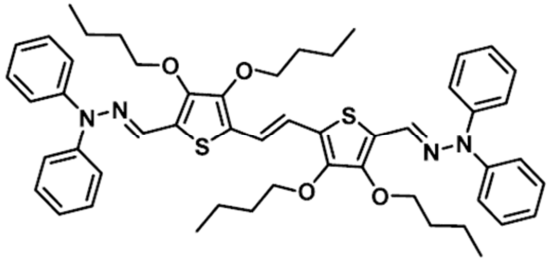

HOMO - 5.08
LUMO -2.57

Figure 6.17: Chemical structure of **3**

The UV-Vis absorption spectrum of **3** in dichloromethane solution is shown in Fig. 6.18. The absorption spectrum is shown for both neutral form as well as oxidized form. From the figure it is evident that the material absorbs mainly in the wavelength range of 410 to 600 nm.

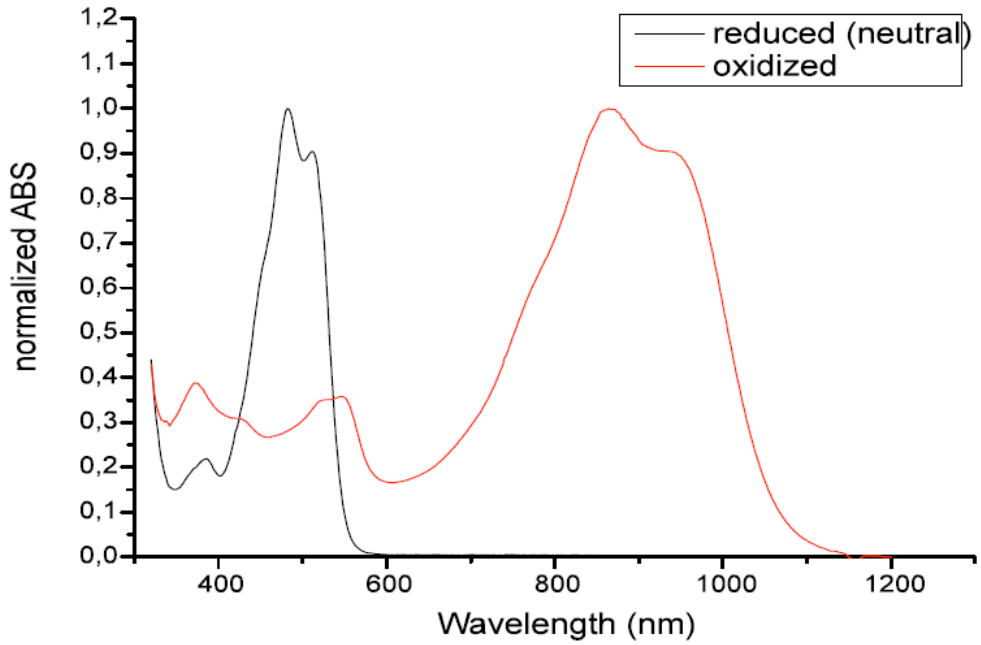

Figure 6.18: UV-Vis absorption spectra of compound 3 (in CH_2Cl_2) in neutral form (black) and in oxidized form (red)

The same optimized conditions used in the case of **2** were used, and only the composition ratios, the solvent and the active layer thickness were changed. Also for **3** it was observed that the 1:3 composition is the best in terms of efficiency. Two different solvents (chlorobenzene and dichlorobenzene) were tried for spin coating of the active layer. As for compound **2**, chlorobenzene and dichlorobenze gave similar results, but chlorobenzene was used because it gave more homogeneous samples. The effect of different active layer thickness was also investigated. Cells with a 70 nm thick active layer were the best performing, compared to the 50 nm optimal thickness for **2**.

A typical I-V curve is shown in Fig. 6.19

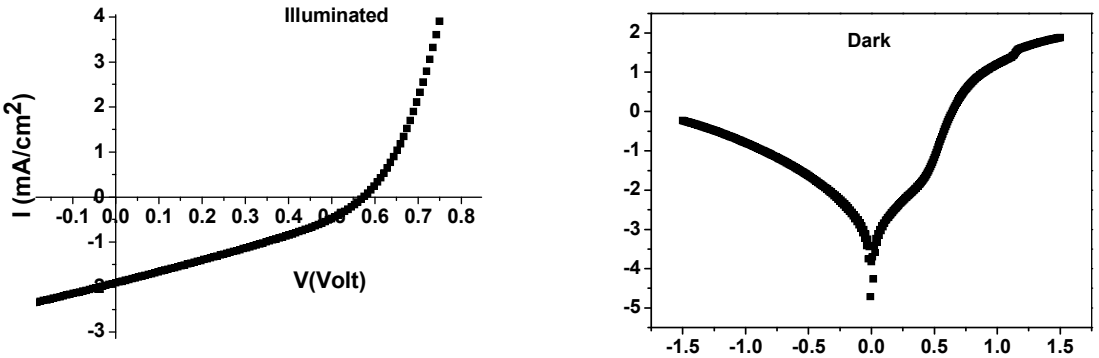

Figure 6.19: I/V curve of BHJ obtained using **3** and $PC_{71}BM$, with a 1:3 sample composition

Table 6.9 summarizes the I/V features obtained with the best performing set of conditions.

Device Parameters	Ca/Al Electrode
Open Circuit Voltage (Voc)	0.58
Short circuit current (Isc)	1.89
Fill Factor	0.32
Efficiency	**0.35**

Table 6.9: I/V parameters of BHJ obtained using **3** with $PC_{71}BM$, in a 1:3 sample composition.

Atomic force images acquired in the tapping mode of BHJ of **3**:$PC_{71}BM$ are shown in Fig. 6.20 in both topography and phase contrast. It is evident that compound **3** shows poor connectivity in phase separated domains when compared to **2**. This could be a possible explanation for the lower efficiency values obtained for this compound, along with the lower absorption values.

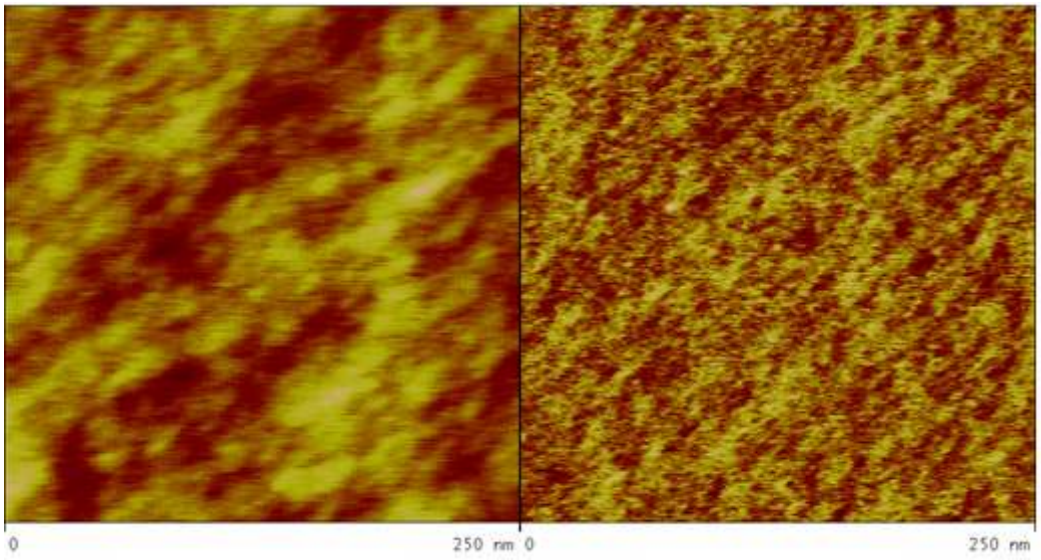

(a)

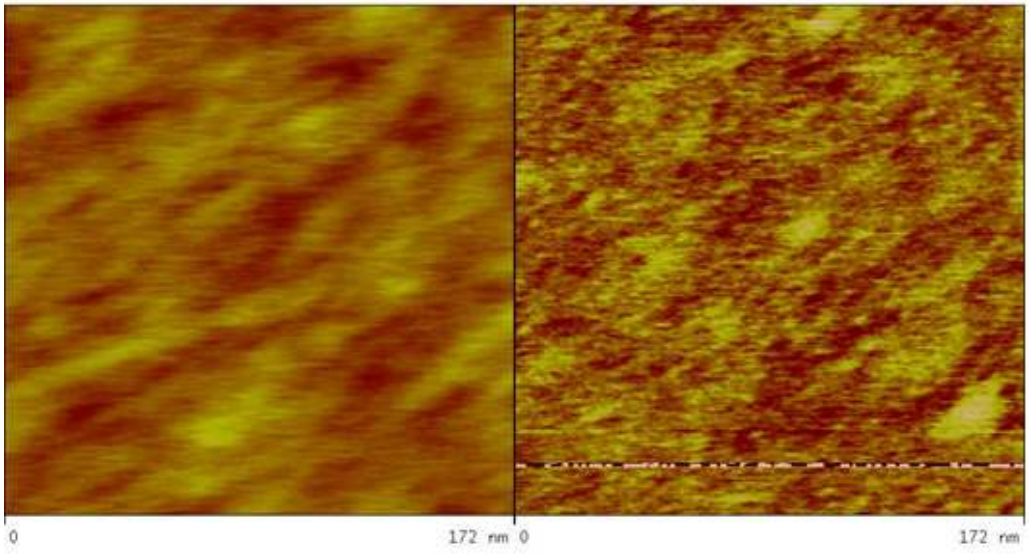

(b)

Figure 6.20: AFM images with (left) topographic and (right) phase contrast of compound **3**:$PC_{71}BM$ BHJ.

The photovoltaic performance of the two new hydrazonic compounds can now be summarized

1. Samples prepared for device optimization using different solvent, spin-coating temperatures, solvent atmospheres, show the same trend of device parameters for both compound **2** and **3**, which leads to the conclusion that a "slower" phase separation is better .

2. It was observed that a 1:3, **2: $PC_{71}BM$** composition gives a better performance than 1:2 or 1:4. This was also observed in **3: $PC_{71}BM$** composition (in this case only 1:3 and 1:4 composition was tried)

3. Using Ca/Al as a cathode improves the device efficiency by mainly increasing the open circuit voltage and also slightly fill factor.

4. These new hydrazonic donors are a potential candidate for organic photovoltaics.

However, one can further improve the performance of these compounds by increasing the absorption along with further fine tuning of the HOMO and LUMO level of the compounds by chemical modifications.

BIBLIOGRAPHY

1. M. Ghedini, A. Golemme, I. Aiello, N. Godbert, R. Termine, A. Crispini, M. La Deda, F. Lelj, M. Amati, S. Belviso, *J. Mater. Chem*., 21, 13434, 2011.
2. I. Aiello, D. Dattilo M. Ghedini, A. Golemme, *J. Am. Chem. Soc*., 123, 5598, 2001.
3. R. Termine, I. Aiello, D. Dattilo, M. Ghedini, A. Golemme, *Adv. Mater*., 15, 723, 2003.
4. M. Ghedini, I. Aiello, A. Crispini, A. Golemme, M. La Deda, D. Pucci, *Coord. Chem. Rev*., 250, 1373, 2006.
5. S. Cook, H. Ohkita, Y. Kim, J.J. Benson-Smith, D.D.C. Bradley, J.R. Durrant, *Chem. Phy. Lett*., 445, 276, 2007.
6. C. Wanzhu, W. Ming, Z. Jie, W. Ergang, Y. Tingbing, H. Chao, S.M. Ji, W. Hongbin, G. Xiong, C.J. Yong, *Phys. Chem. C*, 115, 2314, 2011.
7. S. Kim, B. Kim, J. Kim, *Appl. Mater. Inter*., 6, 1264, 2010.
8. H.Y. Chen, J. Hou, S. Zhang, Y. Liang, G. Yang, Y. Yang, L. Yu, Y. Wu, G. Li, *Nat. Photonics*, 3, 649, 2009.
9. E. Verploegen, R. Mondal, C. Bettinger, S. Sok, M. Toney, Z. Bao, *Adv. Funct. Mater*., 20, 3519, 2010.
10. G. Dennler, K. Forberich, M.C. Scharber, C.J. Barbec, *J. Appl. Phys*., 102, 054516, 2007.
11. D. Bagnis, L. Beverina, H. Huang, F. Silvestri, Y.Yao, H. Yan, G. A. Pagani, T. J. Marks, and A. Facchetti*, J. Am. Chem. Soc., 132*, 4074, 2010.
12. J. C. Hummelen, J. Konl, L. Sanchez, Proc. Of the SPIE, Vol. 4108, 76, 2001.
13. A.C. Arias, M. Granstrom, D.S. Thomos, K. Petritsch, R.H. Friend, *Synth. Met*., 102, 953, 1999.
14. A.C. Arias, M. Granstrom, D.S. Thomos, K. Petritsch, R.H. Friend, Phys. Rev. B., 60, 1854, 1999.
15. P. Peumans, A. Yakimov, S. R. Forest, *J. Appl., Phys*., 93, 3693, 2003.
16. K. Fostiropoulos, M. Vogel, B. Mertesacker, A. Weidinger, Proc. Of the SPIE, Vol. 4801, 1, 2003.
17. J. Huang, P.F. Miller, J. D. de Mello, A. J. de Mello, D.D.C. Bradley, *Synth. Met*., 139, 569, 2003.
18. K. Kawano, R. Pacios, D. Poplavskyy, J. Nelson, D. D. C. Bradley, and J. R. Durrant: Sol. Energy Mater. Sol. Cells, 90, 3520, 2006.
19. T. Yamanari, T Taima, J. Sakai1, J. Tsukamoto, and Y. Yoshida, J. J. of Appd. Phy., 49, 01AC02. 2010.
20. L. Schmidt-Mende, A. Fechtenkotter, K. Müllen, E. Moons, R.H. Friend, J.D. MacKenzie, *Science,* 293**,** 1119, 2001.
21. C.J. Brabec, A. Cravino, D. Meissner, N.S. Sariciftci, T. Fromherz, M.T. Rispens, L. Sanchez, J.C. Hummelen, *Adv. Funct. Mater*., 11, 374, 2001.
22. A. Kumar, S. Sista, Y. Yang, *J. Appl. Phys*., 105, 094512, 2009.
23. V.D. Mihailetchi, P.W.M. Blom, J.C. Hummelen, M.T. Rispens, *J. Appl. Phys*., 94, 6849, 2003.
24. A.K. Pandey, P.E. Shaw, I.D.W. Samuel, J.M. Nunzi, *Appl. Phys. Lett.*, 94, 103303, 2009.
25. K.L. Mutolo, E.I. Mayo, B.P. Rand, S.R. Forrest, M.E. Thompson, *J. Am. Chem. Soc*., 128, 8108, 2006.
26. Y. Yuan, T. J. Reece, P. Sharma, S. Poddar, S. Ducharme, A. Gruverman, Y. Yang, J. Huang, *Nat. Mater.*, 10, 296, 2011.